Article

Base-Resistant Ionic Metal-Organic Framework as a Porous Ion-Exchange Sorbent

Base-Resistant
Cationic MOF for
Ion-Exchange Over
Wide pH range

pH=
4 to 14

Aamod V. Desai,
Arkendu Roy,
Partha Samanta,
Biplab Manna,
Sujit K. Ghosh

sghosh@iiserpune.ac.in

HIGHLIGHTS

Design and synthesis of a rare chemically stable cationic MOF is presented

The MOF exhibits uncommon resistance under highly alkaline conditions

The features endow ion exchange of bulky organic pollutants over a wide pH range
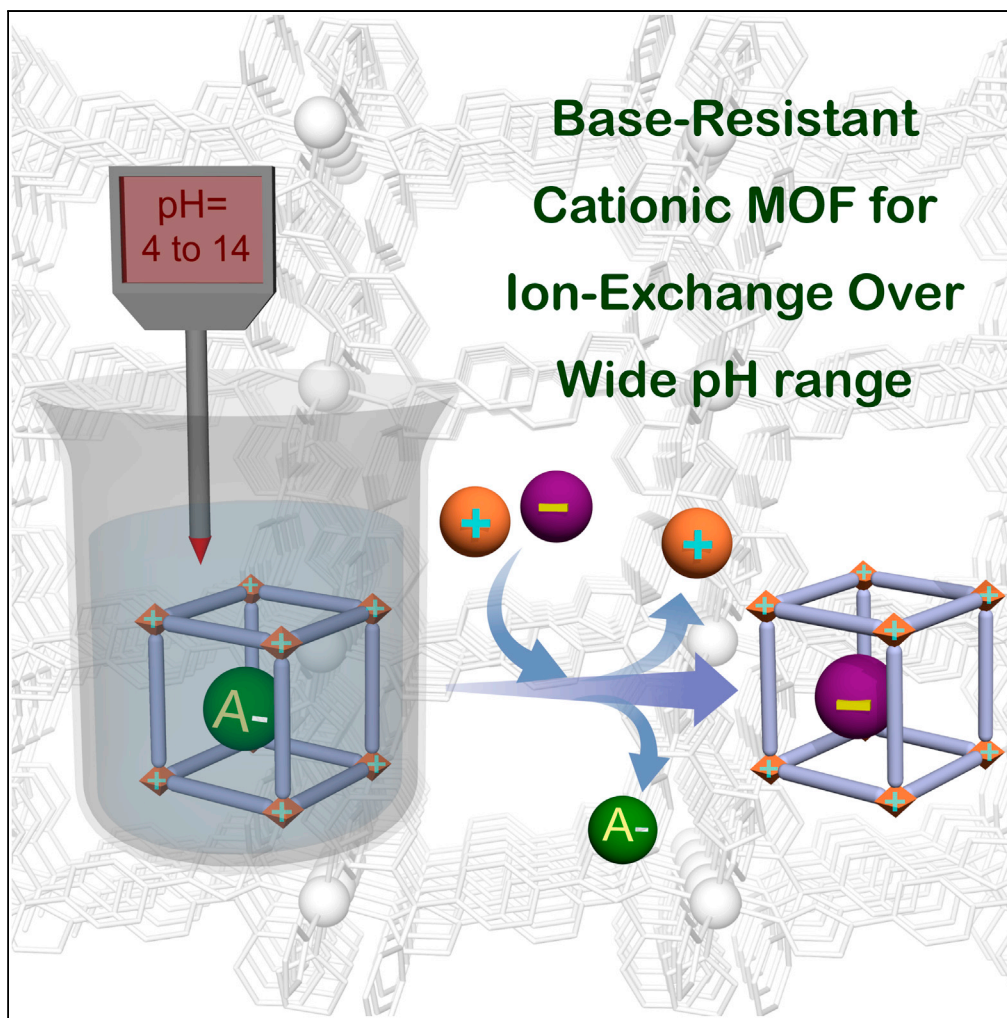
Article

Base-Resistant Ionic Metal-Organic Framework as a Porous Ion-Exchange Sorbent

Aamod V. Desai,[1] Arkendu Roy,[1] Partha Samanta,[1] Biplab Manna,[1] and Sujit K. Ghosh[1,2,3,*]

SUMMARY

A systematic approach has been employed to obtain a hydrolytically stable cationic metal-organic framework (MOF). The synthesized two-dimensional Ni(II)-centered cationic MOF, having its backbone built from purely neutral N-donor ligand, is found to exhibit uncommon resistance over wide pH range, particularly even under highly alkaline conditions. This report presents a rare case of a porous MOF retaining structural integrity under basic conditions, and an even rarer case of a porous cationic MOF. The features of stability and porosity in this ionic MOF have been harnessed for the function of charge- and size-selective capture of small organic dye through ion-exchange process across a wide pH range.

INTRODUCTION

Metal-organic frameworks (MOFs) or porous coordination polymers (PCPs) have rapidly evolved as an important subset of porous materials (Long and Yaghi, 2009; Horike et al., 2009; Furukawa et al., 2013; Zhou and Kitagawa, 2014; Howarth et al., 2017; Maurin et al., 2017). The interest in this domain has expanded in recent years owing to the wide range of applicability exhibited by these materials (Farrusseng et al., 2009; Horcajada et al., 2012; Cui et al., 2012; Sen et al., 2012; Li and Xu, 2013; Ramaswamy et al., 2014; Falcaro et al., 2014; Howarth et al., 2015; Sun et al., 2016; Li et al., 2016a; Aguilera-Sigalat and Bradshaw, 2016; Bao et al., 2016; Lustig et al., 2017). MOFs can be broadly segregated into two classes, based on the charge of the coordination network, viz., neutral and ionic MOFs (i-MOFs); i-MOFs are further classified into cationic and anionic (Karmakar et al., 2016; Li et al., 2016b). MOFs afford significant advancement over congener polymeric materials owing to their crystalline nature, which furnishes precise structure-property correlation. Despite several advantages, there remain a few core issues such as hydrolytic and chemical stability that have stalled the progress of MOFs for real-time applications (Canivet et al., 2014; Burtch et al., 2014; Qadir et al., 2015; Hendon et al., 2017). Although a few benchmark MOF compounds having hydrolytic or chemical stability are known, the majority of them are found to be stable predominantly in acidic pH (Ferey et al., 2005; Park et al., 2006; Cavka et al., 2008; Howarth et al., 2016; Wang et al., 2016a, 2016b, 2016c; Liu et al., 2015; Duan et al., 2017; Bai et al., 2016). The infrequent MOFs exhibiting base resistance are typically neutral frameworks built from azolate-based ligands (Howarth et al., 2016). Development of i-MOFs is seeking greater relevance owing to them being potentially viable alternatives to conventional ion exchangers for various applications (Karmakar et al., 2016; Oliver, 2009; Banerjee et al., 2016; Kumar et al., 2017; Li et al., 2017a; Zhu et al., 2017a, 2017c; Liu et al., 2017). The challenges of stability assume greater relevance for cationic MOFs, which generally are vulnerable to disintegration in aqueous medium or mild acid/basic conditions. To overcome the limitations of weak hydrolytic or chemical stability, design strategies that can provide robust compounds offering resistance are highly sought after. Surveying the literature, some reviews have chalked out broad principles guiding the design of water and chemically stable, porous MOFs. These include strengthening the metal-ligand bond and shielding this bond from the influence of foreign species (Qadir et al., 2015; Duan et al., 2017). The proper choice of the metal ions or the suitable kind of the organic ligand have also been found to play a crucial role in bestowing stability to a compound. This formal outline has generally been derived from stable benchmark compounds, which in most cases are neutral MOFs. The systematic design and development of stable cationic MOFs from the insights gained in literature reports is extremely uncommon (Karmakar et al., 2016).

With this background we sought to focus on the development of approaches for designing stable cationic MOFs. Typically, cationic MOFs are fabricated from neutral N-donor ligands, which render cationic frameworks and afford the presence of uncoordinated, substitutable anions (Fei et al., 2010; Schoedel et al., 2011; Ma et al., 2012; Manna et al., 2013, 2016; Chen et al., 2013; Hou et al., 2013; Sheng et al., 2017;

[1]Department of Chemistry, Indian Institute of Science Education and Research (IISER), Dr. Homi Bhabha Road, Pashan, Pune 411 008, India

[2]Centre for Energy Science, IISER Pune, Pune 411 008, India

[3]Lead Contact

*Correspondence: sghosh@iiserpune.ac.in

Zhu et al., 2017b). For affording stability, ligands with higher pKa have found preference (Colombo et al., 2011; Zhang et al., 2012; Pettinari et al., 2016; He et al., 2016; Rieth et al., 2016), and hence ligands with imidazole/triazole-donating units can be more effective as neutral donor ligands (Chen, 2016). Furthermore, the smaller size of five-membered donating moieties can render greater density of the ligands around the metal nodes by feasibility of hexa-coordination, which can shield the metal nodes from the influence of external species. In general, higher dentate ligands are better suited for generating higher dimensional frameworks. In the present discourse, the additional benefit of such linkers is in affording superior kinetic stability (Wang et al., 2016b). Likewise, the appropriate selection of metal center is vital while fabricating stable systems. The choice of the metal node is directed by its ability to bind to the donor groups of the ligands and the resistance to dissociation of the resulting bonds. Among transition metals that bind equally well with N- and O-donor ligands, Ni(II)-based MOFs have been found to offer remarkable hydrolytic stability and, in certain cases, resistance to varying chemical environments (Howarth et al., 2016; Wang et al., 2016b; Colombo et al., 2011; Desai et al., 2016; Lv et al., 2017). In case of cationic MOFs, although the uncoordinated anions are not a direct part of the framework backbone, their choice can be significant in the preparation. From the existing literature, it is observed that organic sulfonates, which are bulky molecules, are known to bind to metal centers typically at higher temperatures only (Fei and Oliver, 2011; Fei et al., 2013; Sergo et al., 2015; Yang and Fei, 2017). In the current context, such compounds can adapt the function of template anions for the creation of voids and can be an integral part of the framework.

Combining the above-mentioned facets, herein we report the synthesis of a two-dimensional (2D) Ni(II)-centered cationic MOF, viz., $[\{Ni(L)_2\} \cdot (BPSA) \cdot xG]_n$ (L is the ligand; BPSA is 4,4′-biphenyldisulfonic acid; and G is the guest; it is hereafter referred to as IPM-MOF-201, where IPM stands for IISER Pune Materials). The compound is built from a tridentate ligand having terminal imidazole rings and free organosulfonate anions. The compound was found to exhibit extraordinary base resistance, which is uncommonly observed in porous MOFs and even more infrequently observed among i-MOFs. The stability over wide pH range has been tapped for trapping small organic dye molecules across different pH conditions.

RESULTS

Synthesis and Characterization of IPM-MOF-201

Hexagonal-shaped single crystals of compound IPM-MOF-201 were obtained in a solvothermal reaction at 130°C from a mixture of $NiSO_4 \cdot xH_2O$, BPSA, and ligand (L) (1:1.5:1), in a solvent system of N,N′-dimethylformamide (DMF) and water (2:1) (Scheme S1; see Transparent Methods). Compound IPM-MOF-201 was found to crystallize in R-3 space group, as revealed by single-crystal X-ray diffraction (SC-XRD) studies (Table S2). The asymmetric unit is composed of one Ni(II) cation with 1/6 occupancy, one ligand (L) with 1/3 occupancy, and disordered solvent and organic anions (Figure S1). The presence of the organic anion (BPSA) was validated by the ^{1}H-nuclear magnetic resonance (NMR) image obtained after digesting the MOF in D_3PO_4/D_2O, followed by neutralization by NaOD (Figure S11; Scheme S2). The metal center is octahedral with coordination from six nitrogen atoms of six independent ligand units (Figure 1A). We determined the topology of the cationic framework to understand the structure further (Blatov, 2004). The analysis revealed that the compound has a (3,6)-connected binodal kgd topology (Figure S8). Notably, this topology is not commonly found in the domain of MOFs (Zheng et al., 2008; Yao et al., 2011; Mitina and Blatov, 2013; Wang et al., 2014a; Liu et al., 2014; Guillerm et al., 2014). The rational choice of building units for obtaining compounds with such topology would be tris-monodentate trigonal ligands. In the context of the present work, the selection of the ligands would be limited to neutral N-donor linkers. The CSD (Cambridge Structural Database) screening approach suggests that MOFs having tridentate five-membered ligands having neutral donating sites with Ni(II) nodes, and crystallization in such packing modes have not been profoundly explored yet, which can lead to realization of chemically stable frameworks. The important feature of this topology is in the creation of intrinsic porosity (Zheng et al., 2008) (Figures 1B and S2–S5), as the resulting 2D sheets are non-planar. In the context of the present study, the non-planarity of the ligands is well suited as it keeps the metal nodes sterically crowded and enclosed within the 2D layers (Figure S6 and S7). The networks crystallizing in kgd topology disfavor interpenetration, which furnishes large voids in the overall packing (Zheng et al., 2008). Based on the PLATON calculations, the solvent-accessible void in IPM-MOF-201 is estimated to be 2754 $Å^3$ (49%), considering only the cationic network.

Basic characterization of the compound was carefully performed before all subsequent studies. The purity of the bulk phase was validated using powder X-ray diffraction (PXRD) patterns (Figure S9). The peaks corresponding to the ligand were found to be retained in the Fourier transform infrared (FTIR) spectrum
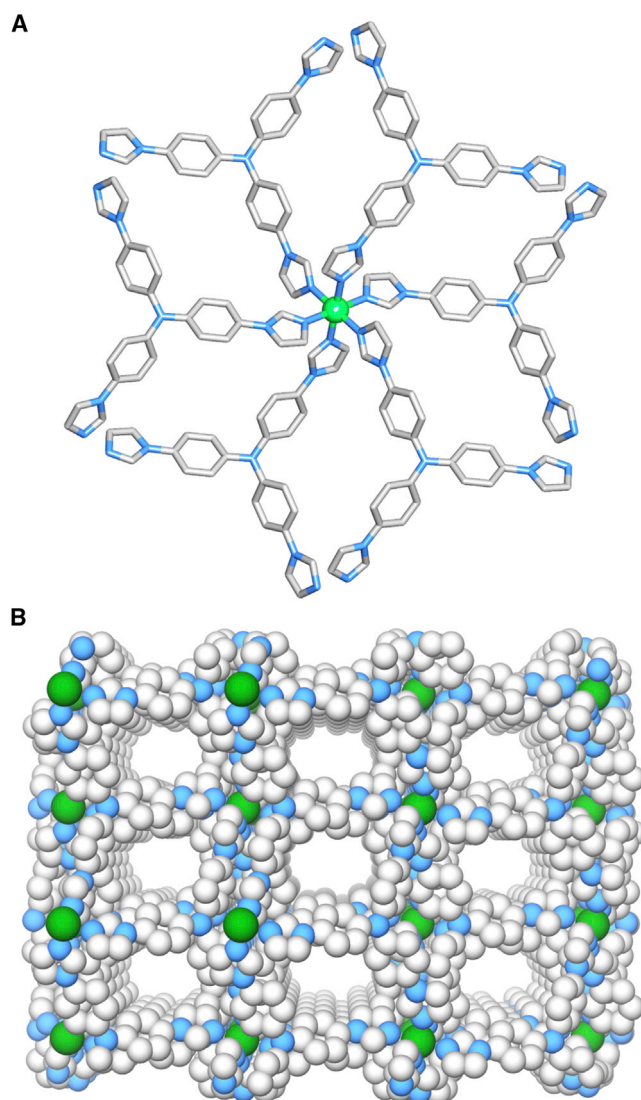
A

B

Figure 1. Structural Features and Characterization of IPM-MOF-201

(A) Coordination environment in IPM-MOF-201.

(B) Perspective view of packing in IPM-MOF-201 showing porous channels. (Hydrogen atoms and disordered anions have been omitted for clarity. Color code: Ni, green; C, gray; N, blue).

See also Figure S1–S19 and Table S2.

for IPM-MOF-201, along with the peak corresponding to S-O stretching frequency (Figure S10) (Li et al., 2014; Samanta et al., 2017a). Field Emission Scanning Electron Microscope (FESEM) images of IPM-MOF-201 confirmed the hexagonal morphology of the crystallites, and Energy-Dispersive X-ray (EDX) spectra (EDX) spectra supported the purity of the crystallites (Figures S12 and S13). Thermogravimetric analysis (TGA) profile suggested initial loss of guest molecules, water, and DMF (Figure S14).

To substantiate the formation of the compound as the favorable product, synthesis was carried out using different Ni^{2+} salts keeping the molar ratios same. In all the cases, we observed purity of the product from PXRD patterns, FTIR spectra, EDX profiles, and morphological analysis using SEM images (Figures S15–S17). The formation of the compound in different batches validated the favorable formation of IPM-MOF-201. Low-temperature gas adsorption measurements were performed to substantiate the porosity of the compound. We observed almost no uptake for N_2 (77 K) (Figure S18), whereas there was considerable uptake for CO_2 (195 K) with strong hysteresis (Figure S18), which suggested strong
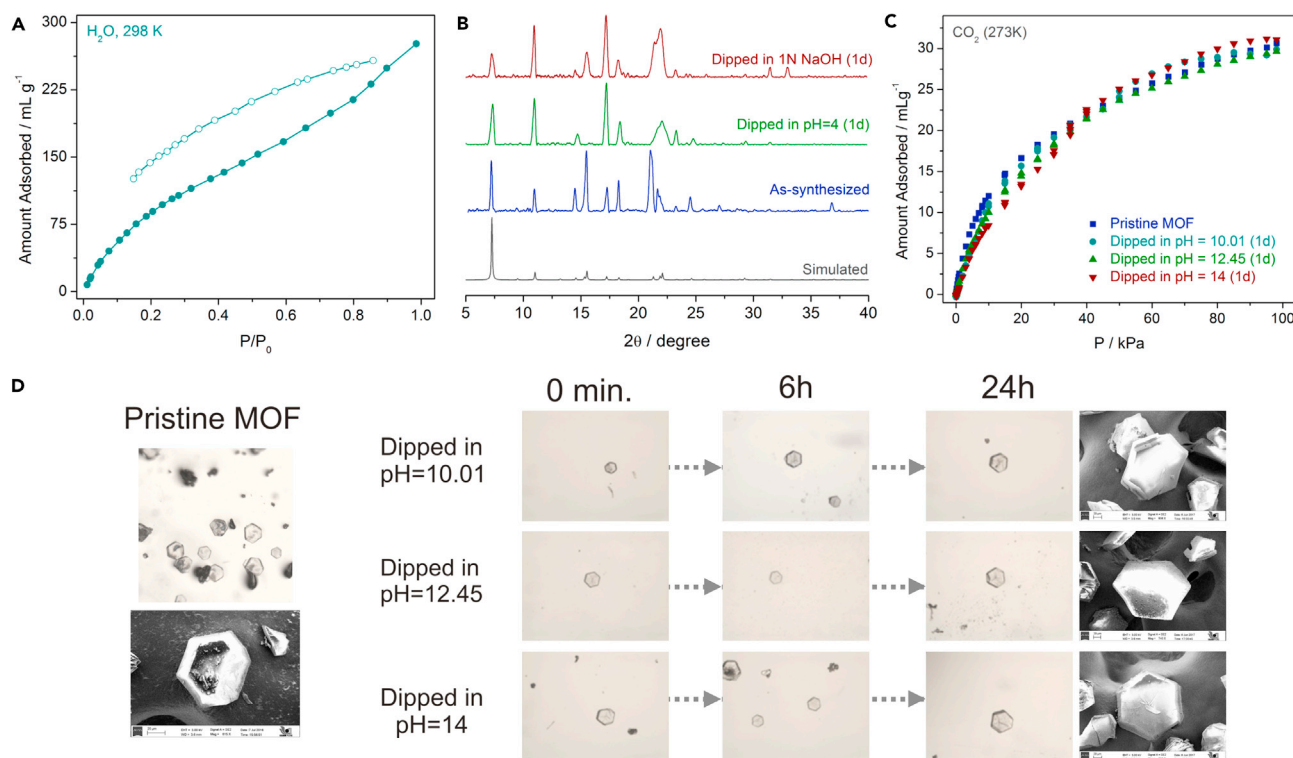
Figure 2. Stability Studies in IPM-MOF-201

(A) Water adsorption isotherm for IPM-MOF-201 at 298 K (closed and open symbols denote adsorption and desorption, respectively).

(B) PXRD patterns of pH = 4 (green) and pH = 14 (red) dipped phases, relative to the as-synthesized phase (blue) and simulated pattern (gray).

(C) CO_2 adsorption profiles (273 K) of base-treated phases of IPM-MOF-201.

(D) Photographs of different phases recorded by optical microscope and the corresponding FESEM images after 24 hr.

See also Figure S20–S38 and Tables S1 and S3.

interactions with the uncoordinated anions. CO_2 adsorption isotherms were also recorded at 273 K and 298 K, which exhibited uptake of $\sim$31 mLg^{-1} and $\sim$20 mLg^{-1}, respectively (Figure S19). The water adsorption isotherm (298 K) revealed that the voids present in the compound permitted the entry of water molecules (Figures 2A and S20).

Stability Studies

To check the hydrolytic stability of the compound over a period, single crystals of IPM-MOF-201 were dipped in water for 30 days, and we found that the morphology of the crystals remained unaffected (Figure S21). The hydrolytic stability was further substantiated by the retention of bulk-phase purity (Figure S22) and CO_2 adsorption (Figure S31). Enthused from these basic characterizations and the robust nature of the compound in aqueous medium, we then set out to investigate the stability of the compound across varying pH. Initially single crystals of IPM-MOF-201 were dipped in pH solutions of 4, 10, and 12.45, and the retention of the crystallinity was monitored under an optical microscope at different time intervals (Figures 2D and S23).

In all the three cases we found that the crystals remained intact with no significant loss to crystallinity. To extrapolate this observation even further, single crystals were dipped in 1N NaOH (pH = 14) solution and observed at different time intervals, and even in this case the crystals appeared to remain unaffected (Figures 2D and S23). Unit-cell parameters were recorded for the crystals recovered after 1-day treatment at pH = 4 and 1N NaOH. In both the cases the parameters were found to be in close proximity to that of the as-synthesized phase (Table S3), suggesting negligible effect of the pH environment. Upon lowering the pH further, we found dissociation of the framework, which is typically observed for frameworks built from neutral N-donor linkers.

Encouraged by these preliminary observations we then tested this behavior on the bulk scale. Crystals of IPM-MOF-201 were dispersed in separate pH solutions under stirring for 24 hr. The compounds recovered after these treatments were characterized using PXRD, SEM, and gas adsorption measurements. PXRD patterns confirmed the retention of bulk-phase purity (Figures 2B and S24), along with supplementary evidence from FTIR spectra, SEM images, and EDX profiles (Figures 2D and S25–S29). Also, inductively coupledplasma atomic emission spectroscopy (ICP-AES) analysis for the supernatant collected after dipping in pH = 4 and 1N NaOH validated that the compound did not undergo disintegration (Table S1). CO_2 adsorption measurements at 273 K (Figures 2C and S30) and 298 K (Figure S31) substantiated the resistance of the compound, with almost similar uptakes in all the treated phases, without perturbing the structural integrity (Figure S34). As additional evidence to the above-mentioned observations, we performed NMR studies using deuterated solvents. Crystals of IPM-MOF-201 were dispersed in a solution of $NaOD/D_2O$ for 1 day (Scheme S3). The solution was centrifuged to separate the filtrate, and $CDCl_3$ was added to the residue and rinsed thoroughly. The solution was centrifuged once again and the supernatant collected for recording the NMR spectra (Figure S32). The lack of peaks corresponding to the ligand in the spectra corroborated with the observed base resistance of IPM-MOF-201. In addition, the SEM images of the residue were recorded, and they showed retention of the hexagonal morphology (Figure S33). The residue was subjected to CO_2 adsorption (298 K), and we found similar uptakes, substantiating the resistance feature (Figure S31). It is noteworthy that the present compound marks an extremely rare example of an MOF exhibiting base resistance and an even rarer case of a cationic MOF retaining integrity under basic conditions. We believe that the structure of the compound affords significant hydrolytic stability owing to the shielding of the metal nodes in the non-planar 2D sheets (Figure S7), as all the coordination sites are occupied by the ligands. It is well understood in the literature that the binding of N-donor linkers to metal nodes can make the pore surface inert and hydrophobic (Zhang et al., 2012). In addition, the utilization of the tridentate ligand with strongly coordinating terminal units affords enhanced stability to the packing (Wang et al., 2016b). Also, Ni(II)-based MOFs are known to be hydrolytically stable, and in certain cases, even stable under extreme chemical conditions (Howarth et al., 2016; Wang et al., 2016b; Colombo et al., 2011; Desai et al., 2016; Lv et al., 2017), providing superior stability to the resulting framework.

As a control experiment to examine the efficacy of the design strategy, we synthesized an isostructural Co(II) MOF keeping all the other reagents and their ratios same. The bulk-phase purity of the thus synthesized MOF, viz., IPM-MOF-201(Co), was validated using PXRD patterns (Figure S35). Although Co-based MOF has been previously reported with ligand (L) (Yao et al., 2011), owing to the bulky anion, the structure obtained is subtly different (Figure S35). Upon primary characterization, the compound was activated in an analogous manner to the Ni(II) compound and then checked for its stability in different pH. Crystals of IPM-MOF-201(Co) were dipped in different pH solutions and monitored under optical microscope at incremental time intervals (Figure S36). Unlike the previous case, the crystals were found to disintegrate with increasing time intervals. This observation was substantiated in the PXRD patterns recorded for the bulk phase after dipping in different conditions (Figure S35). Further control experiments with two previously reported MOFs having similar structures (Yao et al., 2011; Liu et al., 2014) were checked, and in both the cases we observed complete breakdown of the framework under high basic conditions (Figures S37 and S38). These results further support the validity of design strategy in the choice of metal nodes and employment of higher dentate neutral ligands.

Capture of Anionic Organic Dyes

Along with the critical issue of stability, suitability of MOFs for real-time application in varying chemical environments is a focused aspect of research in this domain. Although only as a consequence of stability, the effective utilization of porosity across wide pH range remains a challenge for this class of materials. Thus to tap the resistance of IPM-MOF-201 across wide pH range and the accessible porosity to foreign species, we sought to investigate the ability of the compound to capture small organic dye molecules. Capture and degradation of dye molecules is an important research problem owing to the serious hazards caused by the release of these compounds in water streams (Wang et al., 2014b). Most of these contaminants have high absorption, which blocks the passage of sunlight to living species in water media (Allen and Koumanova, 2005). Also, on account of high consumption of dissolved oxygen, the aquatic ecosystem is imbalanced. These issues have compounded in recent years owing to the extent and growth of dye-manufacturing industries. It is reckoned that the annual production scale of commercial dyes is close to a million tons (Robinson et al., 2001; Rawat et al., 2016). The allied industries, which include textiles, are

estimated to release 10% of the total dyestuffs as industrial wastewaters. Thus given the gravity of this issue, researches have trialed several techniques such as adsorption, coagulation, membrane separation, and photocatalysis (Crini, 2006; Ayati et al., 2014; Sarkka et al., 2015; Singh et al., 2015; Samanta et al., 2017b). Owing to the simplicity, ease of handling, sensitivity, and relative lower cost of operation, adsorption-based methods have commanded greater attention. Thus the development of newer sorbents that can overcome the bottlenecks of existing/conventional adsorbents such as poor selectivity, slow kinetics, and stability are desired. Notably, majority of the studies using i-MOFs as sorbent of dyes have been performed in organic solvents or water at neutral pH (Nickerl et al., 2013; Zhao et al., 2013, 2017; Chen et al., 2015; Song et al., 2015; Gao et al., 2016; Yu et al., 2016; Jia et al., 2016; Li et al., 2017b, 2017c; Nath et al., 2017). Dyes released as industrial wastewaters can have varying pH, and hence the stability and investigation of MOF-based adsorption at varying pH is more pertinent for seeking real-time applicability.

The cationic nature of IPM-MOF-201 and the shape of the pores actuated us to test its trapping ability for anionic dye with linear shape methyl orange (MO). When crystals of IPM-MOF-201 were dipped in an aqueous MO solution (1 mM), the supernatant underwent decoloration over 48 hr, whereas the color of the crystals changed to orange during the same period (Figure S39). PXRD patterns and the SEM images of this ion-exchanged phase suggested retention of structural integrity (Figures S40 and S42). Ultraviolet-visible (UV-vis) spectra were recorded at increasing time intervals to corroborate with the naked-eye observation. As anticipated, the UV-vis spectra of the supernatant showed gradual decrease in intensity with passage of time (Figures S41 and S56). This behavior was retained across different pH of 4.01, 10.01, and 12.45 as well (Figure S44). The PXRD patterns corresponding to these phases demonstrated that the ion exchange at different pH did not affect the structure (Figure S60). To substantiate that the ion-exchange process was charge selective, a cationic dye of similar size, viz., methylene blue (MB), was chosen. The color of the compound did not change upon addition to an aqueous solution of MB and the color of the supernatant did not undergo any change in intensity (Figure S43), as evidenced using UV-vis experiments.

This hypothesis of charge selectivity was further supported when the compound was added to an equimolar mixture of MO and MB. The color of the compound turned orange, and the UV-vis spectra of the supernatant confirmed the selective uptake of only MO (Figures S45–S47). A prototype column experiment was executed wherein this charge-selective separation of dyes could be monitored in a short time (Figure S64). In addition, MB did not entrap even at pH = 10.01, confirming the effect of charge selectivity of the compound (Figure S48). The mixtures of cationic and anionic dyes could be separated over wide pH ranges as well (Figure S65). In addition to charge selectivity, we observed that the ion exchange was size selective. A bulky dye, viz., bromothymol blue, was chosen for this study, and no noticeable change was observed in the time-dependent UV-vis spectra (Figure S53). For real-time applicability, recycling of the adsorbent is highly desired. The cycling efficiency of IPM-MOF-201 for MO dye was checked over three cycles, and the performance was found to be retained (Figure S63).

To extend this behavior even further, we checked the efficacy of IPM-MOF-201 to entrap anionic dyes of similar sizes, viz., indigo carmine (IC) and alizarin red S (ARS). It has been observed in the literature that the dye molecules with dimensions between the minimum and maximum pore windows in porous frameworks can undergo ion exchange (Nickerl et al., 2013; Zhao et al., 2013, 2017; Chen et al., 2015; Song et al., 2015; Gao et al., 2016; Yu et al., 2016; Jia et al., 2016; Li et al., 2017b, 2017c; Nath et al., 2017). Thus linear ions having suitable dimensions can be expected to undergo uptake. In both the cases the color of the compound changed drastically upon addition of the MOF to aqueous solution of the dyes (Figure S49). PXRD patterns for these phases suggested retention of the structural integrity without change to the overall framework (Figure S50). Like the previous case, we recorded time-dependent UV-Vis spectra at different pH, and a similar pattern was observed for both IC and ARS (Figures S51 and S54). Crystals of IPM-MOF-201 were added to an equimolar mixture of two blue dyes (IC and MB). As anticipated, only the peak corresponding to IC underwent decrement without any noticeable change to the peak for MB (Figure S55). As a control experiment, time-dependent UV-vis spectra of blank dye solutions were recorded to validate the ion-exchange process (Figure S52). The anionic dye capture tendency was retained even for dye molecules with carboxylic acid (methyl red [MR]) and phenolic functionalities (4-phenylazophenol [PAP]) (Figures S57 and S59). As observed previously, the structural integrity was not perturbed during the
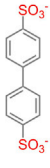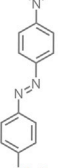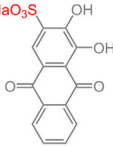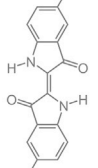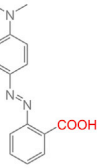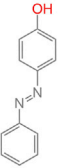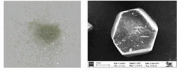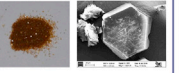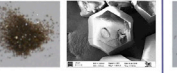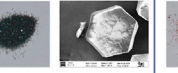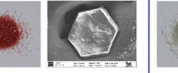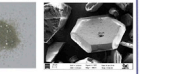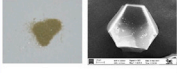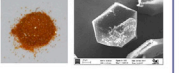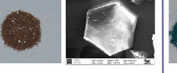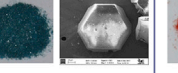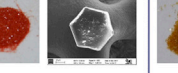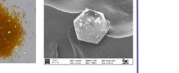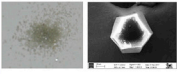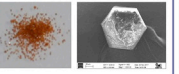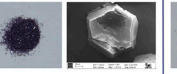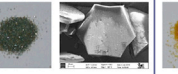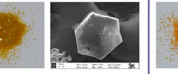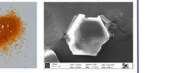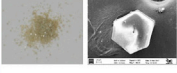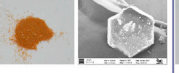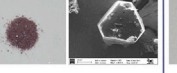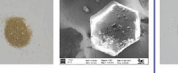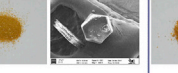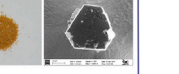
Figure 3. Dye Capture Studies by IPM-MOF-201

Summary showing photographs of all the phases of compound IPM-MOF-201 and the dye-exchange phases under different conditions. The corresponding SEM images of each phase are shown alongside.

See also Figure S39–S65.

exchange at different pH (Figures S58 and S60). For the dyes studied in this work, the ion-exchange process was also observed under high basic conditions at pH = 14 (Figures S61 and S62). Figure 3 summarizes the naked-eye dye capture process at different pH along with the corresponding morphology of the compound. These results suggest that the feature of differential color of the dyes at different pH is carried unabatedly into the MOF-encapsulated phases as well, making this MOF a potentially useful marker for capture of dyes at specific pH.

DISCUSSION

In summary, we have developed a hydrolytically stable cationic MOF that exhibits remarkably high resistance across wide pH range. To the best of our knowledge this is an extremely rare example of a porous MOF exhibiting base resistance and an even rarer case of a porous cationic MOF retaining structural integrity even under high basic pH. Control experiments were executed to validate the choice of the building blocks and the design strategy. The stability and the accessible porosity were harnessed for the function of trapping small organic dyes over wide pH range. Notably, hitherto systematic investigation of dye capture over wide pH range has not been investigated systematically in the literature of MOFs. We believe that the results obtained from this work will contribute significantly to the development of design principles for i-MOFs that offer stability over varying chemical environments.

METHODS

All methods can be found in the accompanying Transparent Methods supplemental file.

DATA AND SOFTWARE AVAILABILITY

The accession number for the IPM-MOF-201 reported in this paper is [CCDC]: [1561299].

REFERENCES

Aguilera-Sigalat, J., and Bradshaw, D. (2016). Synthesis and applications of metal-organic framework–quantum dot (QD@MOF) composites. Coord. Chem. Rev. *307*, 267–291.

Allen, S., and Koumanova, B. (2005). Decolourisation of water/wastewater using adsorption. J. Univ. Chem. Technol. Metall. *40*, 175–192.

Ayati, A., Ahmadpur, A., Bamoharram, F.F., Tanhaei, B., Manttari, M., Lahtinen, M., and Sillanpaa, M. (2014). Novel Au NPs/Preyssler acid/TiO$_2$ nanocomposite for the photocatalytic removal of azo dye. Sep. Purif. Technol. *133*, 415–420.

Bai, Y., Dou, Y., Xie, L.-H., Rutledge, W., Li, J.-R., and Zhou, H.-C. (2016). Zr-based metal–organic frameworks: design, synthesis, structure, and applications. Chem. Soc. Rev. *45*, 2327–2367.

Banerjee, D., Kim, D., Schweiger, M.J., Kruger, A.A., and Thallapally, P.K. (2016). Removal of TcO$_4^-$ ions from solution: materials and future outlook. Chem. Soc. Rev. *45*, 2724–2739.

Bao, Z., Chang, G., Xing, H., Krishna, R., Ren, Q., and Chen, B. (2016). Potential of microporous metal–organic frameworks for separation of hydrocarbon mixtures. Energy Environ. Sci. *9*, 3612–3641.

Blatov, V.A. (2004). TOPOS (Samara State University).

Burtch, N.C., Jasuja, H., and Walton, K.S. (2014). Water stability and adsorption in metal–organic frameworks. Chem. Rev. *114*, 10575–10612.

Canivet, J., Fateeva, A., Guo, Y., Coasne, B., and Farrusseng, D. (2014). Water adsorption in MOFs: fundamentals and applications. Chem. Soc. Rev. *43*, 5594–5617.

Cavka, J.H., Jakobsen, S., Olsbye, U., Guillou, N., Lamberti, C., Bordiga, S., and Lillerud, K.P. (2008). A new zirconium inorganic building brick forming metal organic frameworks with exceptional stability. J. Am. Chem. Soc. *130*, 13850–13851.

Chen, S.-S. (2016). The roles of imidazole ligands in coordination supramolecular systems. CrystEngComm *18*, 6543–6565.

Chen, Y.-Q., Li, G.-R., Chang, Z., Qu, Y.-K., Zhang, Y.-H., and Bu, X.-H. (2013). A Cu(I) metal–organic framework with 4-fold helical channels for sensing anions. Chem. Sci. *4*, 3678–3682.

Chen, D.-M., Shi, W., and Cheng, P. (2015). A cage-based cationic body-centered tetragonal metal–organic framework: single-crystal to single-crystal transformation and selective uptake of organic dyes. Chem. Commun. *51*, 370–372.

Colombo, V., Galli, S., Choi, H.J., Han, G.D., Maspero, A., Palmisano, G., Masciocchi, N., and Long, J.R. (2011). High thermal and chemical stability in pyrazolate-bridged metal–organic frameworks with exposed metal sites. Chem. Sci. *2*, 1311–1319.

Crini, G. (2006). Non-conventional low-cost adsorbents for dye removal: a review. Bioresour. Technol. *97*, 1061–1085.

Cui, Y., Yue, Y., Qian, G., and Chen, B. (2012). Luminescent functional metal–organic frameworks. Chem. Rev. *112*, 1126–1162.

Desai, A.V., Manna, B., Karmakar, A., Sahu, A., and Ghosh, S.K. (2016). A water-stable cationic metal–organic framework as a dual adsorbent of oxoanion pollutants. Angew. Chem. Int. Ed. *55*, 7811–7815.

Duan, J., Jin, W., and Kitagawa, S. (2017). Water-resistant porous coordination polymers for gas separation. Coord. Chem. Rev. *332*, 48–74.

Falcaro, P., Ricco, R., Doherty, C.M., Liang, K., Hill, A.J., and Styles, M.J. (2014). MOF positioning technology and device fabrication. Chem. Soc. Rev. *43*, 5513–5560.

Farrusseng, D., Aguado, S., and Pinel, C. (2009). Metal-organic frameworks: opportunities for catalysis. Angew. Chem. Int. Ed. *48*, 7502–7513.

Fei, H., and Oliver, S.R.J. (2011). Copper hydroxide ethanedisulfonate: a cationic inorganic layered material for high-capacity anion exchange. Angew. Chem. Int. Ed. *50*, 9066–9070.

Fei, H., Rogow, D.L., and Oliver, S.R.J. (2010). Reversible anion exchange and catalytic properties of two cationic Metal−Organic frameworks based on Cu(I) and Ag(I). J. Am. Chem. Soc. *132*, 7202–7209.

Fei, H., Han, C.S., Robins, J.C., and Oliver, S.R.J. (2013). A cationic metal–organic solid solution based on Co(II) and Zn(II) for chromate trapping. Chem. Mater. *25*, 647–652.

Ferey, G., Mellot-Draznieks, C., Serre, C., Millange, F., Dutour, J., Surble, S., and Margiolaki, I. (2005). A chromium terephthalate-based solid with unusually large pore volumes and surface area. Science *309*, 2040–2042.

Furukawa, H., Cordova, K.E., O'Keeffe, M., and Yaghi, O.M. (2013). The chemistry and applications of metal-organic frameworks. Science *341*, 1230444.

Gao, C.-Y., Yang, Y., Ai, J., Tian, H.-R., Li, L.-J., Yang, W., Dang, S., and Sun, Z.-M. (2016). A multifunctional Mn^{II} phosphonate for rapid separation of methyl orange and electron-transfer photochromism. Chem. Eur. J. 22, 11652–11659.

Guillerm, V., Kim, D., Eubank, J.F., Luebke, R., Liu, X., Adil, K., Lah, M.S., and Eddaoudi, M. (2014). A supermolecular building approach for the design and construction of metal–organic frameworks. Chem. Soc. Rev. 43, 6141–6172.

He, T., Zhang, Y.-Z., Wang, B., Lv, X.-L., Xie, L.-H., and Li, J.-R. (2016). A base-resistant Zn^{II}-based metal–organic framework: synthesis, structure, postsynthetic modification, and gas adsorption. ChemPlusChem 81, 864–871.

Hendon, C.H., Reith, A.J., Korzynski, M.D., and Dinca, M. (2017). Grand challenges and future opportunities for metal–organic frameworks. ACS Cent. Sci. 3, 554–563.

Horcajada, P., Gref, R., Baati, T., Allan, P.K., Maurin, G., Couvreur, P., Ferey, G., Morris, R.E., and Serre, C. (2012). Metal–organic frameworks in biomedicine. Chem. Rev. 112, 1232–1268.

Horike, S., Shimomura, S., and Kitagawa, S. (2009). Soft porous crystals. Nat. Chem. 1, 695–704.

Hou, S., Liu, Q.-K., Ma, J.-P., and Dong, Y.-B. (2013). Cd(II)-Coordination framework: synthesis, anion-induced structural transformation, anion-responsive luminescence, and anion separation. Inorg. Chem. 52, 3225–3235.

Howarth, A.J., Liu, Y., Hupp, J.T., and Farha, O.K. (2015). Metal–organic frameworks for applications in remediation of oxyanion/cation-contaminated water. CrystEngComm 17, 7245–7253.

Howarth, A.J., Liu, Y., Li, P., Li, Z., Wang, T.C., Hupp, J.T., and Farha, O.K. (2016). Chemical, thermal and mechanical stabilities of metal–organic frameworks. Nat. Rev. Mater. https://doi.org/10.1038/natrevmats.2015.18.

Howarth, A.J., Peters, A.W., Vermeulen, N.A., Wang, T.C., Hupp, J.T., and Farha, O.K. (2017). Best practices for the synthesis, activation, and characterization of metal–organic frameworks. Chem. Mater. 29, 26–39.

Jia, Y.-Y., Ren, G.-J., Li, A.-L., Zhang, L.-Z., Feng, R., Zhang, Y.-H., and Bu, X.-H. (2016). Temperature-Related synthesis of two anionic metal–organic frameworks with distinct performance in organic dye adsorption. Cryst. Growth Des. 16, 5593–5597.

Karmakar, A., Desai, A.V., and Ghosh, S.K. (2016). Ionic metal-organic frameworks (iMOFs): design principles and applications. Coord. Chem. Rev. 307, 313–341.

Kumar, P., Pournara, A., Kim, K.-H., Bansal, V., Rapti, S., and Manos, M.J. (2017). Metal-organic frameworks: challenges and opportunities for ion-exchange/sorption applications. Prog. Mater. Sci. 86, 25–74.

Li, S.L., and Xu, Q. (2013). Metal–organic frameworks as platforms for clean energy. Energy Environ. Sci. 6, 1656–1683.

Li, B., Zhang, Y., Krishna, R., Yao, K., Han, Y., Wu, Z., Ma, D., Shi, Z., Pham, T., Space, B., et al. (2014). Introduction of π-complexation into porous aromatic framework for highly selective adsorption of ethylene over ethane. J. Am. Chem. Soc. 136, 8654–8660.

Li, B., Chrzanowski, M., Zhang, Y., and Ma, S. (2016a). Applications of metal–organic frameworks featuring multi-functional sites. Coord. Chem. Rev. 307, 106–129.

Li, P., Vermeulen, N.A., Gong, X., Malliakas, C.D., Stoddart, J.F., Hupp, J.T., and Farha, O.K. (2016b). Design and synthesis of a water-stable anionic uranium-based metal–organic framework (MOF) with ultra large pores. Angew. Chem. Int. Ed. 55, 10358–10362.

Li, Y., Yang, Z., Wang, Y., Bai, Z., Zheng, T., Dai, X., Liu, S., Gui, D., Liu, W., Chen, M., et al. (2017a). A mesoporous cationic thorium-organic framework that rapidly traps anionic persistent organic pollutants. Nat. Commun. 8, 1354.

Li, C.-P., Zhou, H., Wang, S., Yuan, H.-H., Zhang, S.-Z., and Du, M. (2017b). A nanoporous Ag(I) coordination polymer for selective adsorption of carcinogenic dye Acid Red 26. Chem. Commun. 53, 4767–4770.

Li, Q., Xue, D.-X., Zhang, Y.-F., Zhang, Z.-H., Gao, Z., and Bai, J. (2017c). A dual-functional indium–organic framework towards organic pollutant decontamination via physically selective adsorption and chemical photodegradation. J. Mater. Chem. A. 5, 14182–14189.

Liu, S.-S., Yuan, S., Li, X.-Y., Miao, S., Yu, Z.-W., Wang, X.-P., and Sun, D. (2014). A 'kagome dual' (kgd) sheet based on triangular rigid ligand: synthesis, structure, photoluminescence and anion exchange properties. Inorg. Chim. Acta 416, 195–199.

Liu, T.-F., Feng, D., Chen, Y.-P., Zou, L., Bosch, M., Yuan, S., Wei, Z., Fordham, S., Wang, K., and Zhou, H.-C. (2015). Topology-guided design and syntheses of highly stable mesoporous porphyrinic zirconium metal–organic frameworks with high surface area. J. Am. Chem. Soc. 137, 413–419.

Liu, W., Wang, Y., Bai, Z., Li, Y., Wang, Y., Chen, L., Xu, L., Diwu, J., Chai, Z., and Wang, S. (2017). Hydrolytically stable luminescent cationic metal organic framework for highly sensitive and selective sensing of chromate anions in natural water systems. ACS Appl. Mater. Interfaces 9, 16448–16457.

Long, J.R., and Yaghi, O.M. (2009). The pervasive chemistry of metal–organic frameworks. Chem. Soc. Rev. 38, 1213–1214.

Lustig, W.P., Mukherjee, S., Rudd, N.D., Desai, A.V., Li, J., and Ghosh, S.K. (2017). Metal-organic frameworks: functional luminescent and photonic materials for sensing applications. Chem. Soc. Rev. 46, 3242–3285.

Lv, X.-L., Wang, K., Wang, B., Su, J., Zou, X., Xie, Y., Li, J.-R., and Zhou, H.-C. (2017). A base-resistant metalloporphyrin metal–organic framework for C–H bond halogenation. J. Am. Chem. Soc. 139, 211–217.

Ma, J.-P., Yu, Y., and Dong, Y.-B. (2012). Fluorene-based Cu(II)-MOF: a visual colorimetric anion sensor and separator based on an anion-exchange approach. Chem. Commun. 48, 2946–2948.

Manna, B., Chaudhari, A.K., Joarder, B., Karmakar, A., and Ghosh, S.K. (2013). Dynamic structural behavior and anion-responsive tunable luminescence of a flexible cationic metal–organic framework. Angew. Chem. Int. Ed. 52, 998–1002.

Manna, B., Desai, A.V., and Ghosh, S.K. (2016). Neutral N-donor ligand based flexible metal–organic frameworks. Dalton Trans. 45, 4060–4072.

Maurin, G., Serre, C., Cooper, A., and Ferey, G. (2017). The new age of MOFs and of their porous-related solids. Chem. Soc. Rev. 46, 3104–3107.

Mitina, T.G., and Blatov, V.A. (2013). Topology of 2-periodic coordination networks: toward expert systems in crystal design. Cryst. Growth Des. 13, 1655–1664.

Nath, K., Maity, K., and Biradha, K. (2017). Two-dimensional coordination polymers with "X"-Shaped cavities as adsorbents of oxoanion pollutants and toxic dyes. Cryst. Growth Des. 17, 4437–4444.

Nickerl, G., Notzon, A., Heitbaum, M., Senkovska, I., Glorius, F., and Kaskel, S. (2013). Selective adsorption properties of cationic metal–organic frameworks based on imidazolic linker. Cryst. Growth Des. 13, 198–203.

Oliver, S.R.J. (2009). Cationic inorganic materials for anionic pollutant trapping and catalysis. Chem. Soc. Rev. 38, 1868–1881.

Park, K.S., Ni, Z., Cote, A.P., Choi, J.Y., Huang, R., Uribe-Romo, F.J., Chae, H.K., O'Keeffe, M., and Yaghi, O.M. (2006). Exceptional chemical and thermal stability of zeolitic imidazolate frameworks. Proc. Natl. Acad. Sci. USA 103, 10186–10191.

Pettinari, C., Tabacaru, A., and Galli, S. (2016). Coordination polymers and metal–organic frameworks based on poly(pyrazole)-containing ligands. Coord. Chem. Rev. 307, 1–31.

Qadir, N., Said, S.A.M., and Bahaidarah, H.M. (2015). Structural stability of metal organic frameworks in aqueous media – controlling factors and methods to improve hydrostability and hydrothermal cyclic stability. Microporous Mesoporous Mater. 201, 61–90.

Ramaswamy, P., Wong, N.E., and Shimizu, G.K.H. (2014). MOFs as proton conductors – challenges and opportunities. Chem. Soc. Rev. 43, 5913–5932.

Rawat, D., Mishra, V., and Sharma, R.S. (2016). Detoxification of azo dyes in the context of environmental processes. Chemosphere 155, 591–605.

Rieth, A.J., Tulchinsky, Y., and Dinca, M. (2016). High and reversible ammonia uptake in mesoporous azolate metal–organic frameworks with open Mn, Co, and Ni sites. J. Am. Chem. Soc. 138, 9401–9404.

Robinson, T., McMullan, G., Marchant, R., and Nigam, P. (2001). Remediation of dyes in textile effluent: a critical review on current treatment technologies with a proposed alternative. Biores. Technol. 77, 247–255.

Samanta, P., Desai, A.V., Anothumakkool, B., Shirolkar, M.M., Karmakar, A., Kurungot, S., and Ghosh, S.K. (2017a). Enhanced proton conduction by post-synthetic covalent modification in a porous covalent framework. J. Mater. Chem. A. 5, 13659–13664.

Samanta, P., Chandra, P., Desai, A.V., and Ghosh, S.K. (2017b). Chemically stable microporous hyper-cross-linked polymer (HCP): an efficient selective cationic dye scavenger from an aqueous medium. Mater. Chem. Front. 1, 1384–1388.

Sarkka, H., Bhatnagar, A., and Sillanpaa, M. (2015). Recent developments of electro-oxidation in water treatment — a review. J. Electroanal. Chem. 754, 46–56.

Schoedel, A., Wojtas, L., Kelley, S.P., Rogers, R.D., Eddaoudi, M., and Zaworotko, M.J. (2011). Network diversity through decoration of trigonal-prismatic nodes: two-step crystal engineering of cationic metal–organic materials. Angew. Chem. Int. Ed. 50, 11421–11424.

Sen, S., Nair, N.N., Yamada, T., Kitagawa, H., and Bharadwaj, P.K. (2012). High proton conductivity by a metal–organic framework incorporating Zn_8O clusters with aligned imidazolium groups decorating the channels. J. Am. Chem. Soc. 134, 19432–19437.

Sergo, K.M., Han, C.S., Bresler, M.R., Citrak, S.C., Abdollahian, Y., Fei, H., and Oliver, S.R.J. (2015). Erbium hydroxide ethanedisulfonate: a cationic layered material with organic anion exchange capability. Inorg. Chem. 54, 3883–3888.

Sheng, D., Zhu, L., Xu, C., Xiao, C., Wang, Y., Wang, Y., Chen, L., Diwu, J., Chen, J., Chai, Z., et al. (2017b). Efficient and selective uptake of TcO_4^- by a cationic metal–organic framework material with open Ag^+ sites. Environ. Sci. Technol. 51, 3471–3479.

Singh, R.L., Singh, P.K., and Singh, R.P. (2015). Enzymatic decolorization and degradation of azo dyes – a review. Int. Biodeter. Biodegr. 104, 21–31.

Song, B.-Q., Wang, X.-L., Zhang, Y.-T., Wu, X.-S., Liu, H.-S., Shao, K.-Z., and Su, Z.-M. (2015). Periodic tiling of triangular and square nanotubes in a cationic metal–organic framework for selective anion exchange. Chem. Commun. 51, 9515–9518.

Sun, L., Campbell, M.G., and Dinca, M. (2016). Electrically conductive porous metal-organic frameworks. Angew. Chem. Int. Ed. 55, 3566–3579.

Wang, R., Wang, Z., Xu, Y., Dai, F., Zhang, L., and Sun, D. (2014a). Porous zirconium metal–organic framework constructed from 2D → 3D interpenetration based on a 3,6-connected kgd net. Inorg. Chem. 53, 7086–7088.

Wang, C.-C., Li, J.-R., Lv, X.-L., Zhang, Y.-Q., and Guo, G. (2014b). Photocatalytic organic pollutants degradation in metal–organic frameworks. Energy Environ. Sci. 7, 2831–2867.

Wang, C., Liu, X., Demir, N.K., Chen, J.P., and Li, K. (2016a). Applications of water stable metal–organic frameworks. Chem. Soc. Rev. 45, 5107–5134.

Wang, K., Lv, X.-L., Feng, D., Li, J., Chen, S., Sun, J., Song, L., Xie, Y., Li, J.-R., and Zhou, H.-C. (2016b). Pyrazolate-based porphyrinic metal–organic framework with extraordinary base-resistance. J. Am. Chem. Soc. 138, 914–919.

Wang, B., Lv, X.-L., Feng, D., Xie, L.-H., Zhang, J., Li, M., Xie, Y., Li, J.-R., and Zhou, H.-C. (2016c). Highly stable Zr(IV)-Based metal–organic frameworks for the detection and removal of antibiotics and organic explosives in water. J. Am. Chem. Soc. 138, 6204–6216.

Yang, H., and Fei, H. (2017). Exfoliation of a two-dimensional cationic inorganic network as a new paradigm for high-capacity Cr^{VI}-anion capture. Chem. Commun. 53, 7064–7067.

Yao, X.-Q., Cao, D.-P., Hu, J.-S., Li, Y.-Z., Guo, Z.-J., and Zheng, H.-G. (2011). Chiral and porous coordination polymers based on an N-centered triangular rigid ligand. Cryst. Growth Des. 11, 231–239.

Yu, P., Li, Q., Hu, Y., Liu, N., Zhang, L., Su, K., Qian, J., Huang, S., and Hong, M. (2016). Cuboctahedron-based indium–organic frameworks for gas sorption and selective cation exchange. Chem. Commun. 52, 7978–7981.

Zhang, J.-P., Zhang, Y.-B., Lin, J.-B., and Chen, X.-M. (2012). Metal azolate frameworks: from crystal engineering to functional materials. Chem. Rev. 112, 1001–1033.

Zhao, X., Bu, X., Wu, T., Zheng, S.-T., Wang, L., and Feng, P. (2013). Selective anion exchange with nanogated isoreticular positive metal-organic frameworks. Nat. Commun. https://doi.org/10.1038/ncomms3344.

Zhao, N., Sun, F., Zhang, N., and Zhu, G. (2017). Novel pyrene-based anionic metal–organic framework for efficient organic dye elimination. Cryst. Growth Des. 17, 2453–2457.

Zheng, S.-R., Yang, Q.-Y., Liu, Y.-R., Zhang, J.-Y., Tong, Y.-X., Zhao, C.-Y., and Su, C.-Y. (2008). Assembly of CdI_2-type coordination networks from triangular ligand and octahedral metal center: topological analysis and potential framework porosity. Chem. Commun. 0, 356–358.

Zhou, H.C., and Kitagawa, S. (2014). Metal–organic frameworks (MOFs). Chem. Soc. Rev. 43, 5415–5418.

Zhu, L., Zhang, L., Li, J., Zhang, D., Chen, L., Sheng, D., Yang, S., Xiao, C., Wang, J., Chai, Z., et al. (2017a). Selenium sequestration in a cationic layered rare earth hydroxide: a combined batch experiments and EXAFS investigation. Environ. Sci. Technol. 51, 8606–8615.

Zhu, L., Xiao, C., Dai, X., Li, J., Gui, D., Sheng, D., Chen, L., Zhou, R., Chai, Z., Albrecht-Schmitt, T.E., and Wang, S. (2017b). Exceptional perrhenate/pertechnetate uptake and subsequent immobilization by a low-dimensional cationic coordination polymer: overcoming the Hofmeister bias selectivity. Environ. Sci. Technol. Lett. 4, 316–322.

Zhu, L., Sheng, D., Xu, C., Dai, X., Silver, M.A., Li, J., Li, P., Wang, Y., Wang, Y., Chen, L., et al. (2017c). Identifying the recognition site for selective trapping of $^{99}TcO_4^-$ in a hydrolytically stable and radiation resistant cationic metal–organic framework. J. Am. Chem. Soc. 139, 14873–14876.

Supplemental Information

Base-Resistant Ionic Metal-Organic

Framework as a Porous Ion-Exchange Sorbent

Aamod V. Desai, Arkendu Roy, Partha Samanta, Biplab Manna, and Sujit K. Ghosh
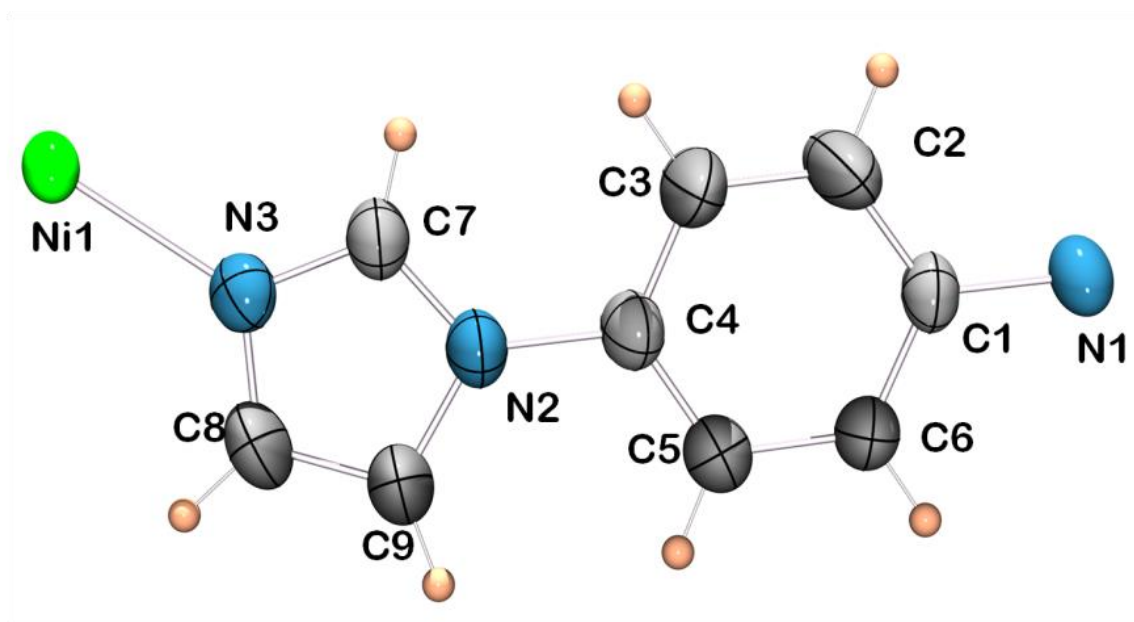
FIGURES

Figure S1: Structural Features of IPM-MOF-201, related to Figure 1.

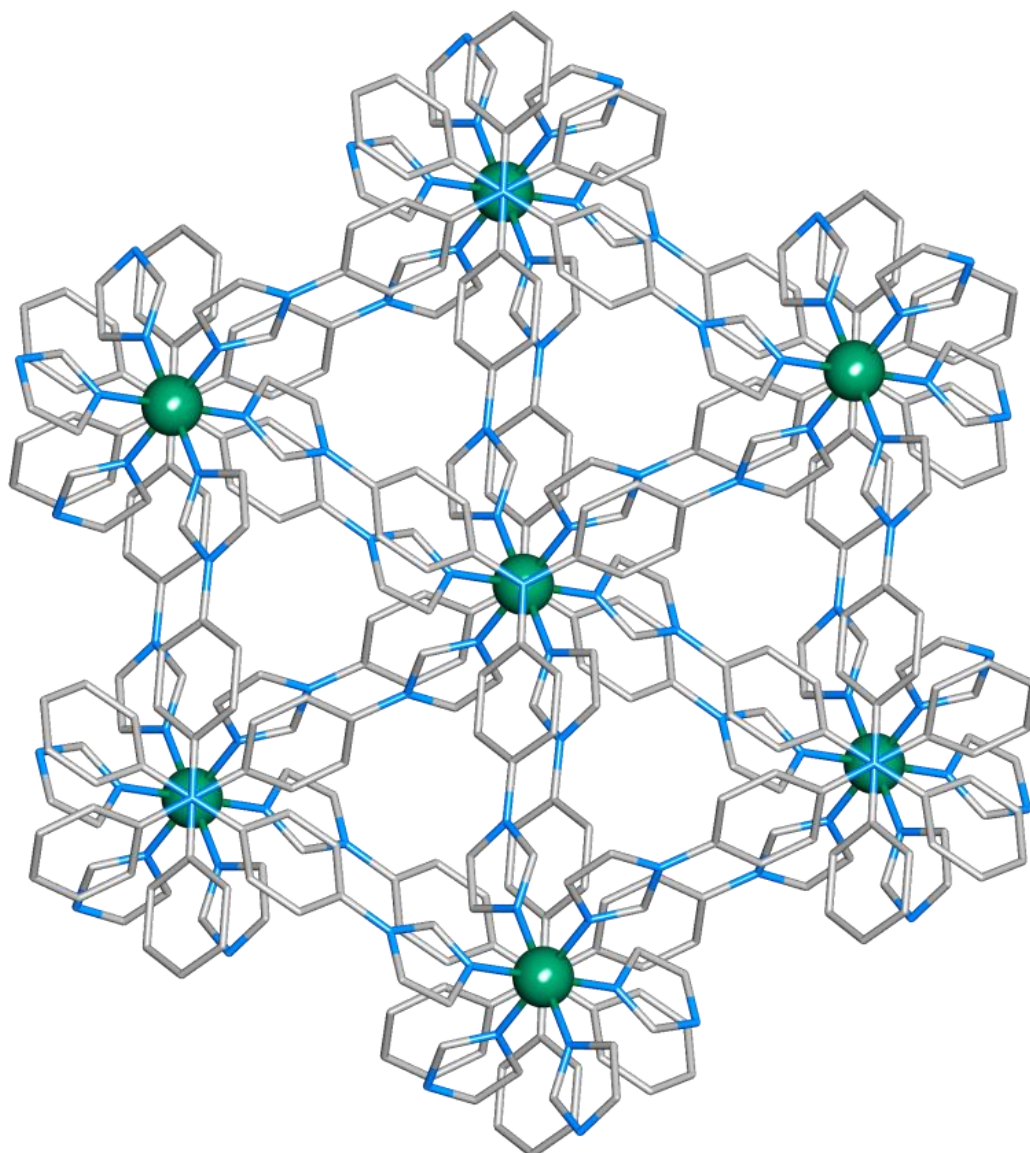ORTEP diagram of asymmetric unit of **IPM-MOF-201** in thermal ellipsoids.

Figure S2: Structural Features of IPM-MOF-201, related to Figure 1.

Figure showing packing of **IPM-MOF-201** along crystallographic *c*-axis. (Hydrogen atoms and disordered anions have been omitted for clarity, colour: Gray - C, Blue - N, Green - Ni).
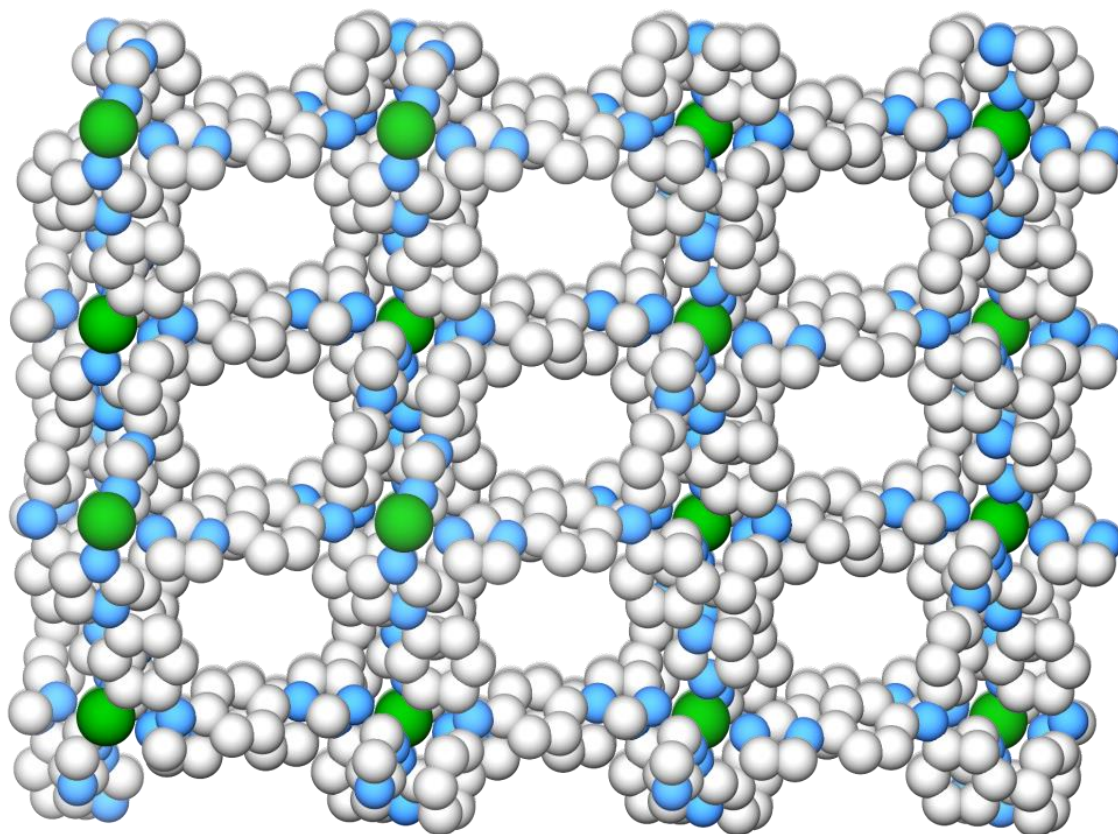
Figure S3: Structural Features of IPM-MOF-201, related to Figure 1.

Packing diagram of **IPM-MOF-201** showing porous channel. (Hydrogen atoms and disordered anions have been omitted for clarity, colour: Gray - C, Blue - N, Green - Ni).
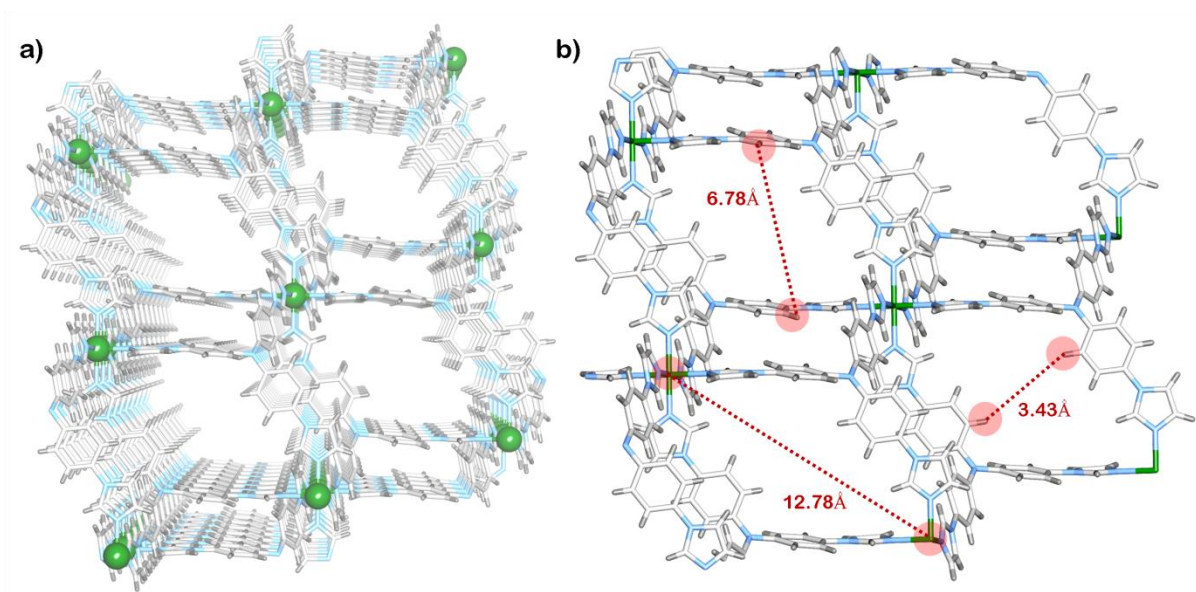
Figure S4: Structural Features of IPM-MOF-201, related to Figure 1.

a) Packing diagram of **IPM-MOF-201** showing porous channels, b) View of a single net adopted from the packing diagram showing the dimensions of the pore. The dimensions have included the Van der Waal radii of the atoms chosen for measurement. The measurements suggest that the d_{min} and d_{max} for the compound is 3.43Å and 12.78Å respectively. (Disordered anions have been omitted for clarity, colour: Light Gray - C, Dark Gray - H, Blue - N, Green - Ni).
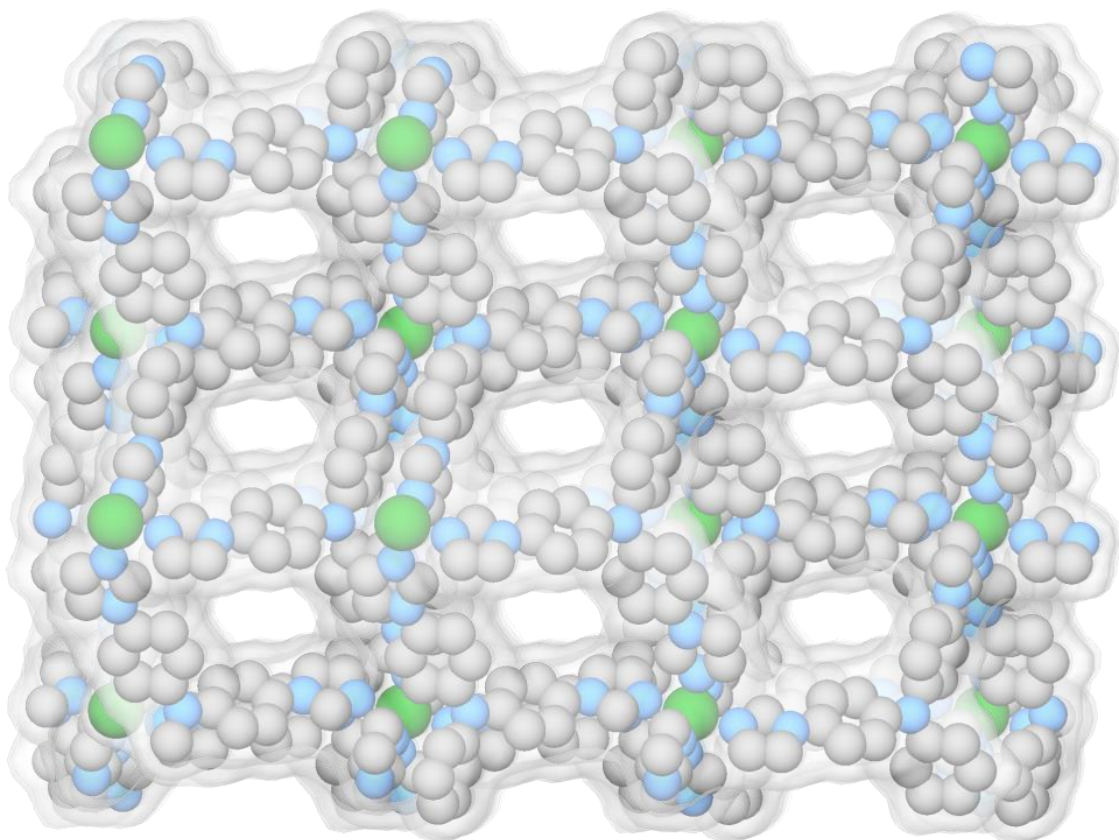
Figure S5: Structural Features of IPM-MOF-201, related to Figure 1.

Packing diagram of **IPM-MOF-201**. (Hydrogen atoms and disordered anions have been omitted for clarity, colour: Gray - C, Blue - N, Green - Ni).
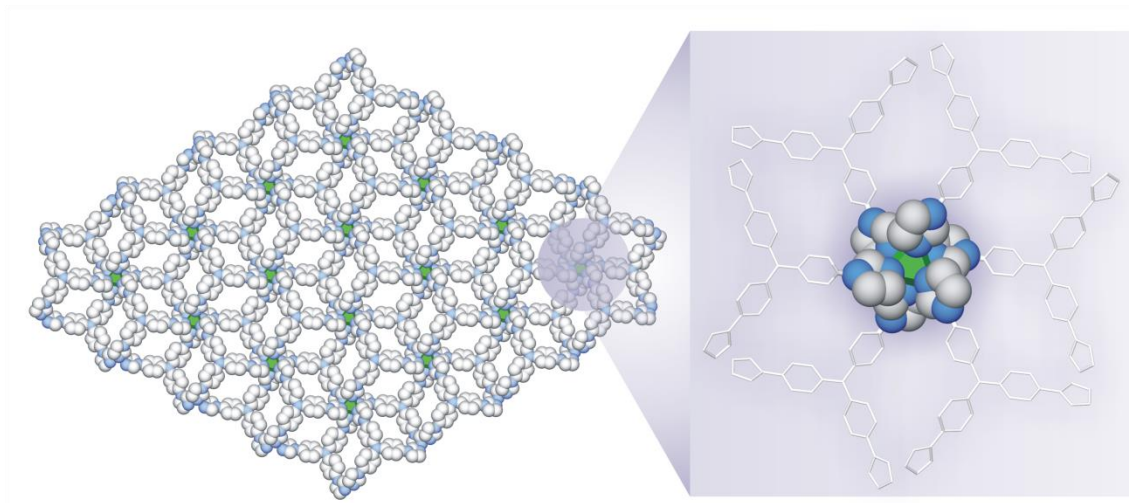
Figure S6: Structural Features of IPM-MOF-201, related to Figure 1.

Packing diagram of **IPM-MOF-201** and zoomed view of the coordination environment of the metal node. (Hydrogen atoms and disordered anions have been omitted for clarity, colour: Gray - C, Blue - N, Green - Ni).
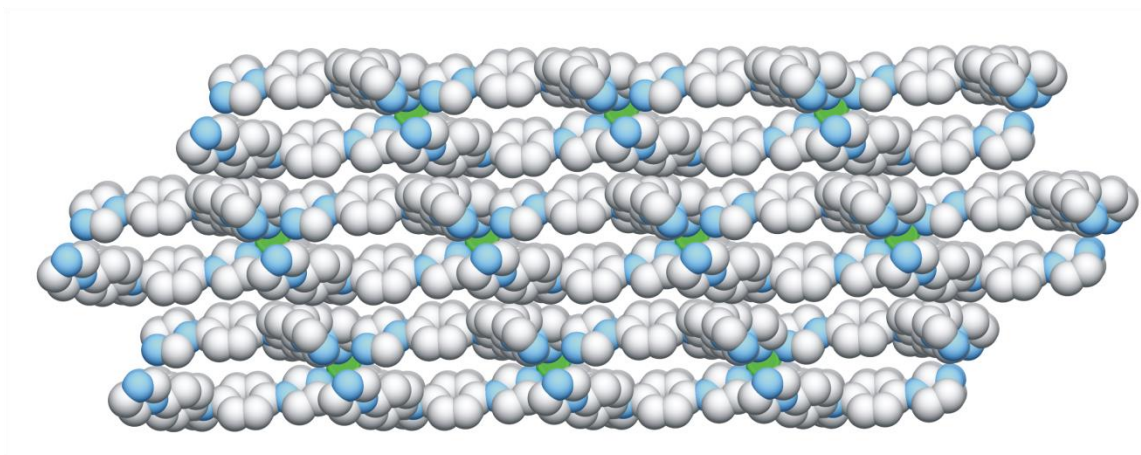
Figure S7: Structural Features of IPM-MOF-201, related to Figure 1.

Packing diagram of **IPM-MOF-201** showing depicting the metal nodes are buried in the 2D layer stacking arrangement. (Hydrogen atoms and disordered anions have been omitted for clarity, colour: Gray - C, Blue - N, Green - Ni).
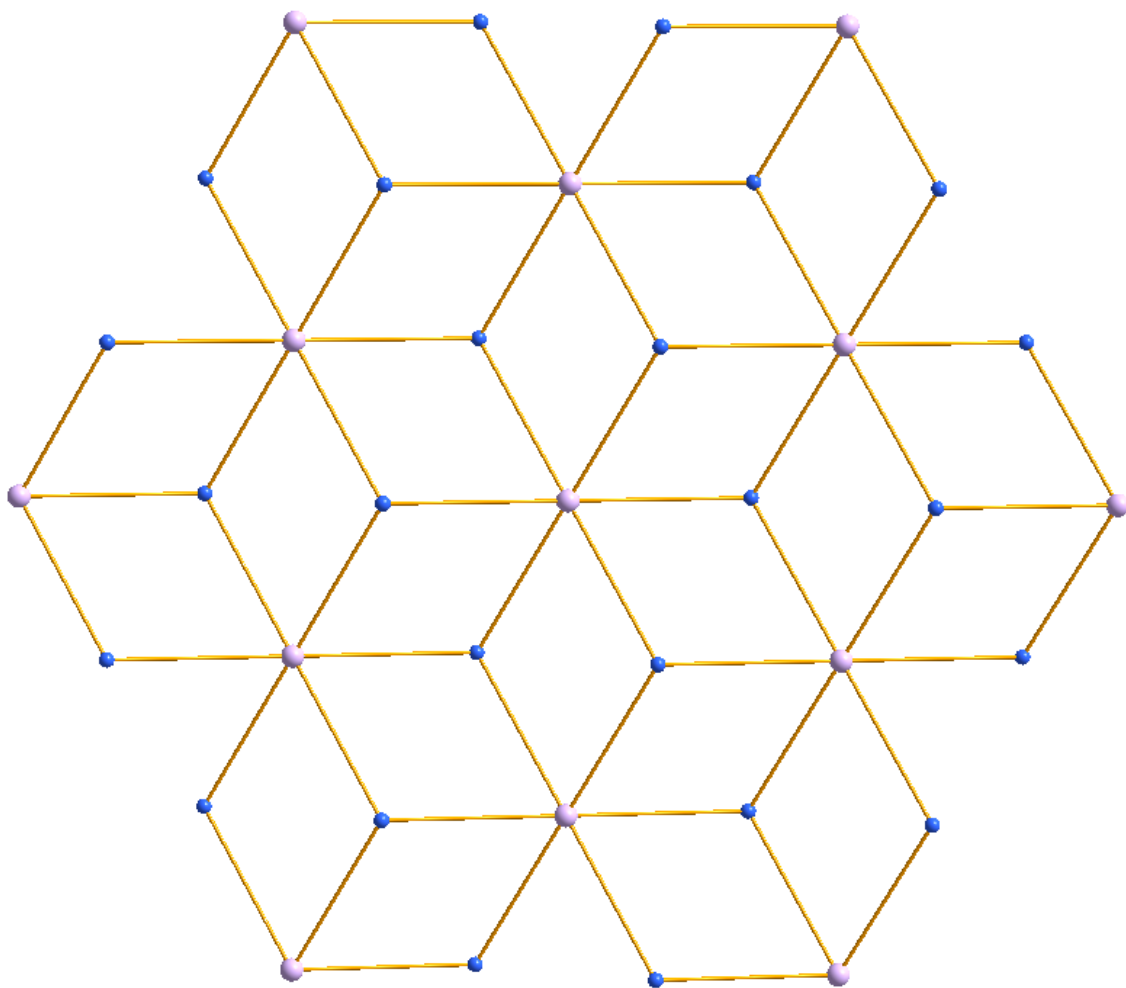
Figure S8: Structural Features of IPM-MOF-201, related to Figure 1.

Simplified topological representation of **IPM-MOF-201** having kgd topology.
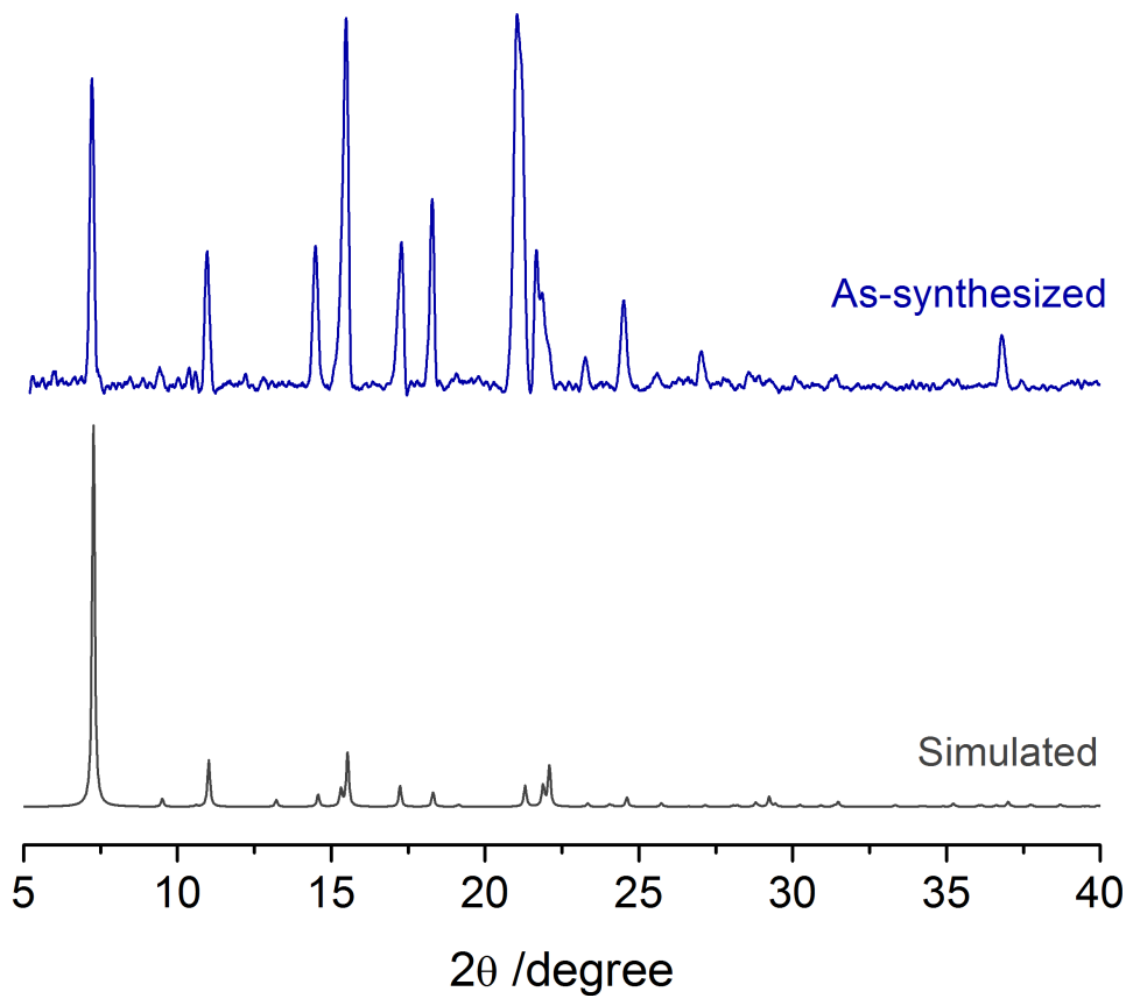
Figure S9: Characterization of IPM-MOF-201, related to Figure 1.

Powder X-ray diffraction patterns of **IPM-MOF-201** - Simulated (gray), as-synthesized (blue).
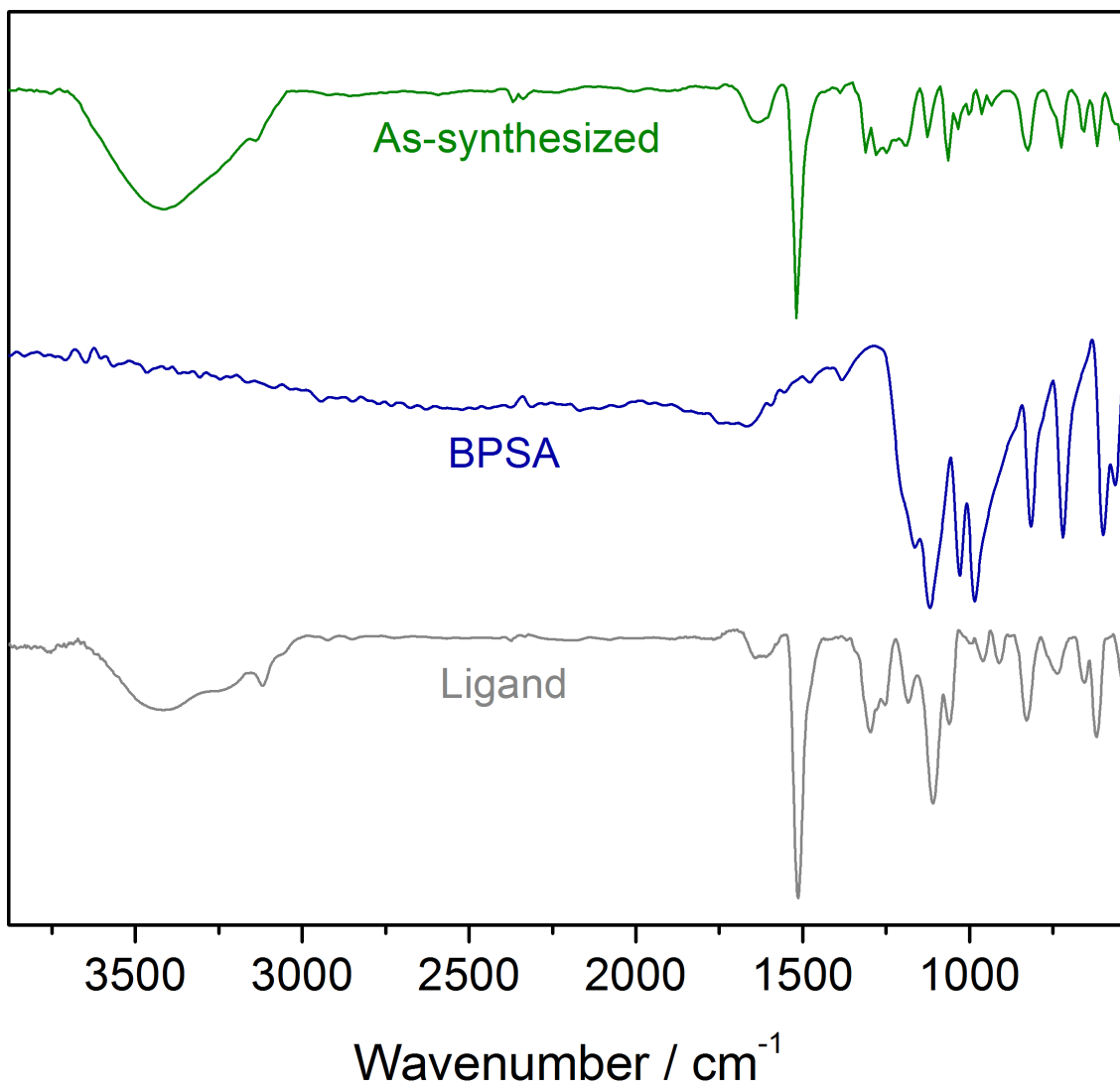
Figure S10: Characterization of IPM-MOF-201, related to Figure 1.
FT-IR spectra for compound **IPM-MOF-201** (green), BPSA (blue) and ligand (gray).
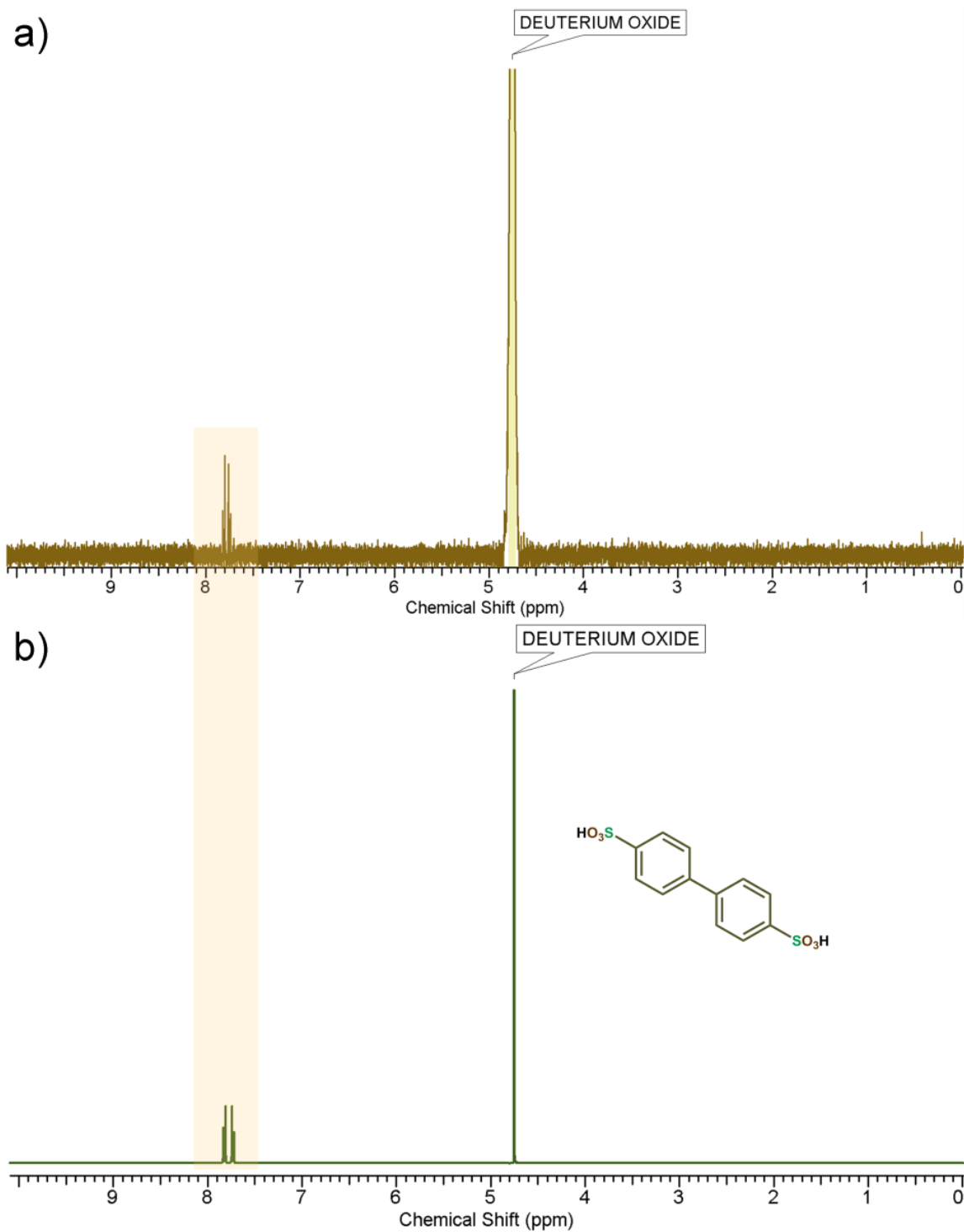
Figure S11: Characterization of IPM-MOF-201, related to Figure 1.
a) ^{1}H-NMR after digesting **IPM-MOF-201** in D_3PO_4/D_2O followed by neutralization with NaOD. b) ^{1}H-NMR of commercially available BPSA in D_2O.
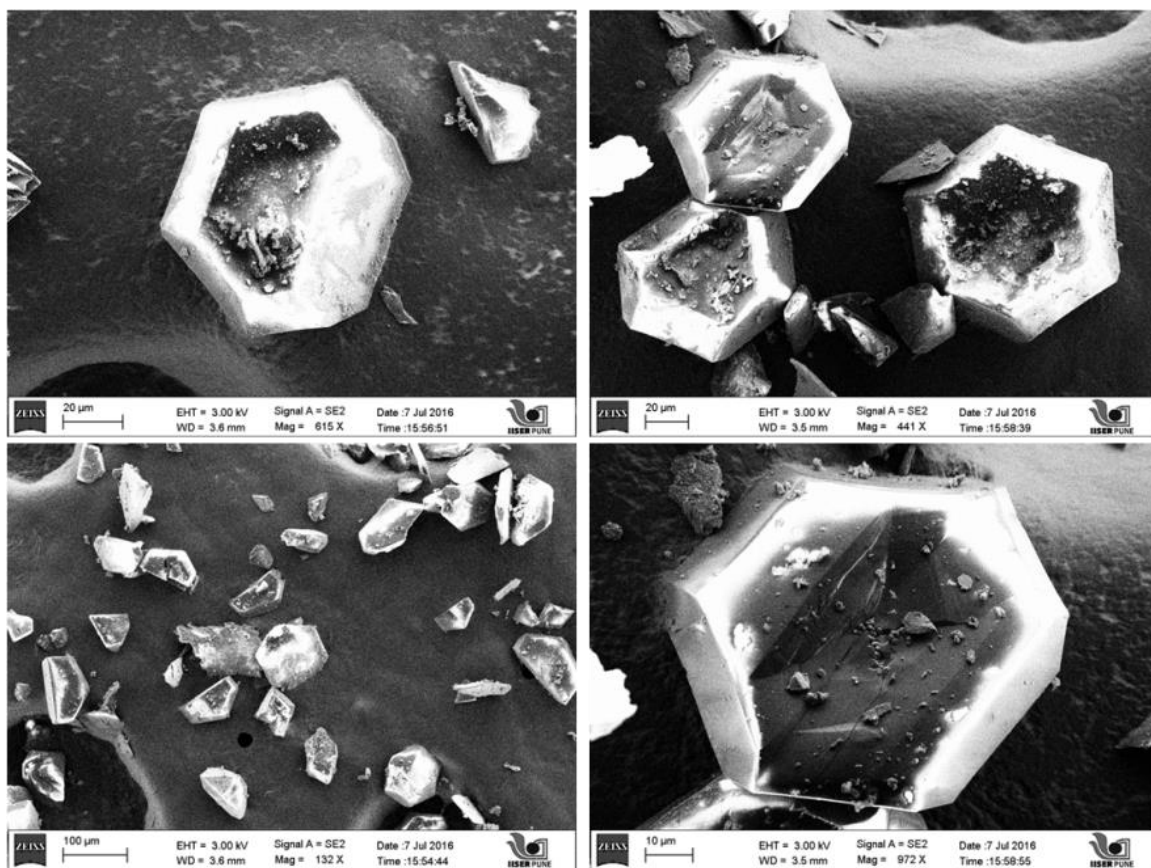
Figure S12: Characterization of IPM-MOF-201, related to Figure 1.
FESEM images for compound **IPM-MOF-201**.
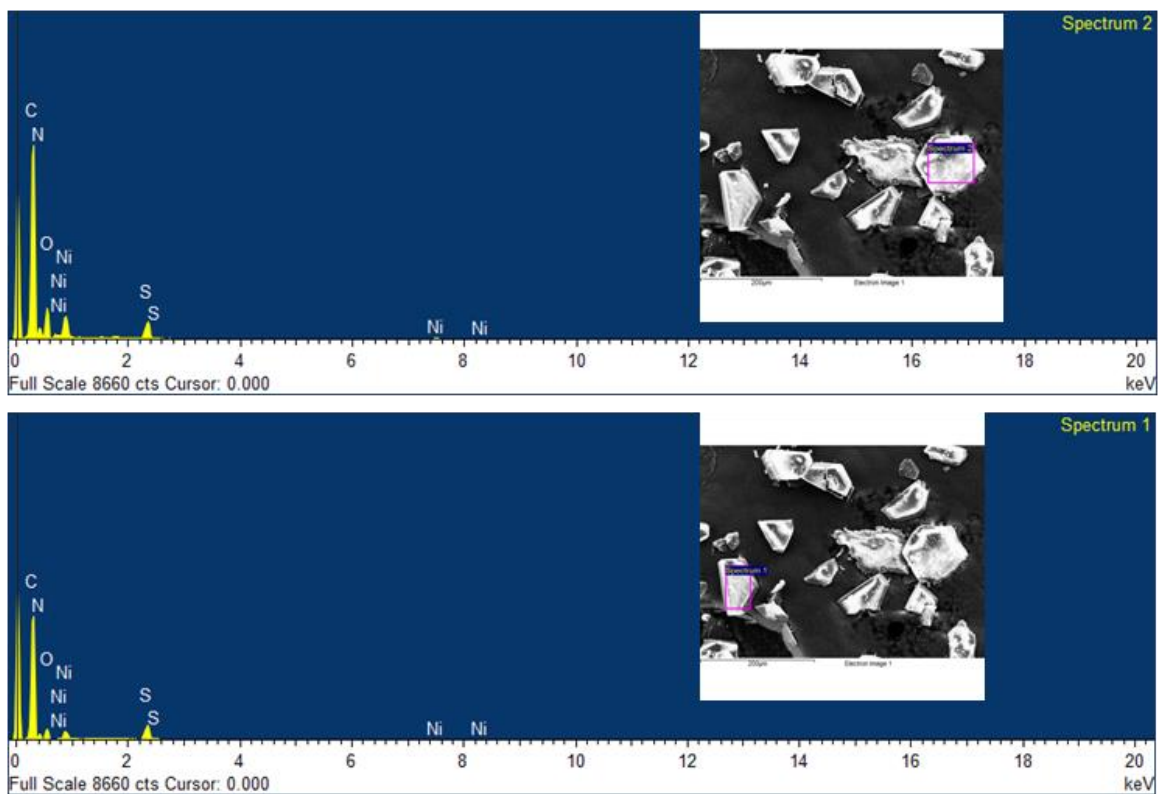
Figure S13: Characterization of IPM-MOF-201, related to Figure 1.
EDX spectra for compound **IPM-MOF-201**.
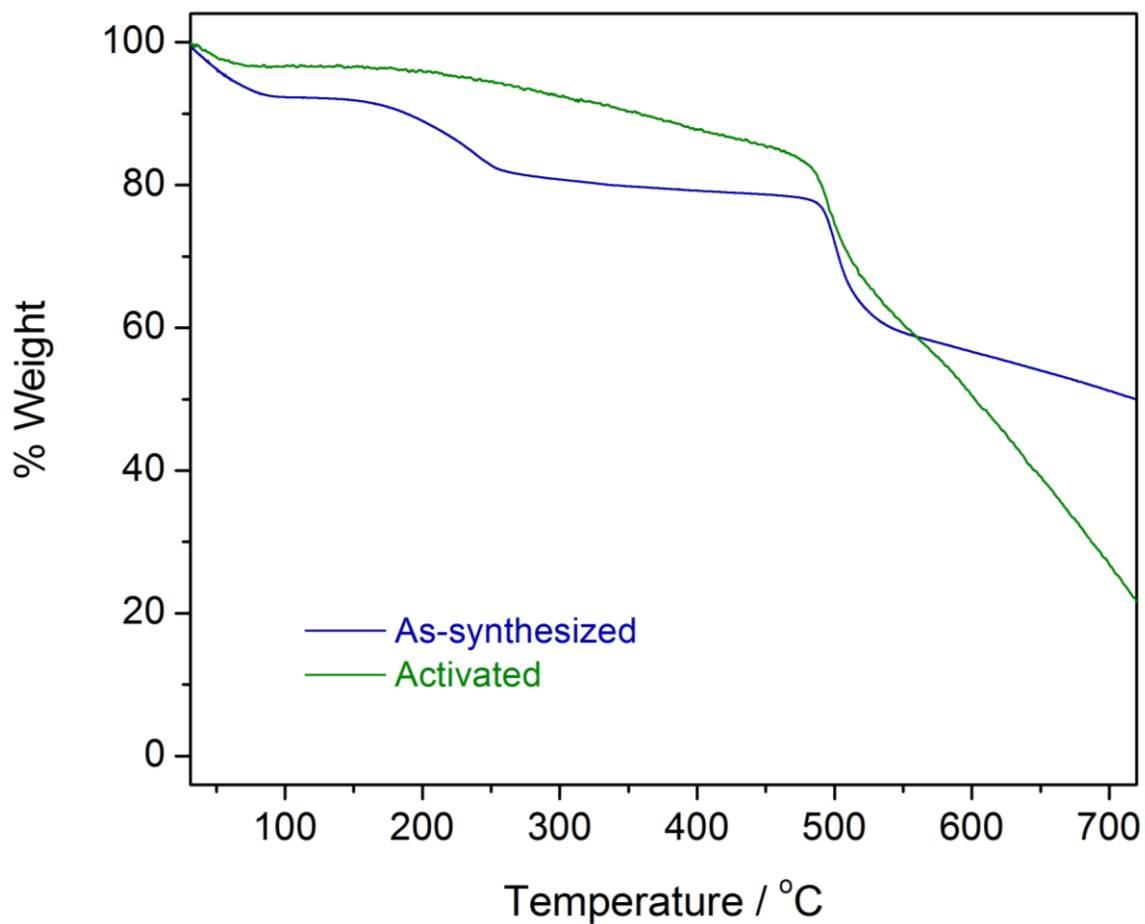
Figure S14: Characterization of IPM-MOF-201, related to Figure 1.
TGA profiles for compound **IPM-MOF-201**.
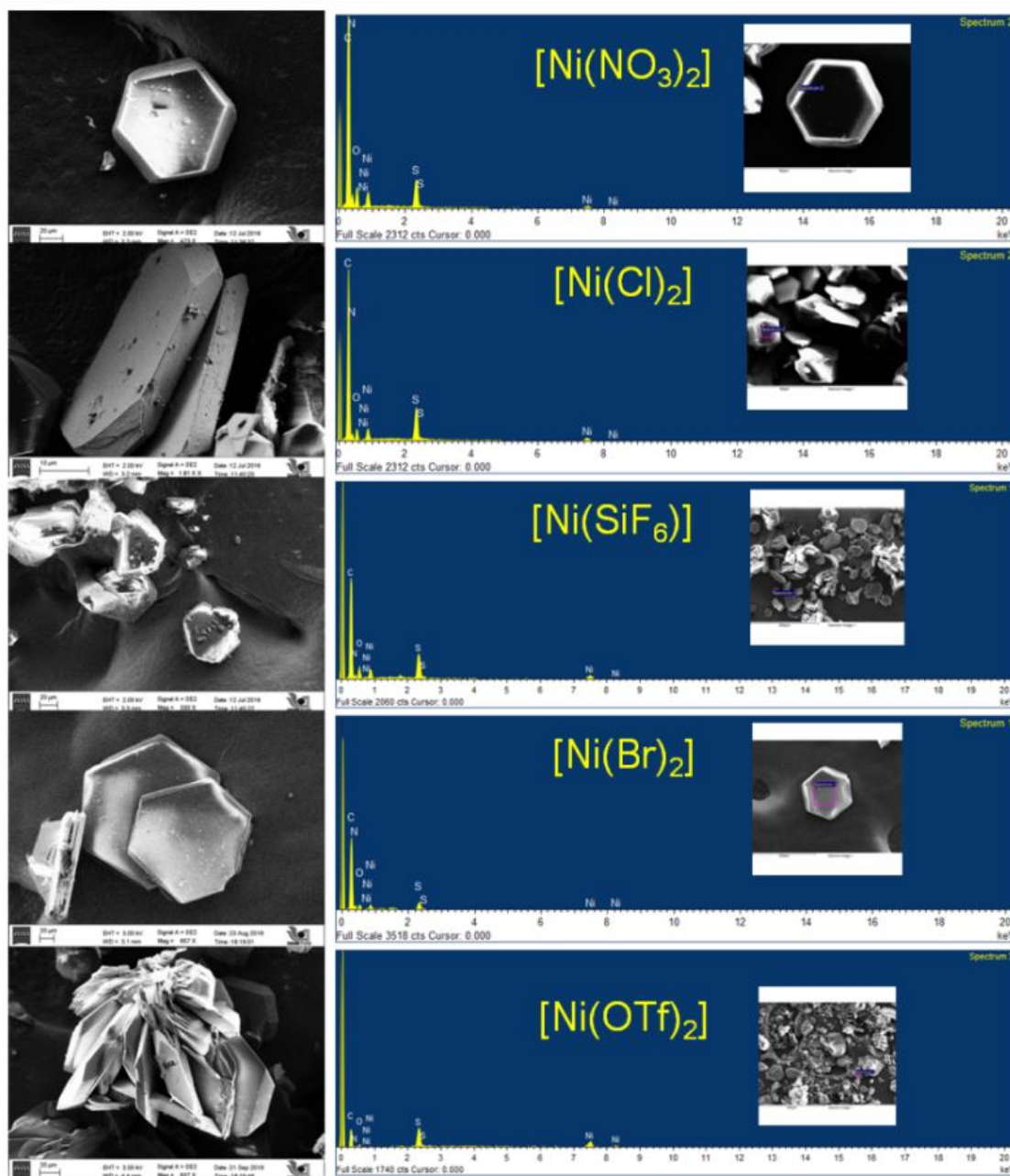
Figure S15: Characterization of IPM-MOF-201, related to Figure 1.
EDX spectra for compounds synthesized using different salts of Ni^{2+} and BPSA (excess).
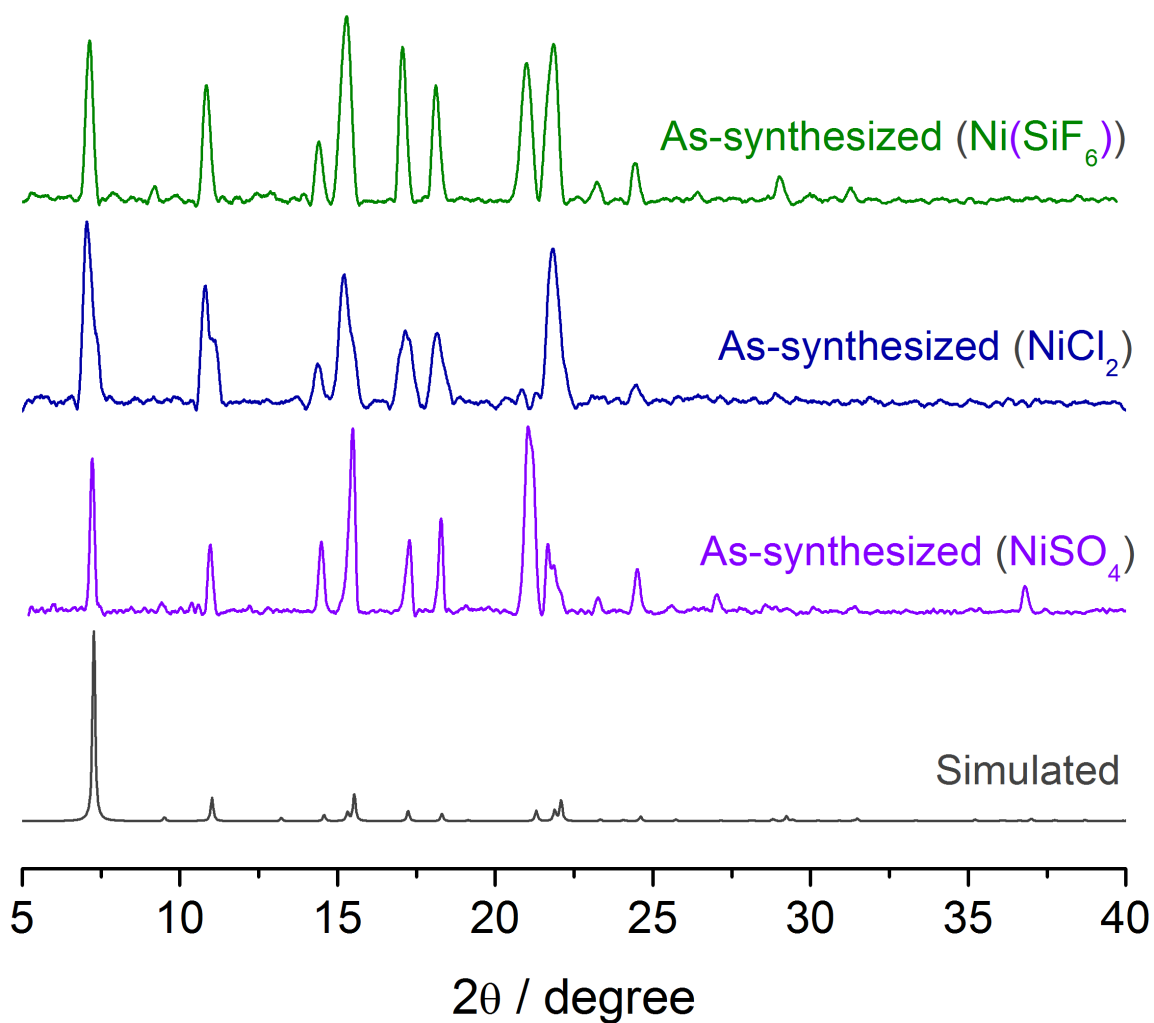
Figure S16: Characterization of IPM-MOF-201, related to Figure 1.
Powder X-ray diffraction patterns for compounds synthesized using different salts of Ni^{2+} and BPSA (excess).
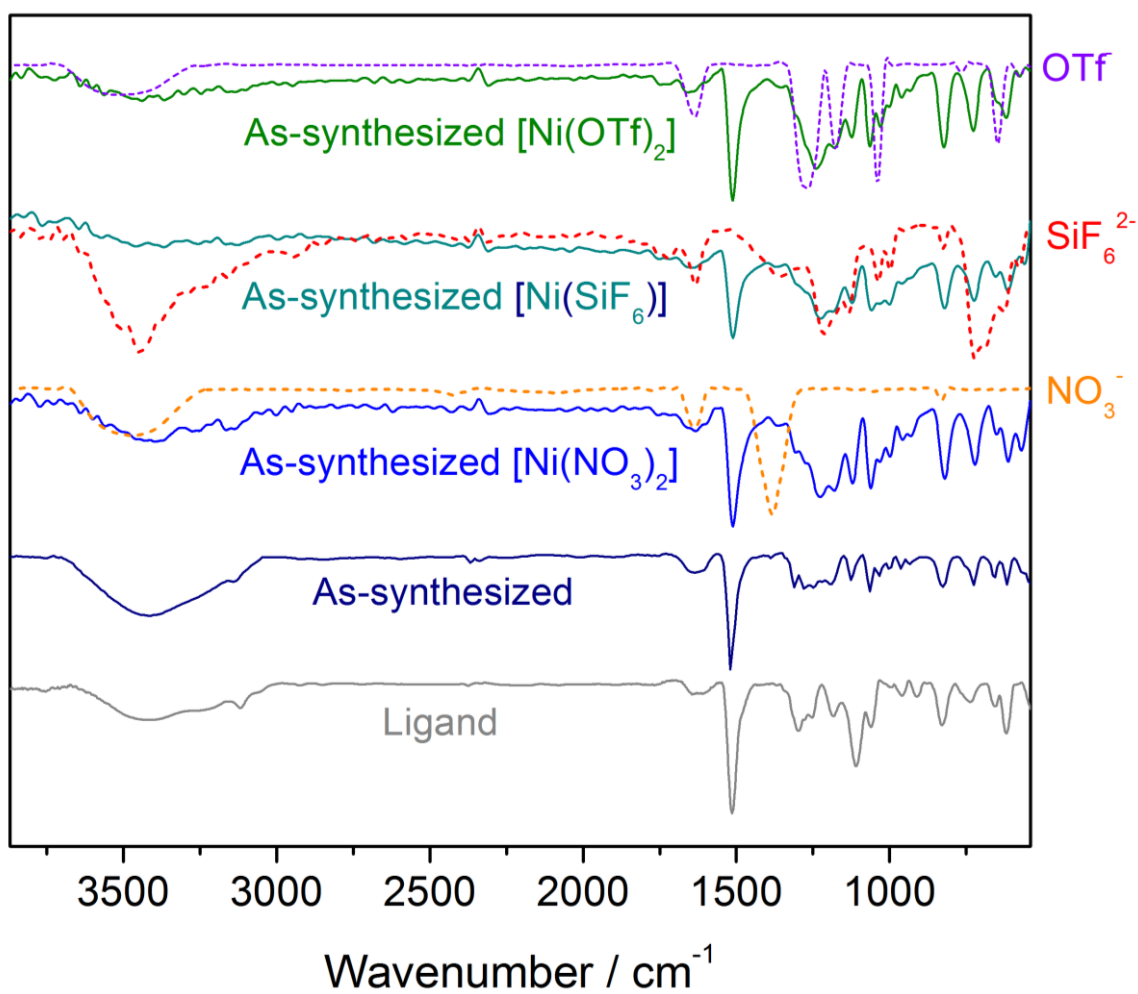
Figure S17: Characterization of IPM-MOF-201, related to Figure 1.
FT-IR spectra for compounds synthesized using different salts of Ni^{2+} and BPSA (excess). Dotted lines represent spectra for salts of respective anions.
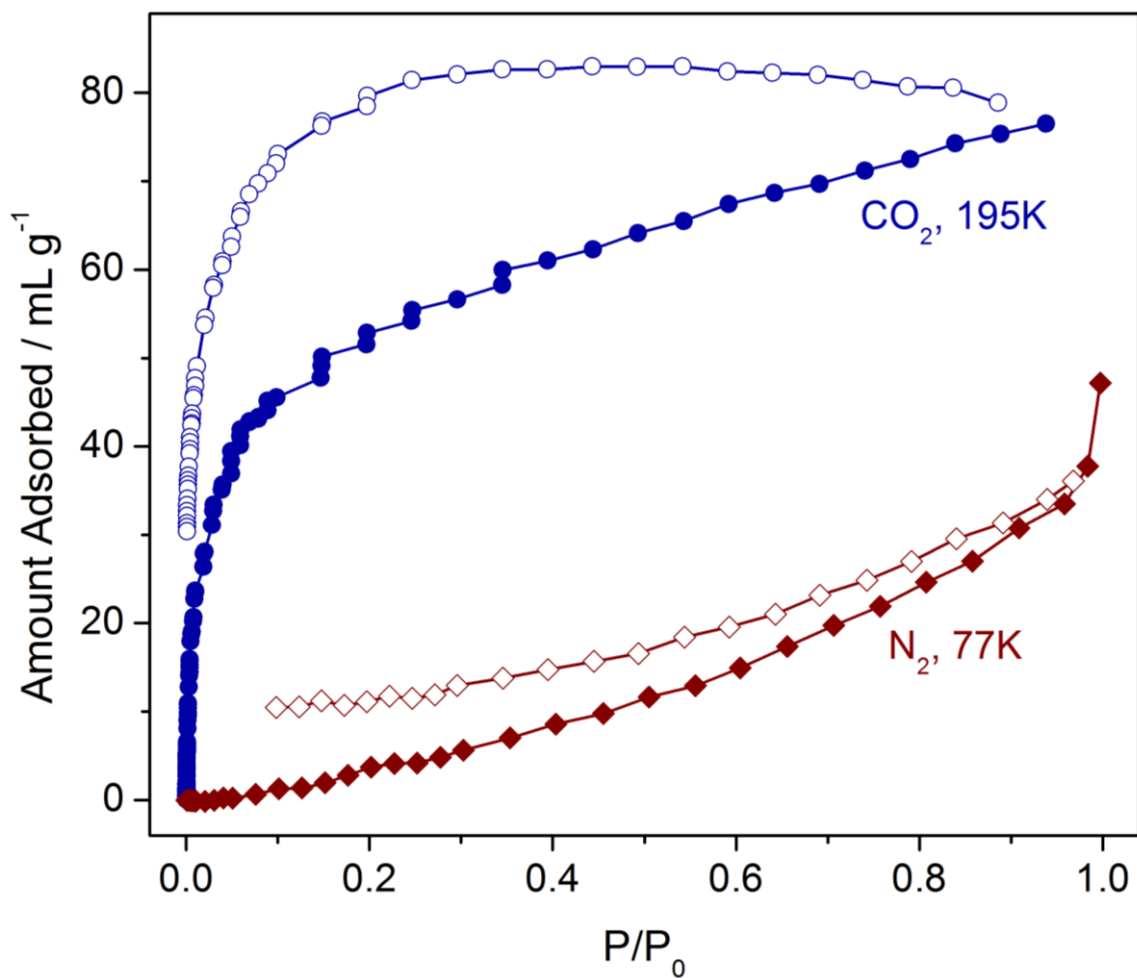
Figure S18: Gas adsorption of IPM-MOF-201, related to Figure 1.
Low temperature gas adsorption isotherms for compound **IPM-MOF-201**. Closed symbols denote adsorption while open symbols denote desorption.
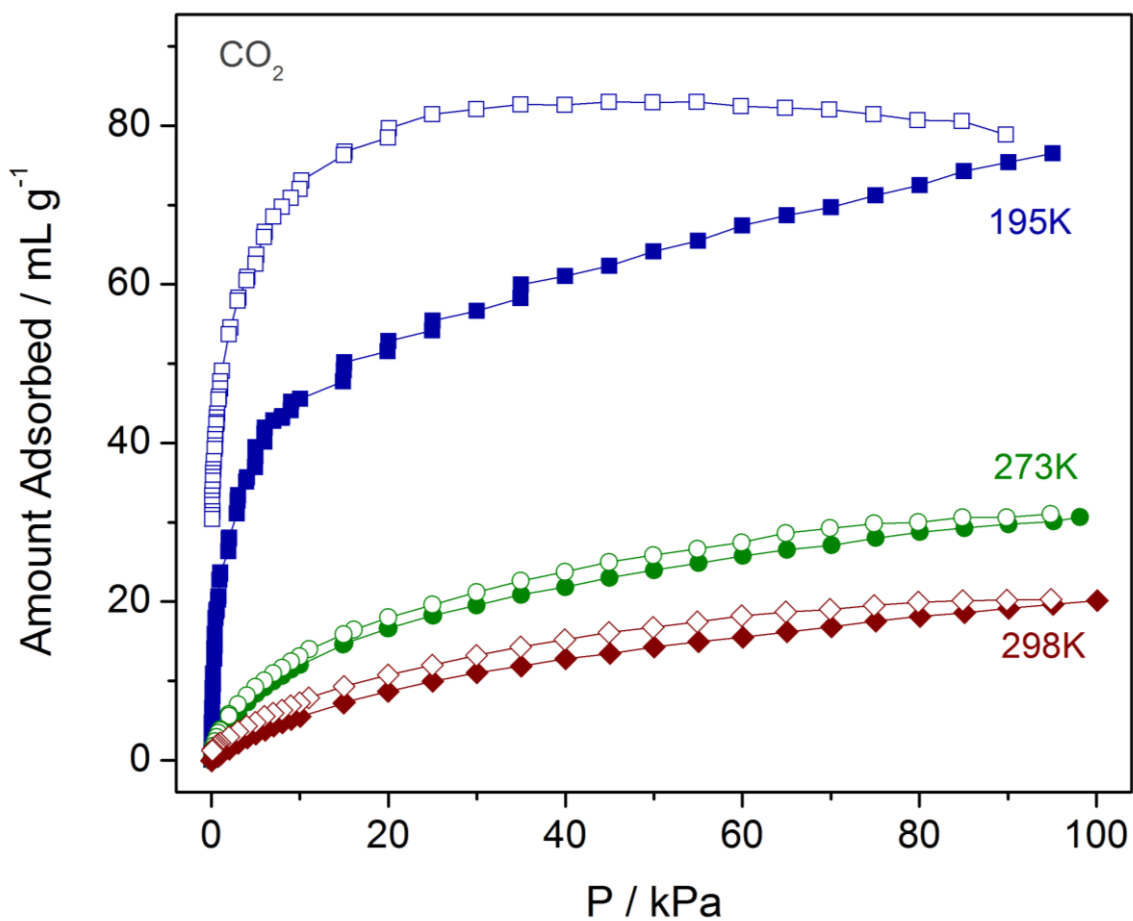
Figure S19: Gas adsorption of IPM-MOF-201, related to Figure 1.
CO₂ adsorption isotherms for compound **IPM-MOF-201** at different temperatures; 195K (blue), 273K (green), 298K (wine red). Closed symbols denote adsorption while open symbols denote desorption.
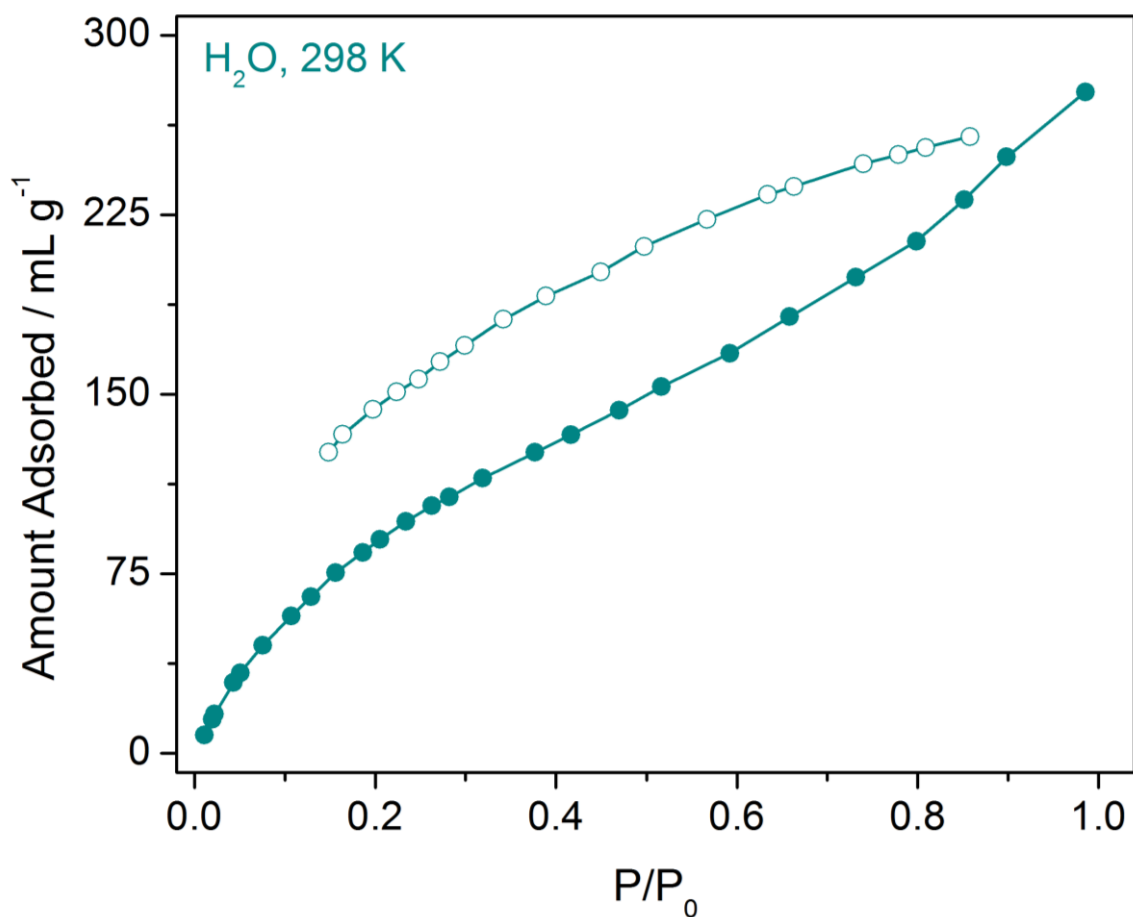
Figure S20: Vapour adsorption of IPM-MOF-201, related to Figure 2.
Water adsorption isotherm for compound **IPM-MOF-201** at 298K. Closed symbols denote adsorption while open symbols denote desorption.
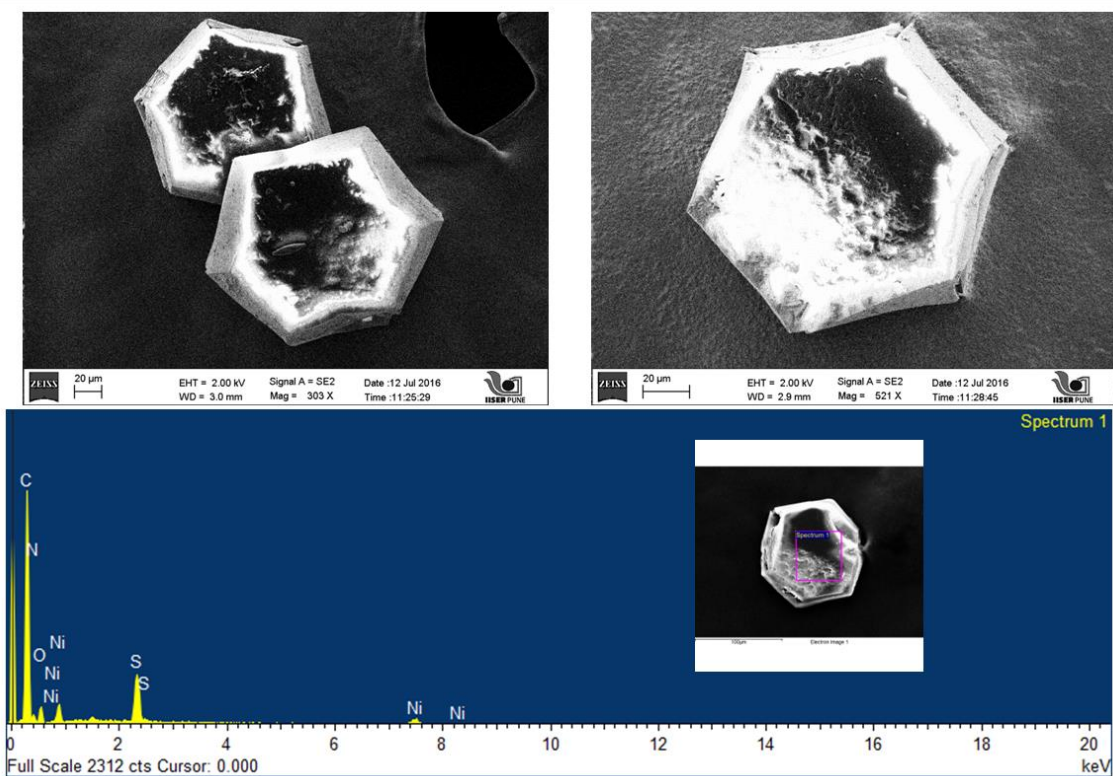
Figure S21: Stability Studies of IPM-MOF-201, related to Figure 2.
FESEM images (top) and EDX spectra (below; inset sample chosen for recording the EDX spectra) for compound **IPM-MOF-201** dipped in D.I. water for 1 month.
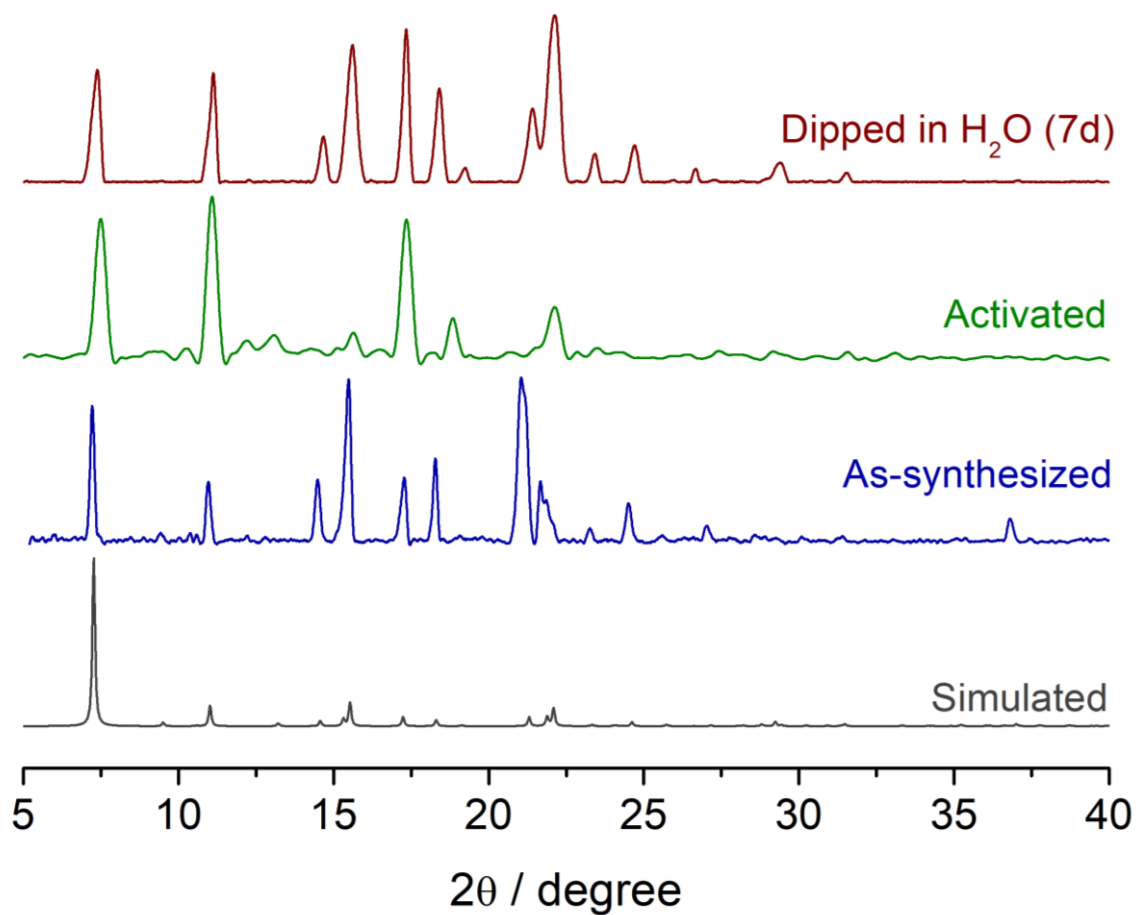
Figure S22: Stability Studies of IPM-MOF-201, related to Figure 2.
PXRD patterns for simulated (grey), as-synthesized (blue), activated (green) and water-dipped phases (wine red).
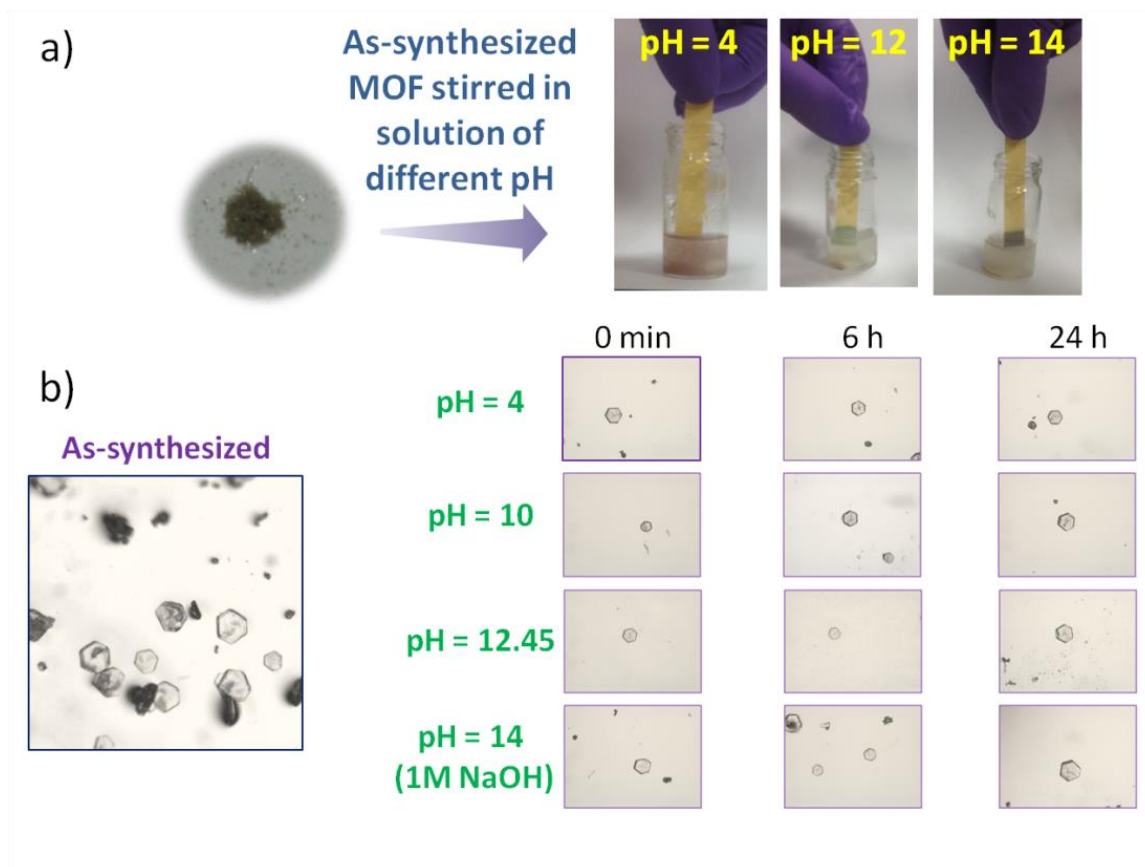
Figure S23: Stability Studies of IPM-MOF-201, related to Figure 2.
a) Photographs showing the experiment performed to check pH resistance, b) photographs taken under microscope for as-synthesized phase and the crystals upon dipping in solutions of different pH at varying time intervals.
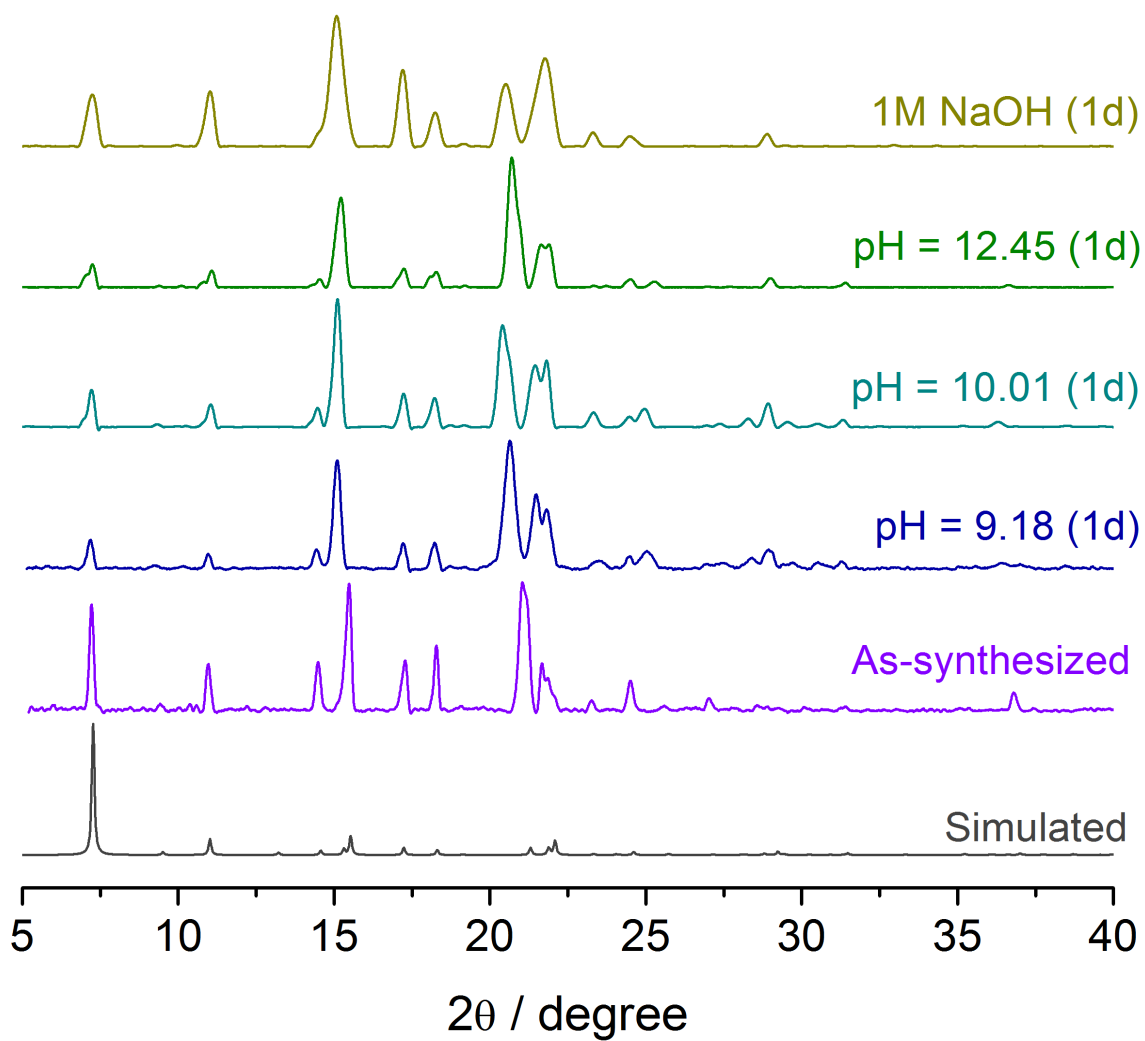
Figure S24: Stability Studies of IPM-MOF-201, related to Figure 2.
Powder x-ray diffractions patterns for simulated (grey), as-synthesized (purple), and compound **IPM-MOF-201** dipped in different pH conditions.
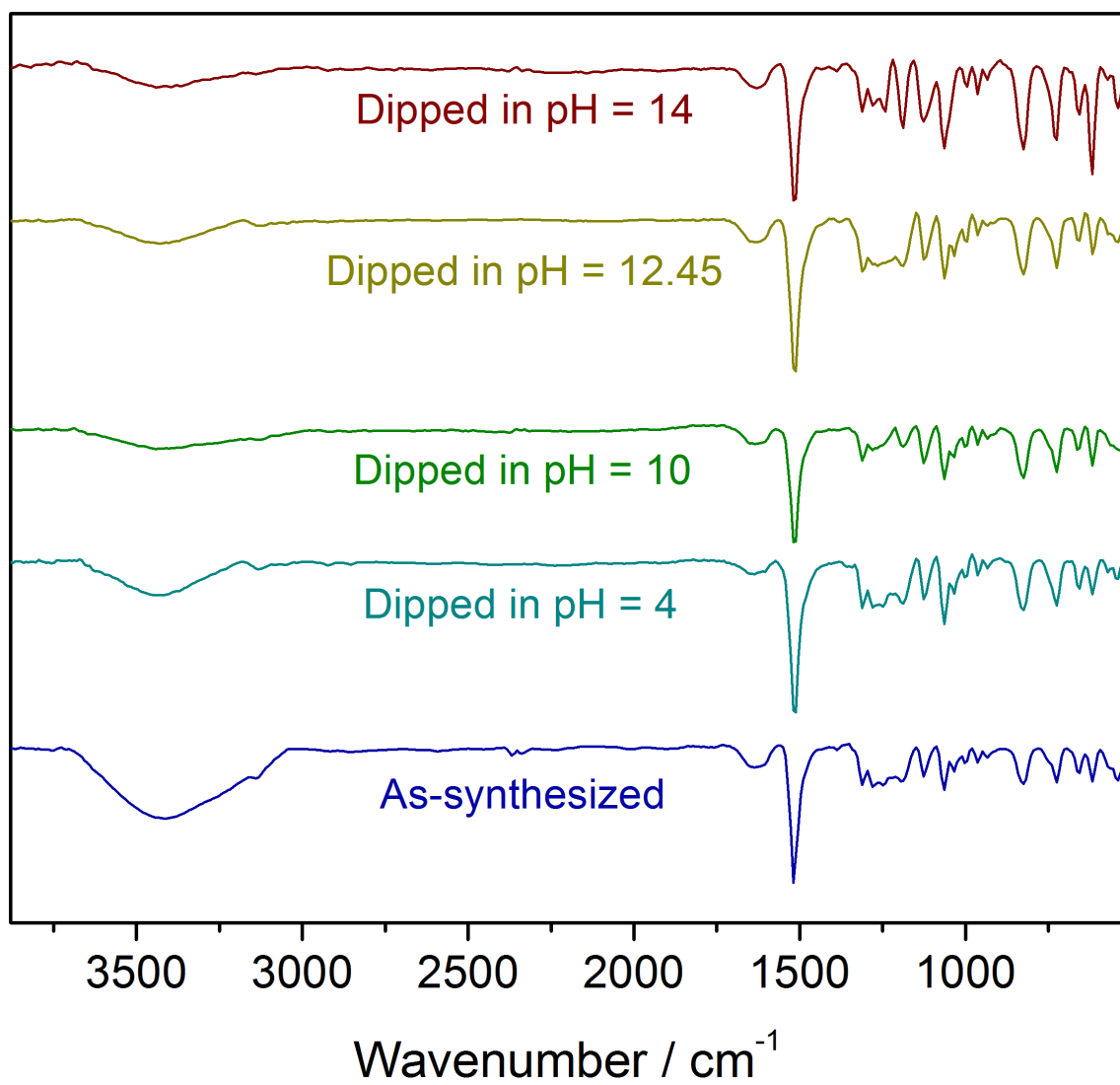
Figure S25: Stability Studies of IPM-MOF-201, related to Figure 2.
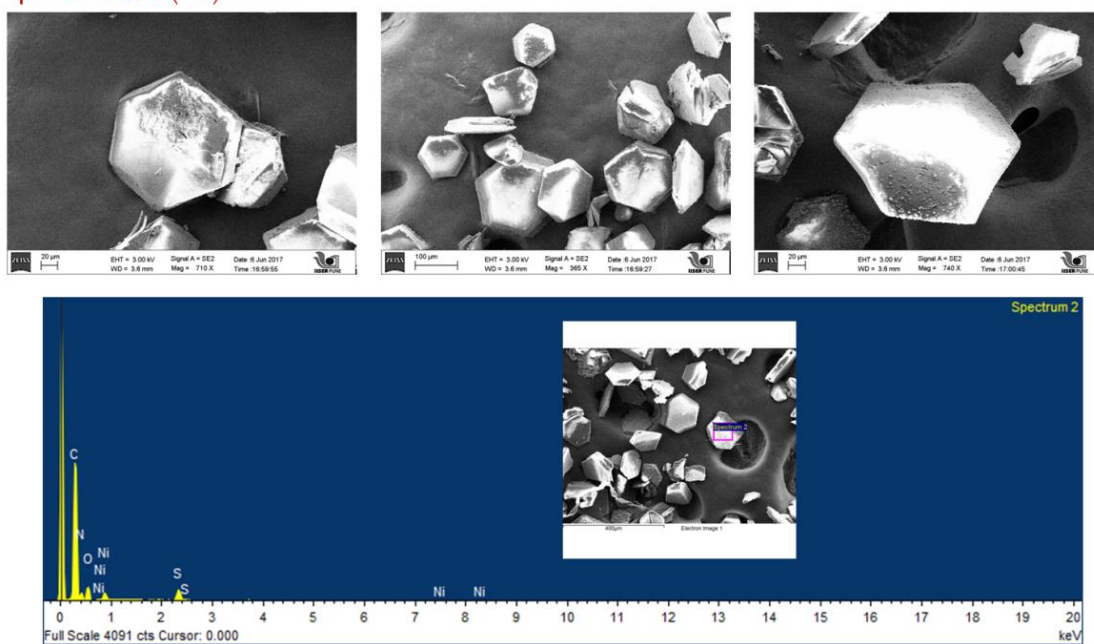FT-IR spectra for **IPM-MOF-201** dipped in different pH solutions.
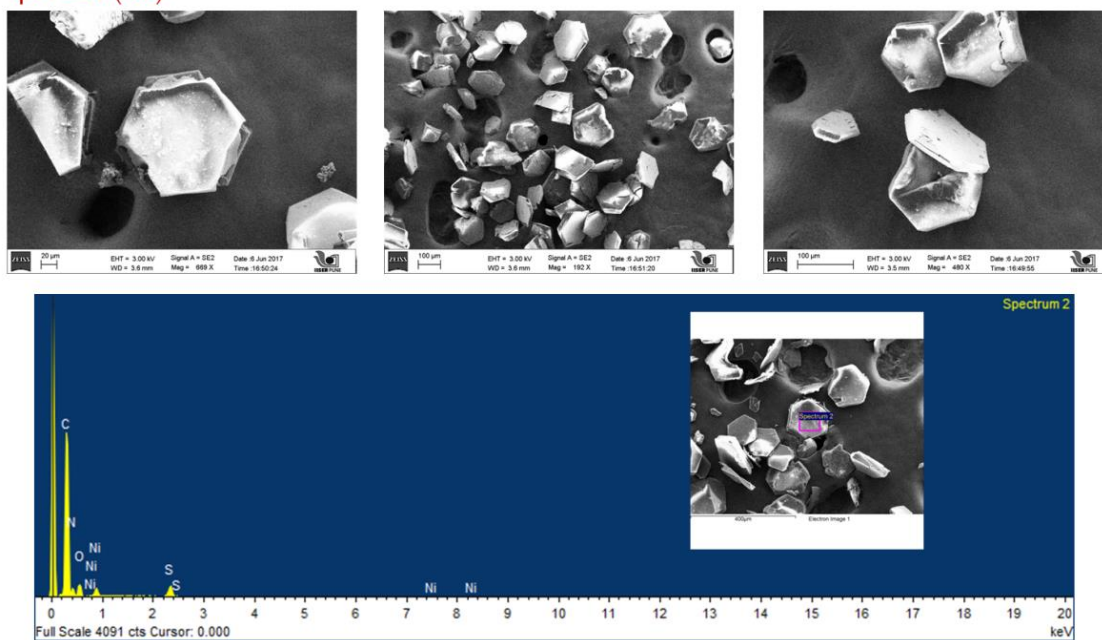
Figure S26: Stability Studies of IPM-MOF-201, related to Figure 2.
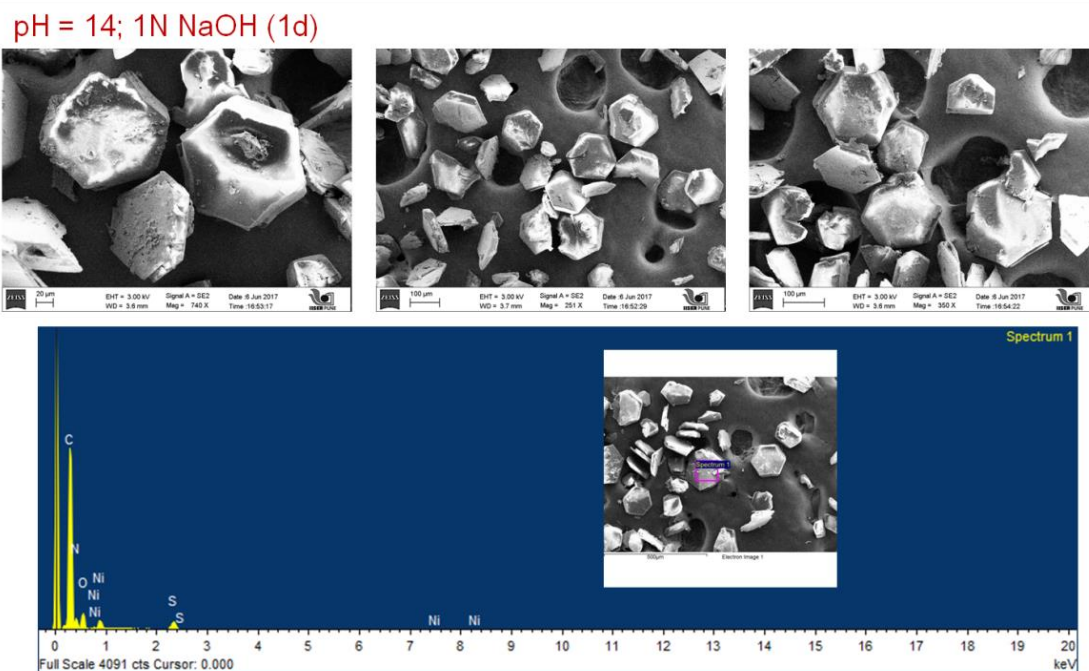FESEM images of compound **IPM-MOF-201** dipped in solution of pH = 4 & corresponding EDX profile.
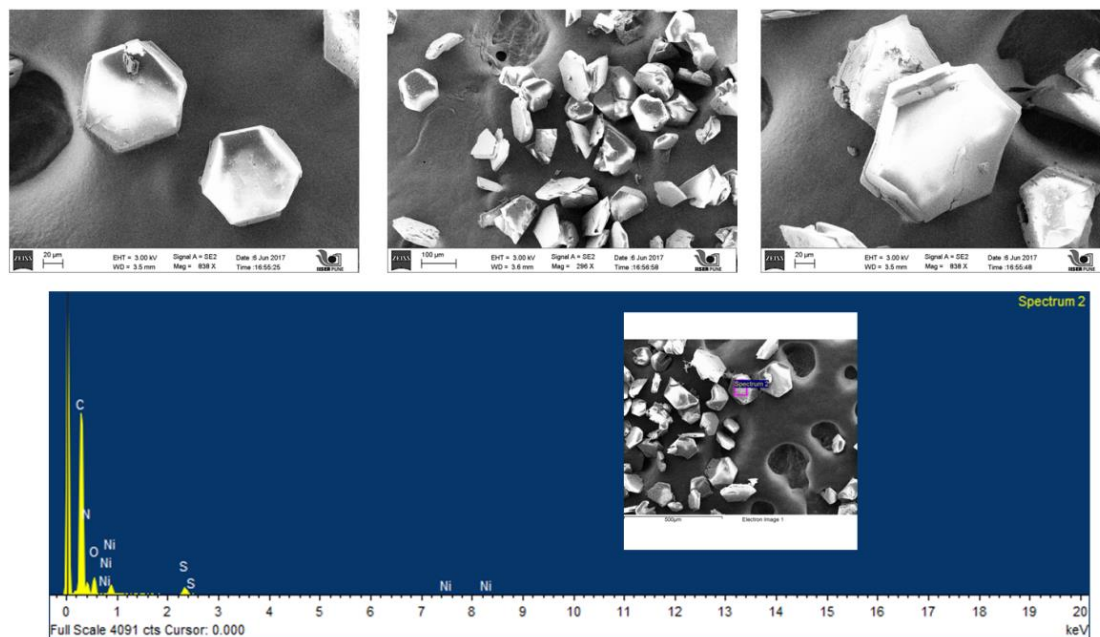
Figure S27: Stability Studies of IPM-MOF-201, related to Figure 2.
FESEM images of compound **IPM-MOF-201** dipped in solution of pH = 10.01 & corresponding EDX profile.

Figure S28: Stability Studies of IPM-MOF-201, related to Figure 2.
FESEM images of compound **IPM-MOF-201** dipped in solution of pH = 12.45 & corresponding EDX profile.

Figure S29: Stability Studies of IPM-MOF-201, related to Figure 2.
FESEM images of compound **IPM-MOF-201** dipped in solution of pH = 14 (1N NaOH) &
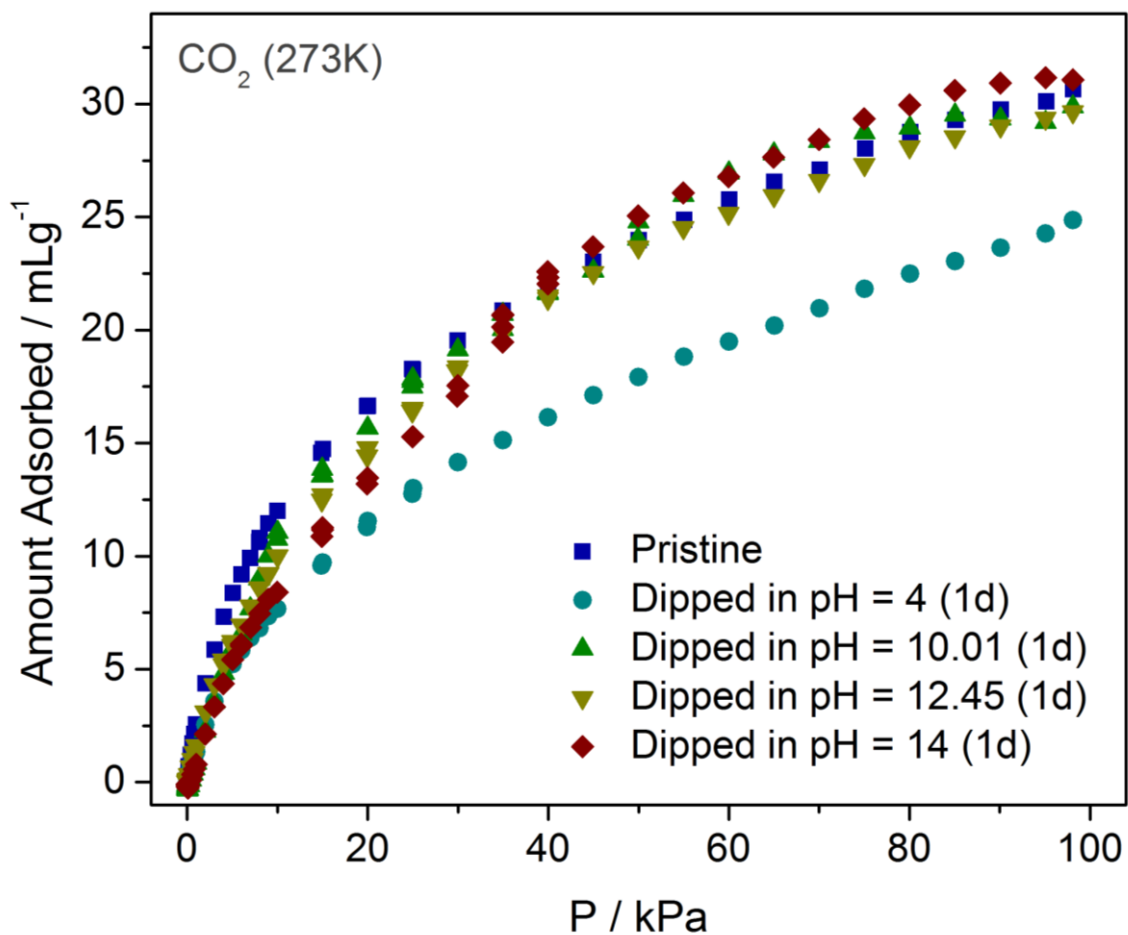corresponding EDX profile.

Figure S30: Stability Studies of IPM-MOF-201, related to Figure 2.
CO_2 adsorption isotherms at 273K for compound **IPM-MOF-201** dipped in different conditions.
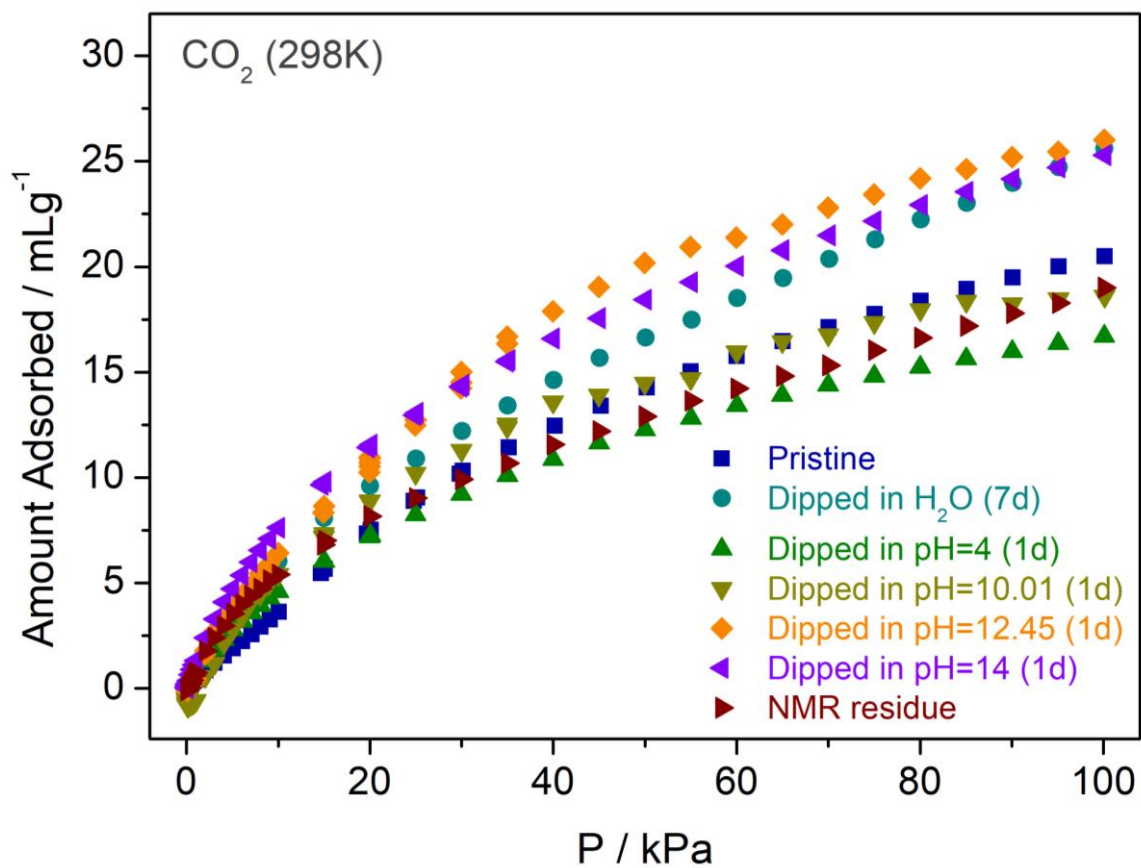
Figure S31: Stability Studies of IPM-MOF-201, related to Figure 2.
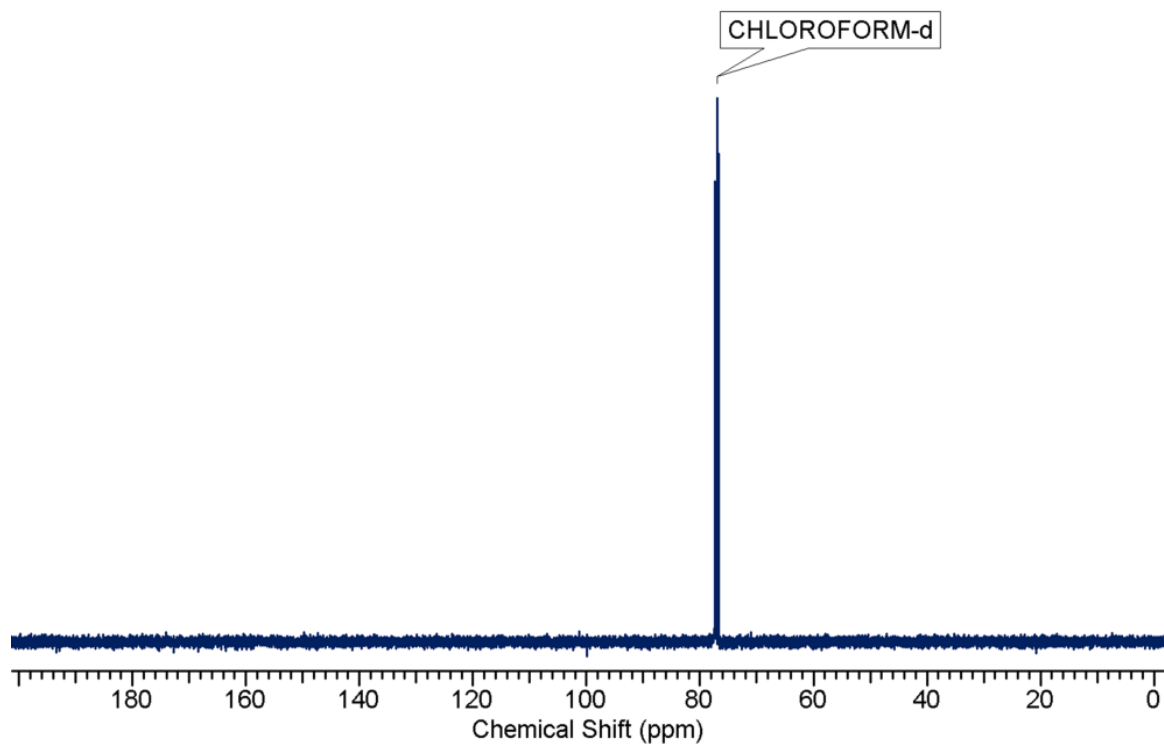CO_2 adsorption isotherms at 298K for compound **IPM-MOF-201** dipped in different conditions.

Figure S32: Stability Studies of IPM-MOF-201, related to Figure 2.
^{13}C-NMR of the supernatant obtained after treating **IPM-MOF-201** in solution of NaOD/D$_2$O for 1 day.
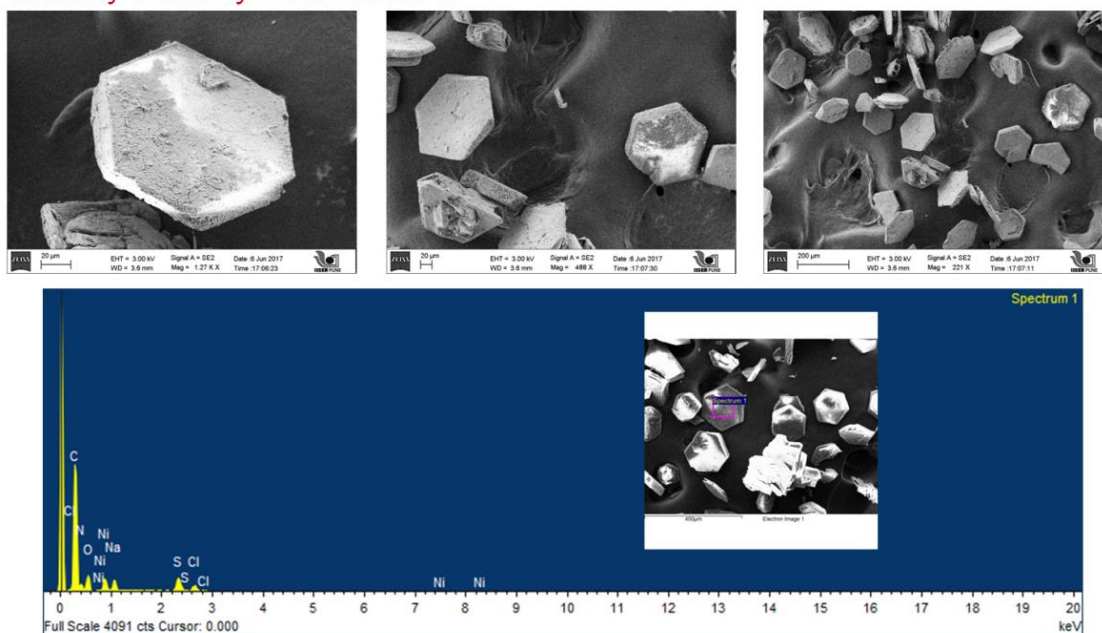
Figure S33: Stability Studies of IPM-MOF-201, related to Figure 2.

 FESEM images of compound **IPM-MOF-201** & corresponding EDX profile after performing the NMR characterization experiment.
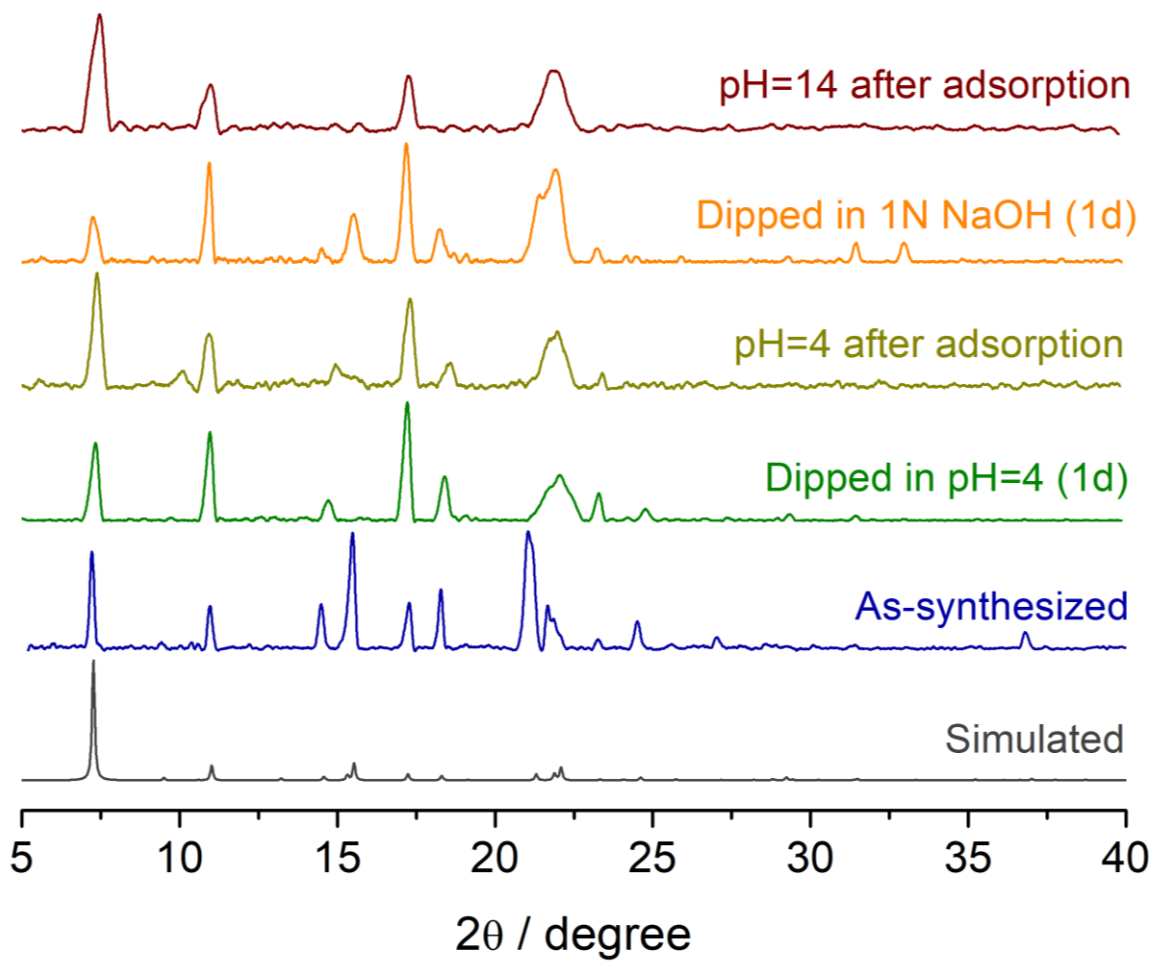
Figure S34: Stability Studies of IPM-MOF-201, related to Figure 2.
PXRD patterns for the pH dipped conditions and the post-adsorption phases.

Figure S35: Stability Studies of IPM-MOF-201, related to Figure 2.
Powder diffraction patterns for compound **IPM-MOF-201(Ni)** (simulated, grey), Co-MOF (simulated, purple) [simulated pattern adapted from ref. (Yao et al., 2011)], as-synthesized **IPM-MOF-201(Co)** (blue) and phase dipped in pH=12.45 (green) and pH=14 (wine red).

Figure S36: Stability Studies of IPM-MOF-201, related to Figure 2.
Photographs of Co-IPM-MOF when dipped in pH solutions of 4, 12.45 and 14 at different time intervals.
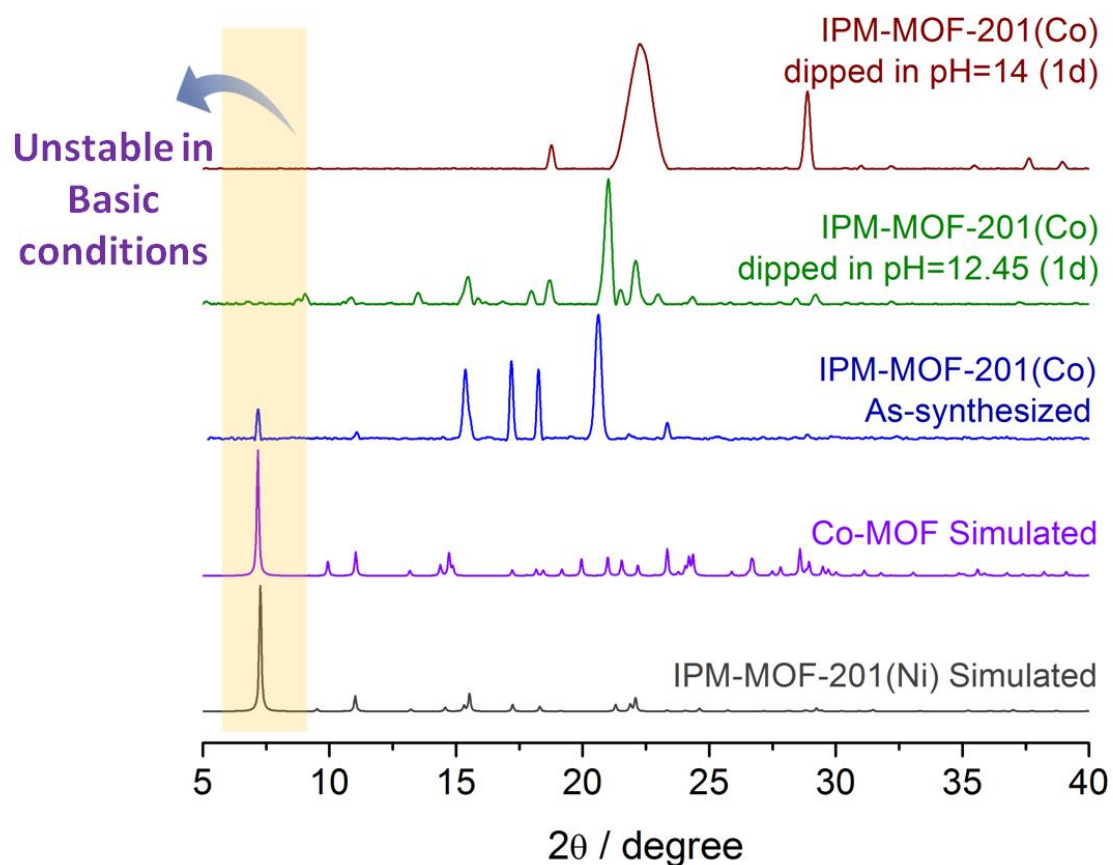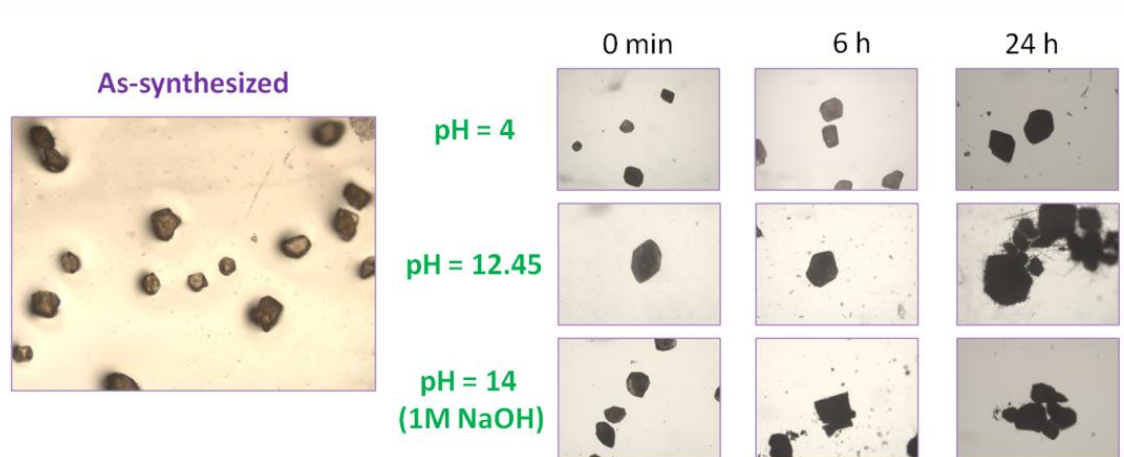
Figure S37: Stability Studies of IPM-MOF-201, related to Figure 2.
Powder diffraction patterns for compound **IPM-MOF-201(Ni)** (simulated, grey), Co-MOF (simulated, blue) [simulated pattern adapted from ref. (Yao et al., 2011)], as-synthesized Co-MOF (cyan), phase dipped in pH=12.45 (green) and pH=14 (yellow), and ligand (wine red).
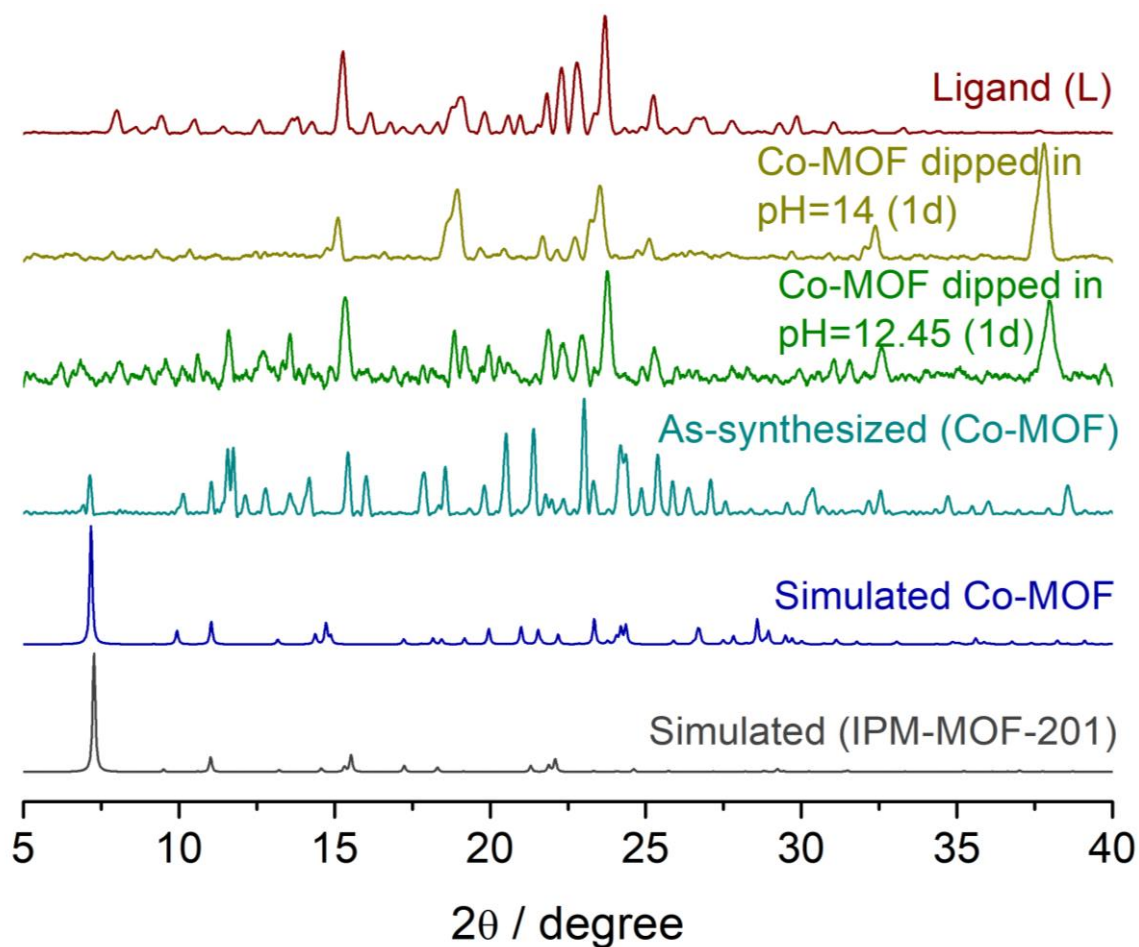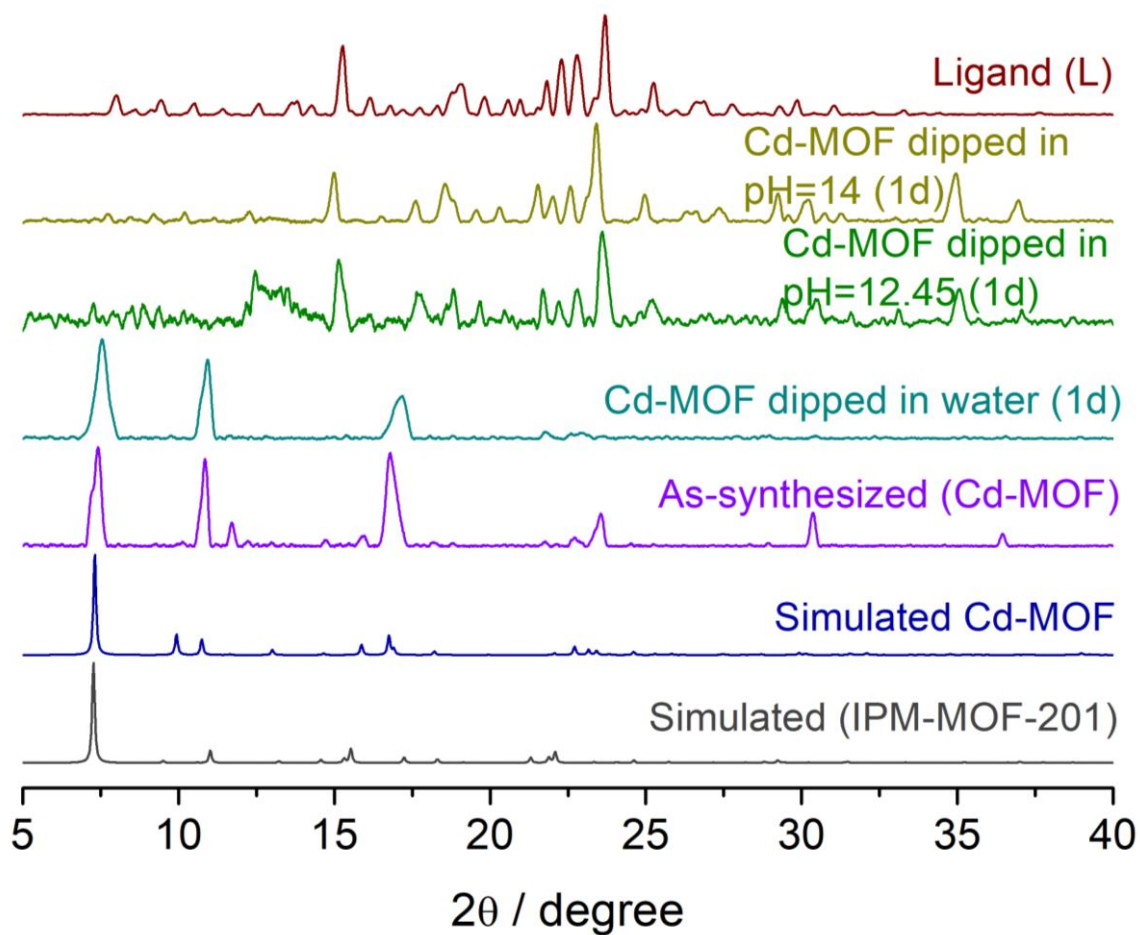
Figure S38: Stability Studies of IPM-MOF-201, related to Figure 2.
Powder diffraction patterns for compound **IPM-MOF-201(Ni)** (simulated, grey), Cd-MOF (simulated, blue) [simulated pattern adapted from ref. (Liu et al., 2014)], as-synthesized Cd-MOF (purple), dipped in water (cyan), phase dipped in pH=12.45 (green) and pH=14 (yellow), and ligand (wine red).
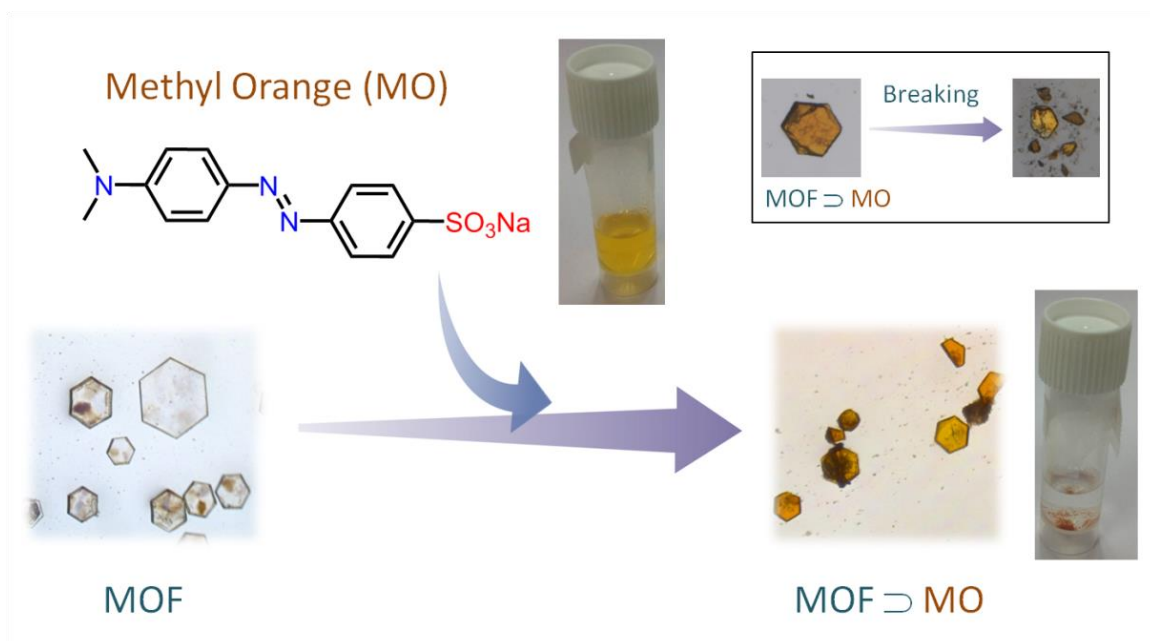
Figure S39: Dye capture studies by IPM-MOF-201, related to Figure 3.
Schematic illustration of dye inclusion (Methyl Orange - MO) in compound **IPM-MOF-201**. The corresponding photographs of the crystals under the microscope have been shown alongside. (Inset) The photograph of MO-exchanged crystals and the fragments after breaking it randomly.
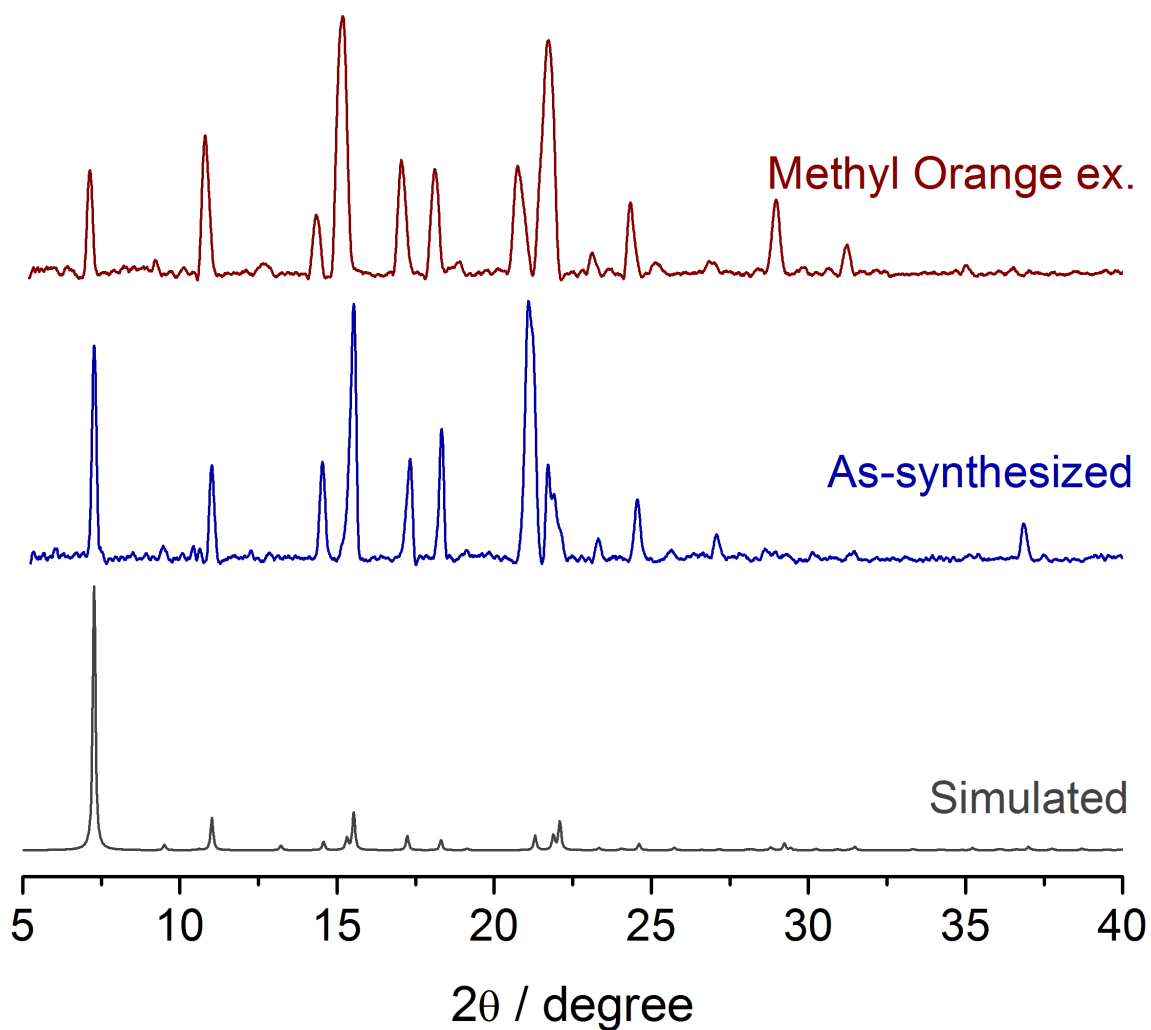
Figure S40: Dye capture studies by IPM-MOF-201, related to Figure 3.
Powder diffraction patterns for compound **IPM-MOF-201** (simulated, grey), as-synthesized (blue) and MO-exchange phase (wine red).

Figure S41: Dye capture studies by IPM-MOF-201, related to Figure 3.
UV-Vis spectra of the supernatant aqueous MO solution after addition of compound **IPM-MOF-201** at different time intervals.
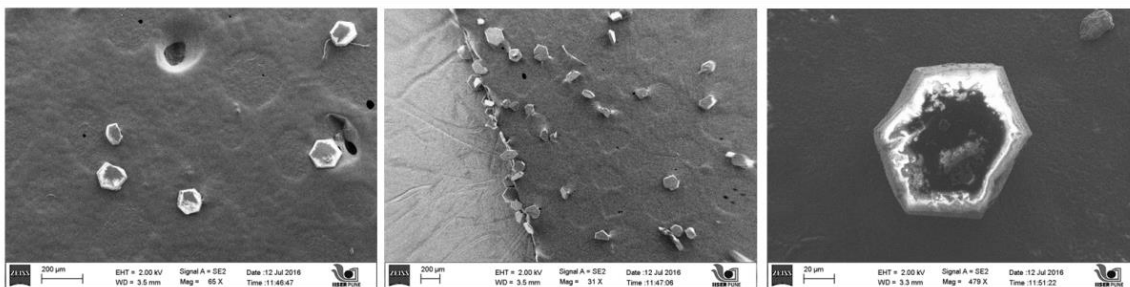
Figure S42: Dye capture studies by IPM-MOF-201, related to Figure 3.
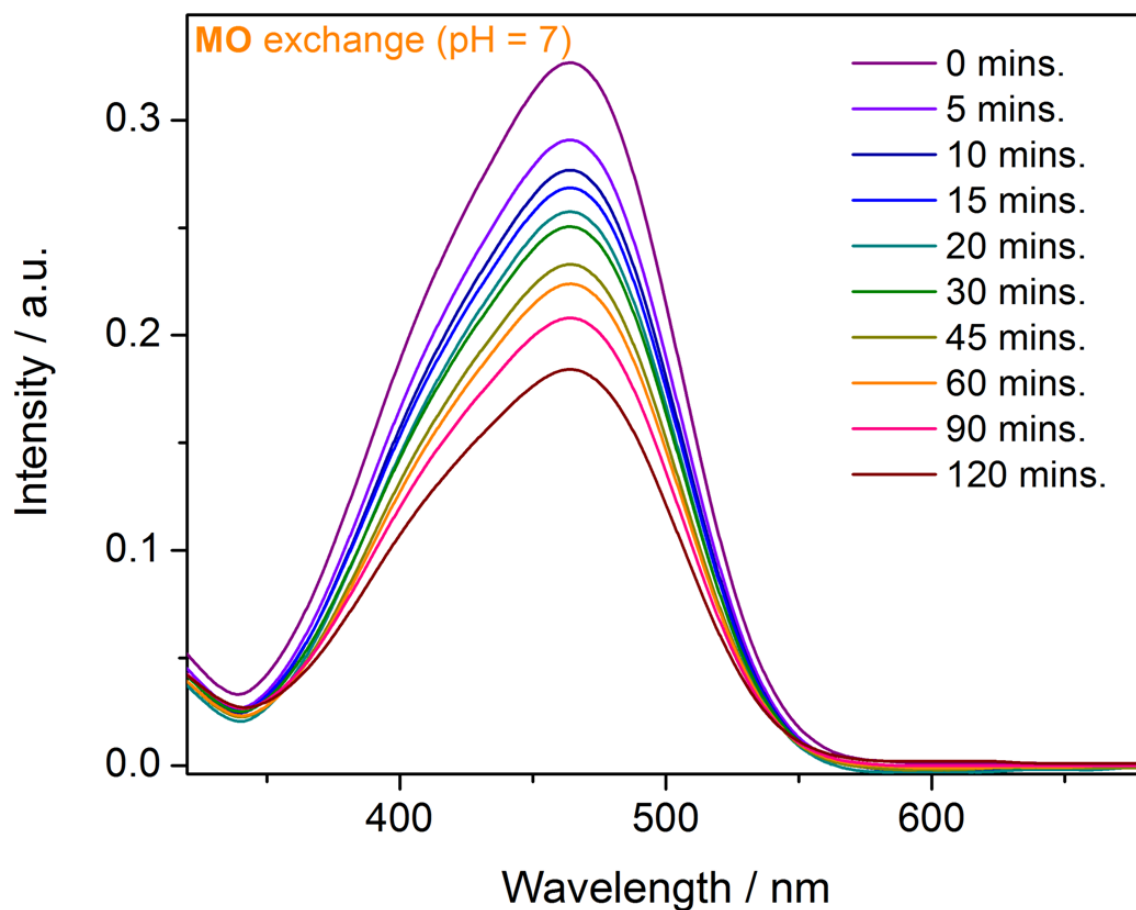FESEM images of compound **IPM-MOF-201** dipped in aqueous MO solution.

Figure S43: Dye capture studies by IPM-MOF-201, related to Figure 3.
UV-Vis spectra of the supernatant aqueous MB solution after addition of compound **IPM-MOF-201** at different time intervals.

Figure S44: Dye capture studies by IPM-MOF-201, related to Figure 3.
UV-Vis spectra of the supernatant MO solution having pH a) 4.01, b) 10.01 and c) 12.45, after addition of compound **IPM-MOF-201** to respective phases at different time intervals.
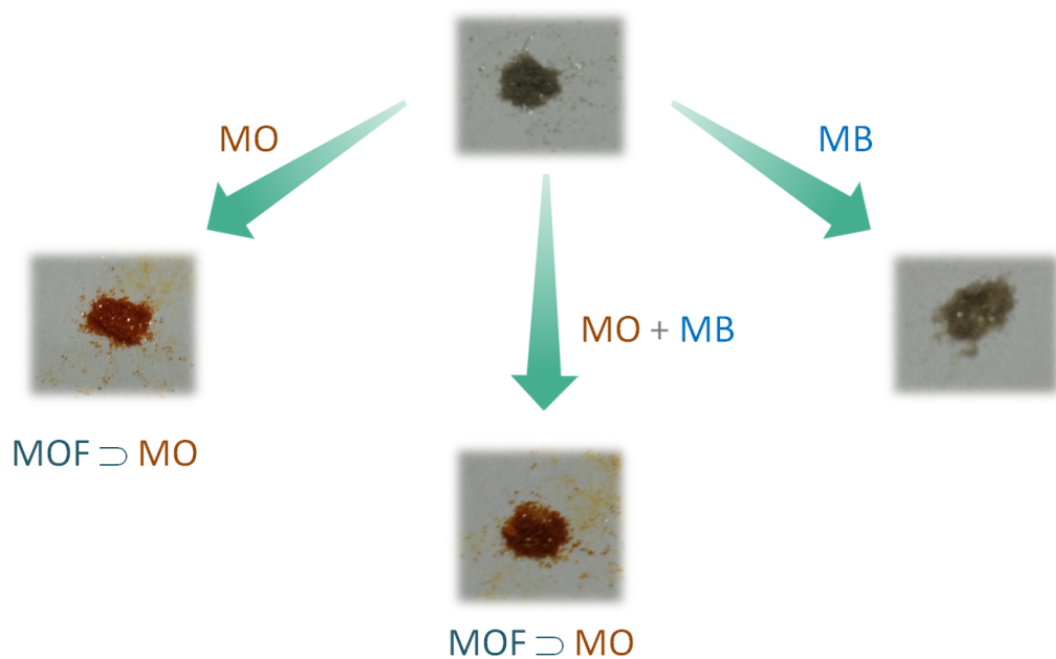
Figure S45: Dye capture studies by IPM-MOF-201, related to Figure 3.
Photographs showing preferential capture of anionic dye over cationic dye, even in presence of equimolar mixture of both dyes.
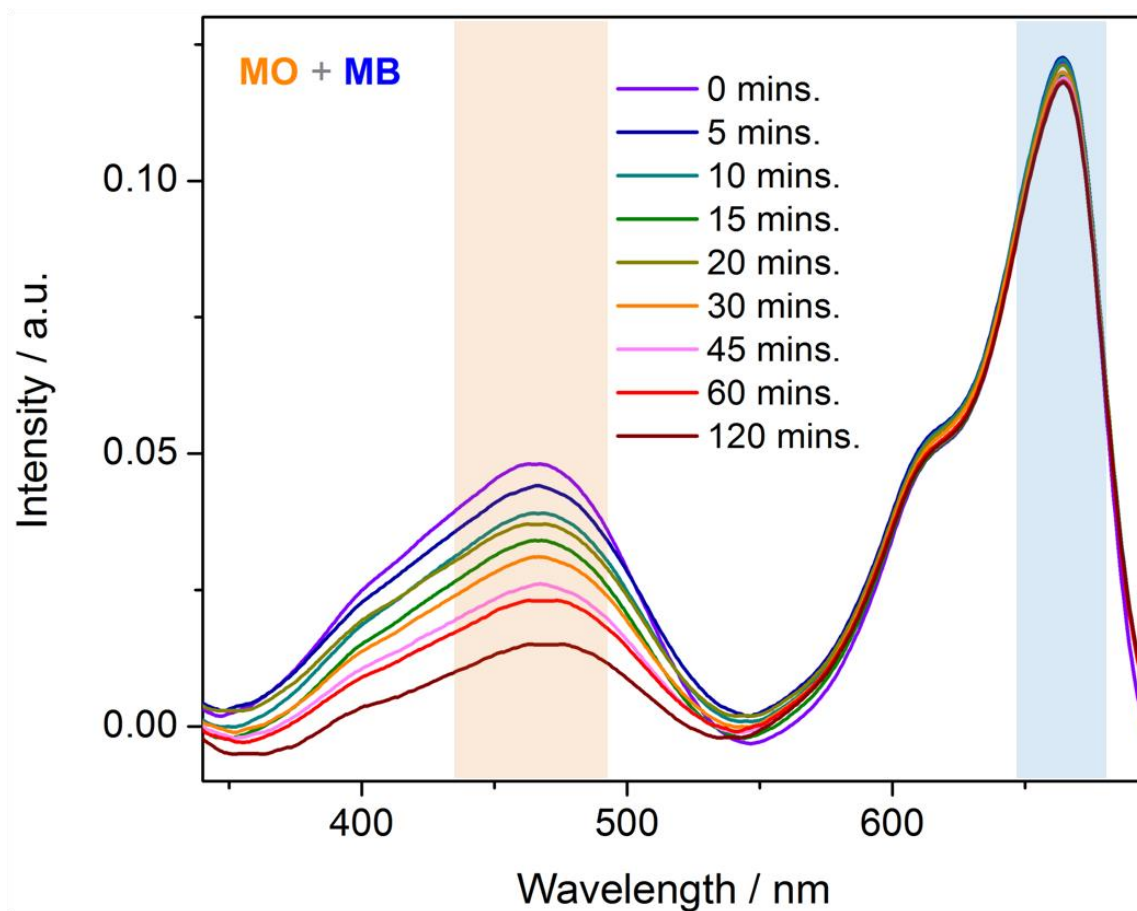
Figure S46: Dye capture studies by IPM-MOF-201, related to Figure 3.
UV-Vis spectra of the supernatant solution of equimolar mixture of MB & MO after addition
of compound **IPM-MOF-201** recorded at different time intervals.
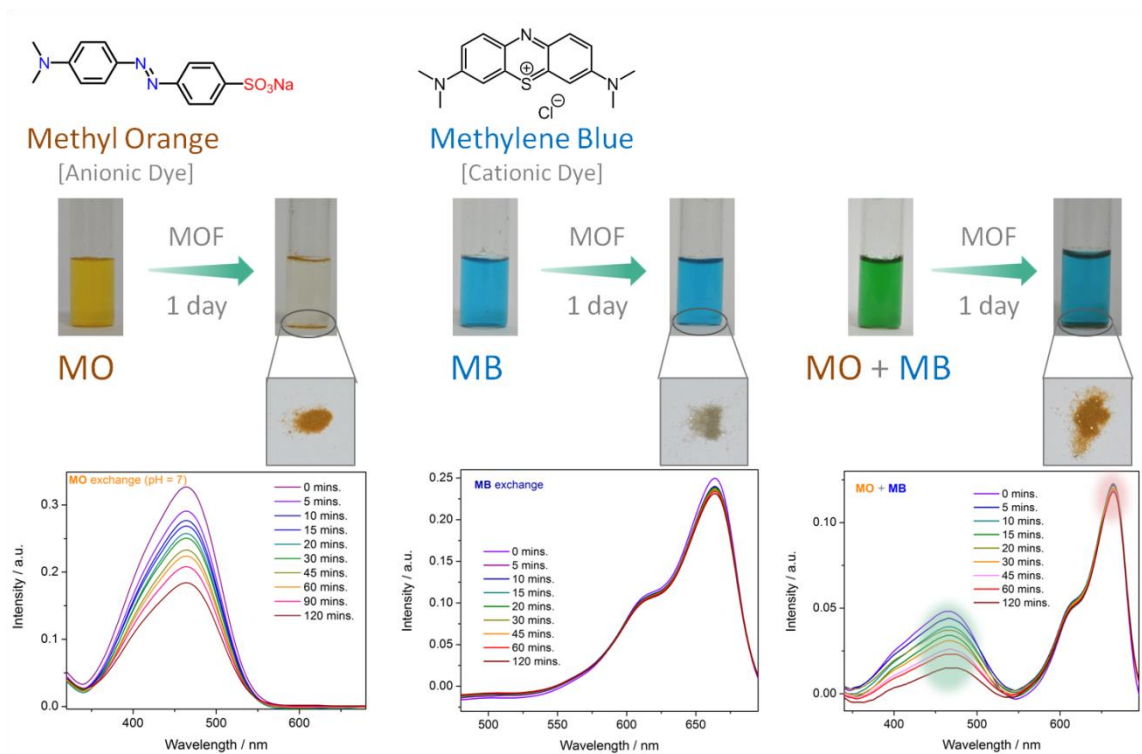
Figure S47: Dye capture studies by IPM-MOF-201, related to Figure 3.
Overall representation of the charge selective dye capture by **IPM-MOF-201**.

Figure S48: Dye capture studies by IPM-MOF-201, related to Figure 3.
UV-Vis spectra of the supernatant MB solution of pH = 10.01 after addition of compound **IPM-MOF-201** recorded at different time intervals.
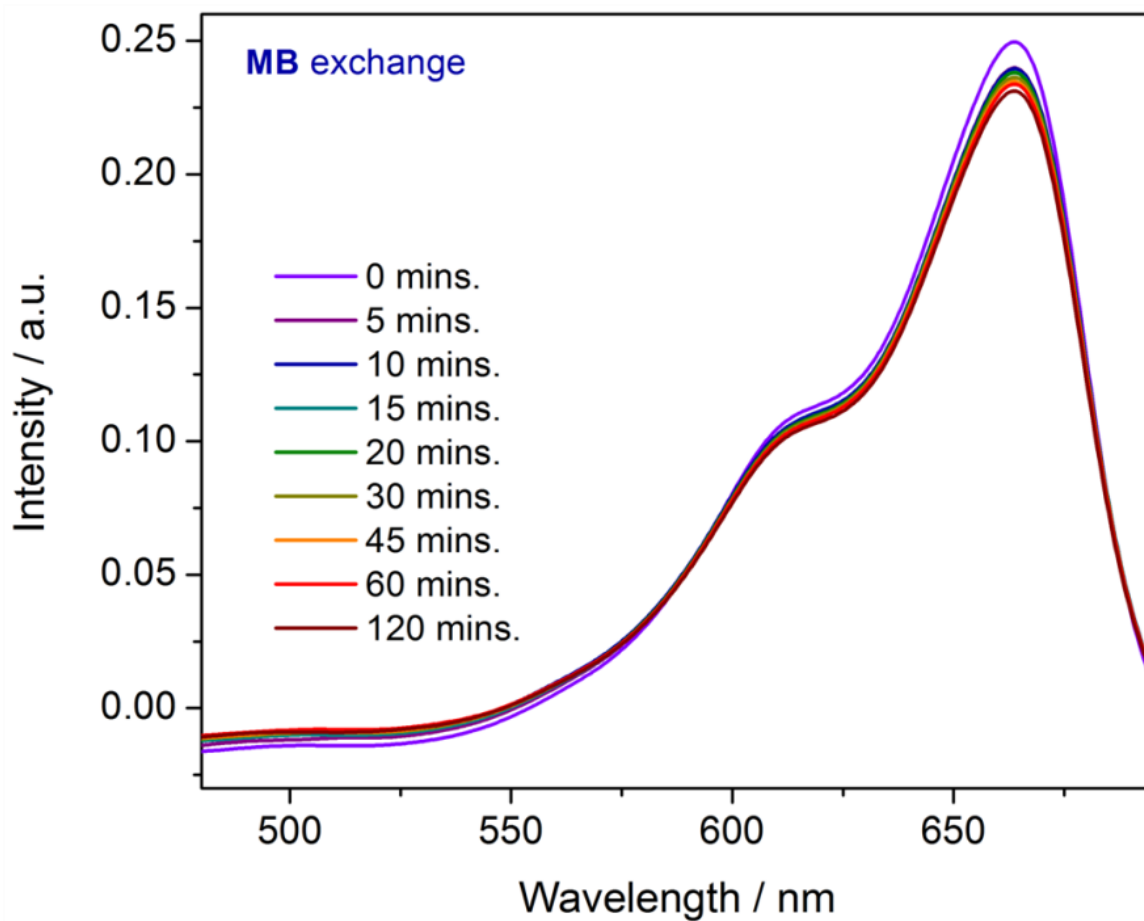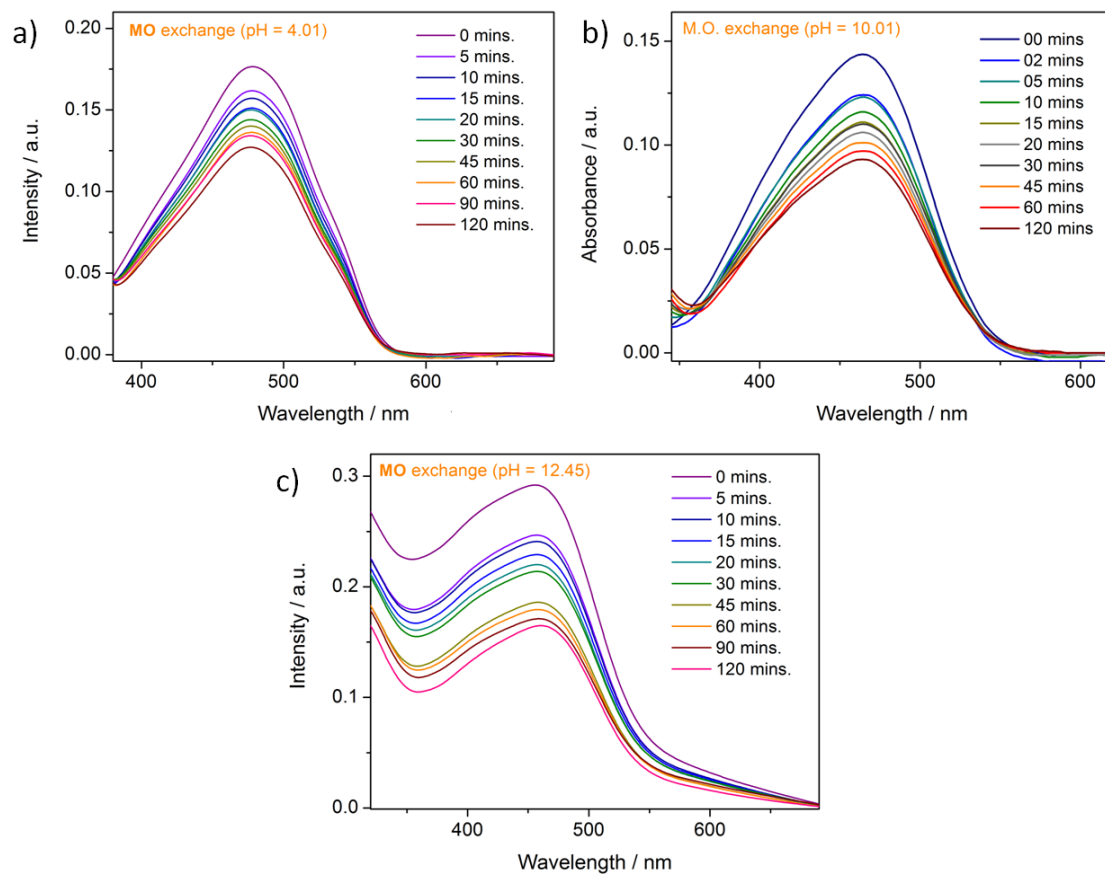
Figure S49: Dye capture studies by IPM-MOF-201, related to Figure 3.
Illustration showing capture of anionic dyes (IC & ARS) by compound **IPM-MOF-201**.

Figure S50: Dye capture studies by IPM-MOF-201, related to Figure 3.
Powder x-ray diffraction patterns of simulated (grey), as-synthesized (blue), and aqueous phase dye exchanged phases (MO - purple, IC - green, ARS - wine red).

Figure S51: Dye capture studies by IPM-MOF-201, related to Figure 3.
UV-Vis spectra of the supernatant aqueous solution of a) IC and b) ARS, after addition of compound **IPM-MOF-201** at different time intervals.

Figure S52: Dye capture studies by IPM-MOF-201, related to Figure 3.
UV-Vis spectra of blank aqueous dye solutions at different time intervals.

Figure S53: Dye capture studies by IPM-MOF-201, related to Figure 3.
UV-Vis spectra of the supernatant aqueous solution of bromothymol blue (BTB) at pH=7 after addition of compound **IPM-MOF-201** at different time intervals.
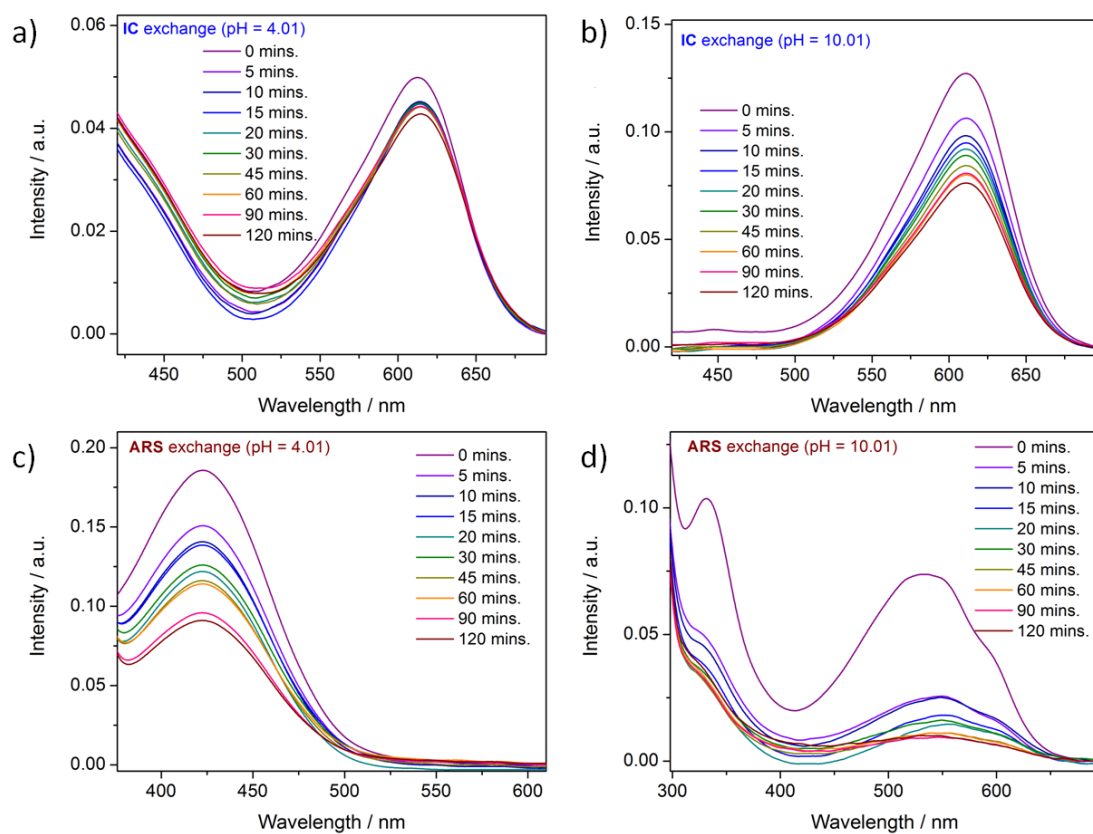
Figure S54: Dye capture studies by IPM-MOF-201, related to Figure 3.
UV-Vis spectra of the supernatant solution of a) IC (pH=4.01), b) IC (pH =10.01), c) ARS (pH=4.01) and d) ARS (pH=10.01), after addition of compound **IPM-MOF-201** to respective phases at different time intervals.
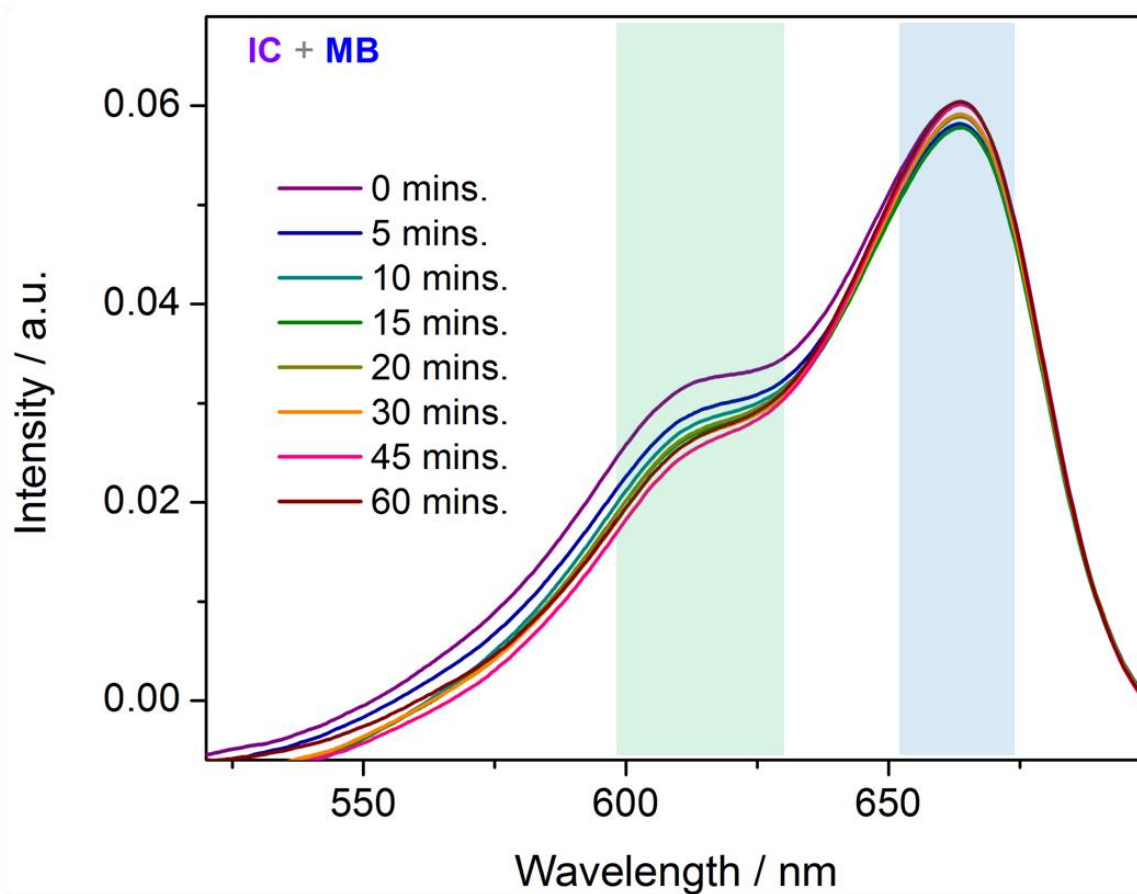
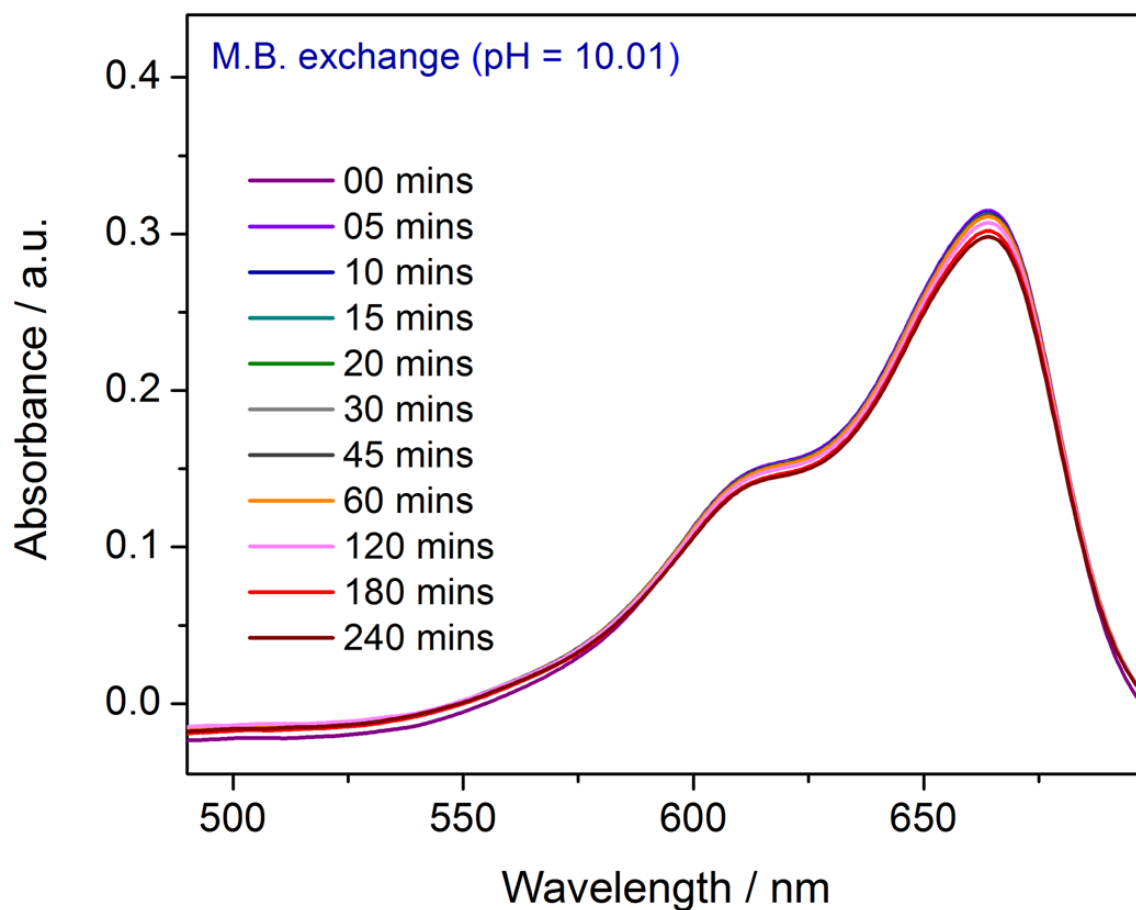**Figure S55: Dye capture studies by IPM-MOF-201, related to Figure 3.**
UV-Vis spectra of the supernatant solution of equimolar mixture of MB & IC after addition of compound **IPM-MOF-201** recorded at different time intervals.
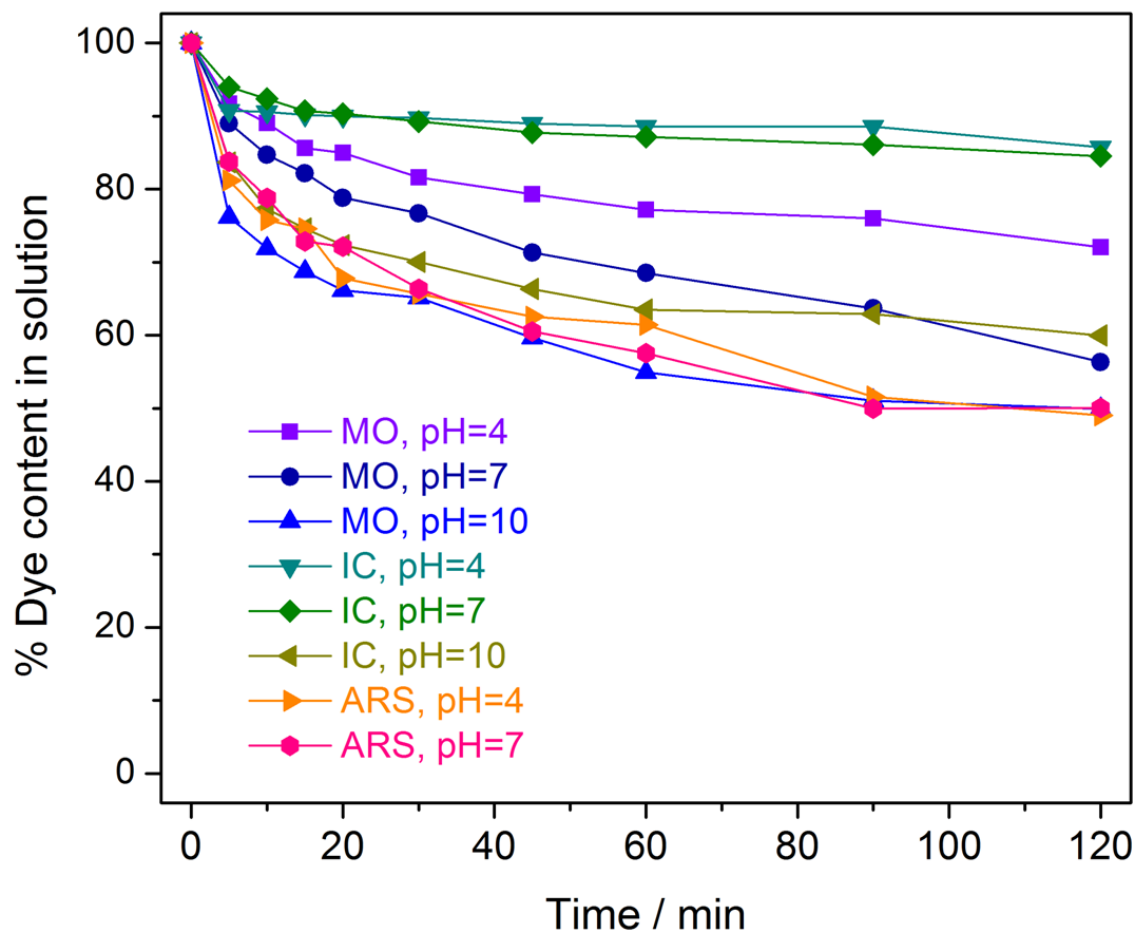
Figure S56: Dye capture studies by IPM-MOF-201, related to Figure 3.
Plot showing the rate of decrement in the concentration of the supernatant solution upon addition of compound **IPM-MOF-201**, recorded at different time intervals.
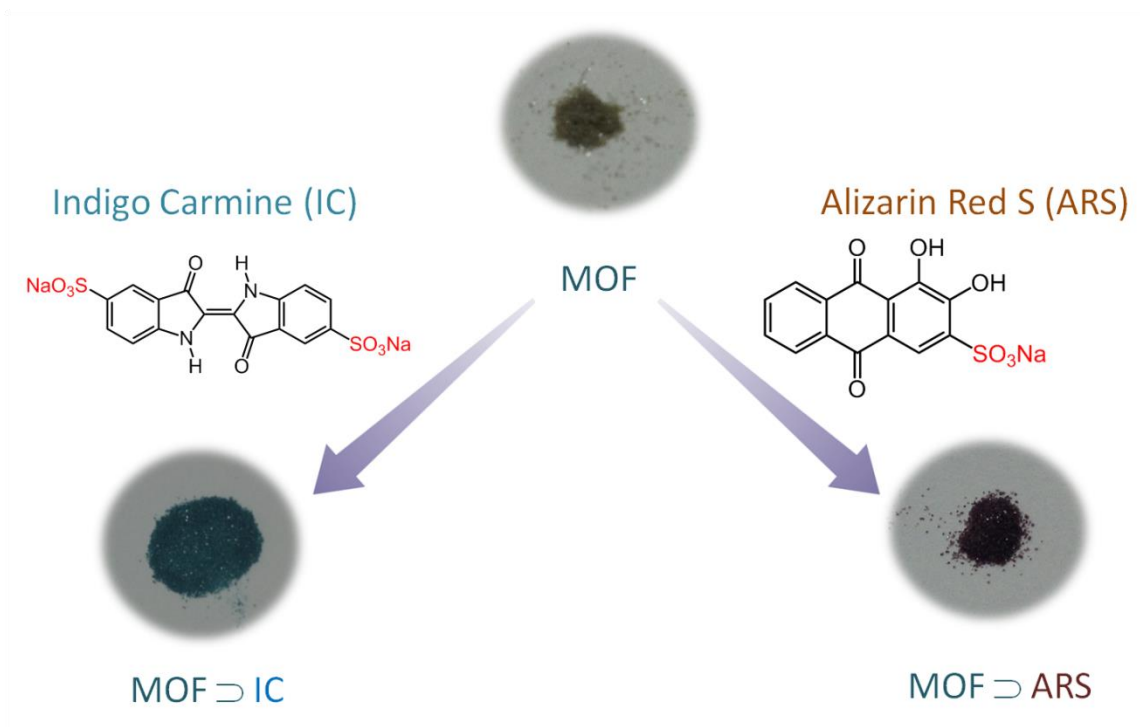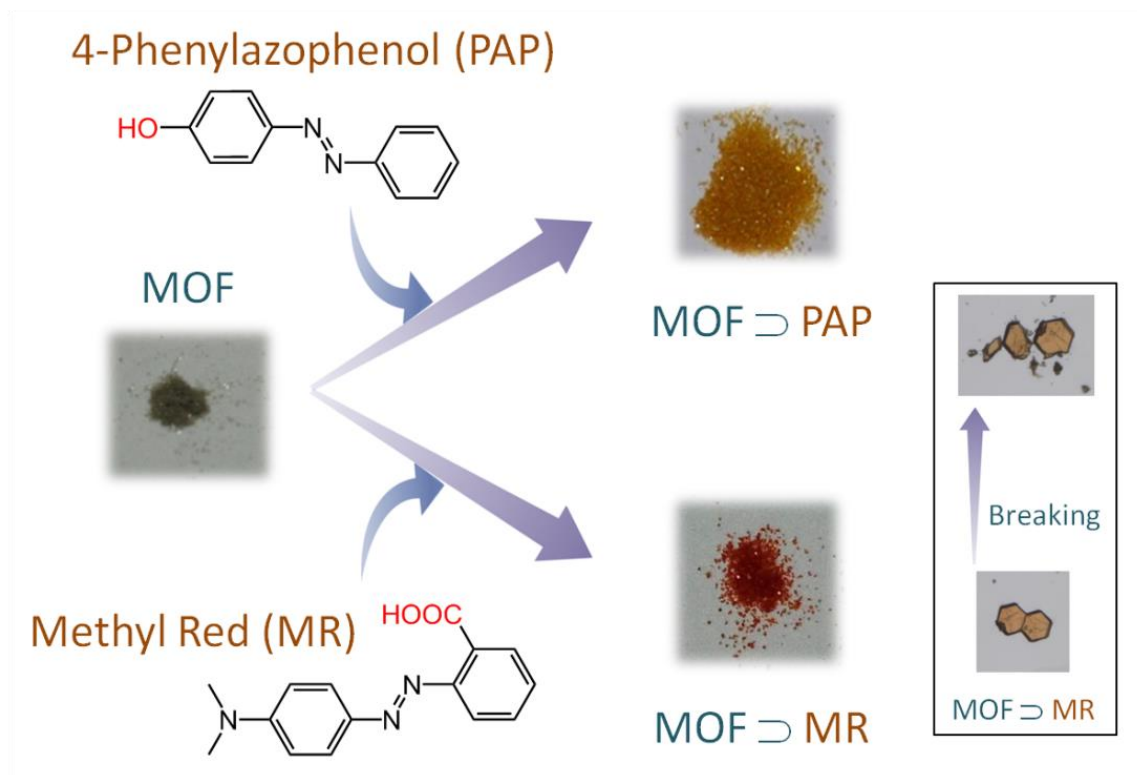
Figure S57: Dye capture studies by IPM-MOF-201, related to Figure 3.
Illustration showing capture of anionic dyes (PAP & MR) by compound **IPM-MOF-201**. (Inset): The photograph of MR-exchanged crystals and the fragments after breaking it randomly.
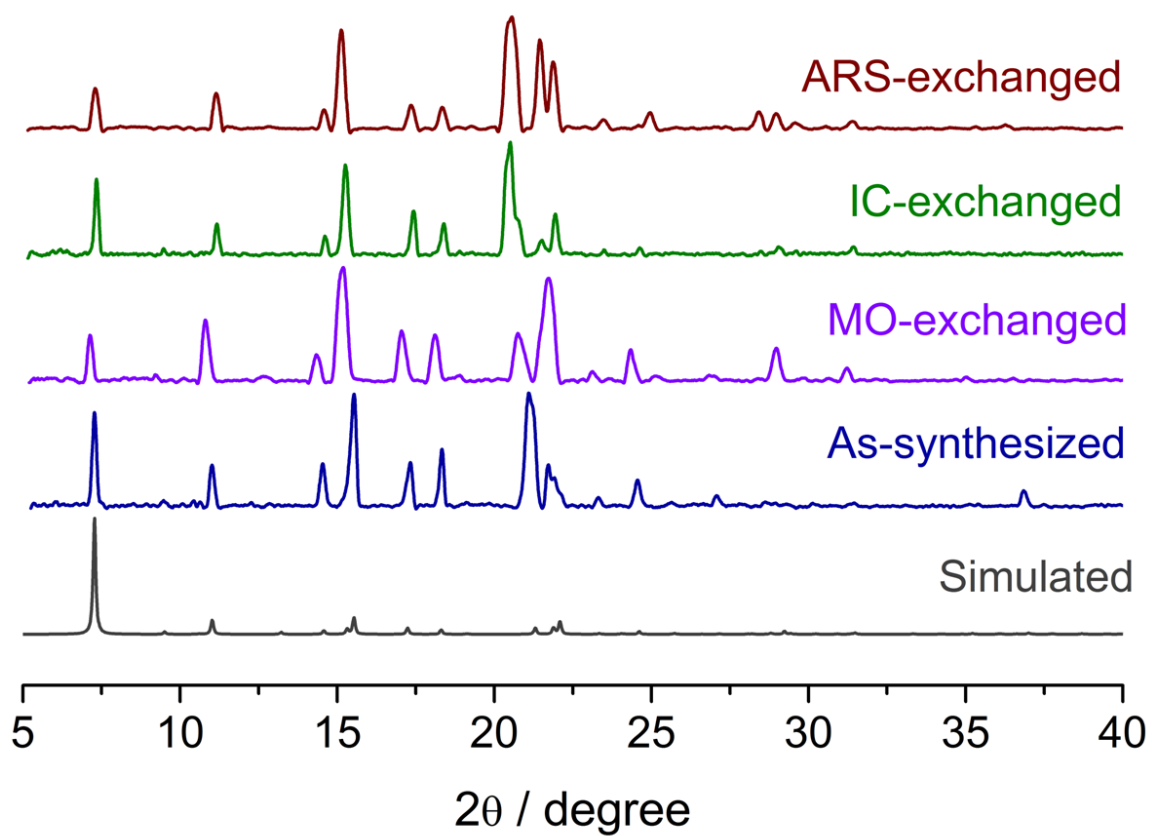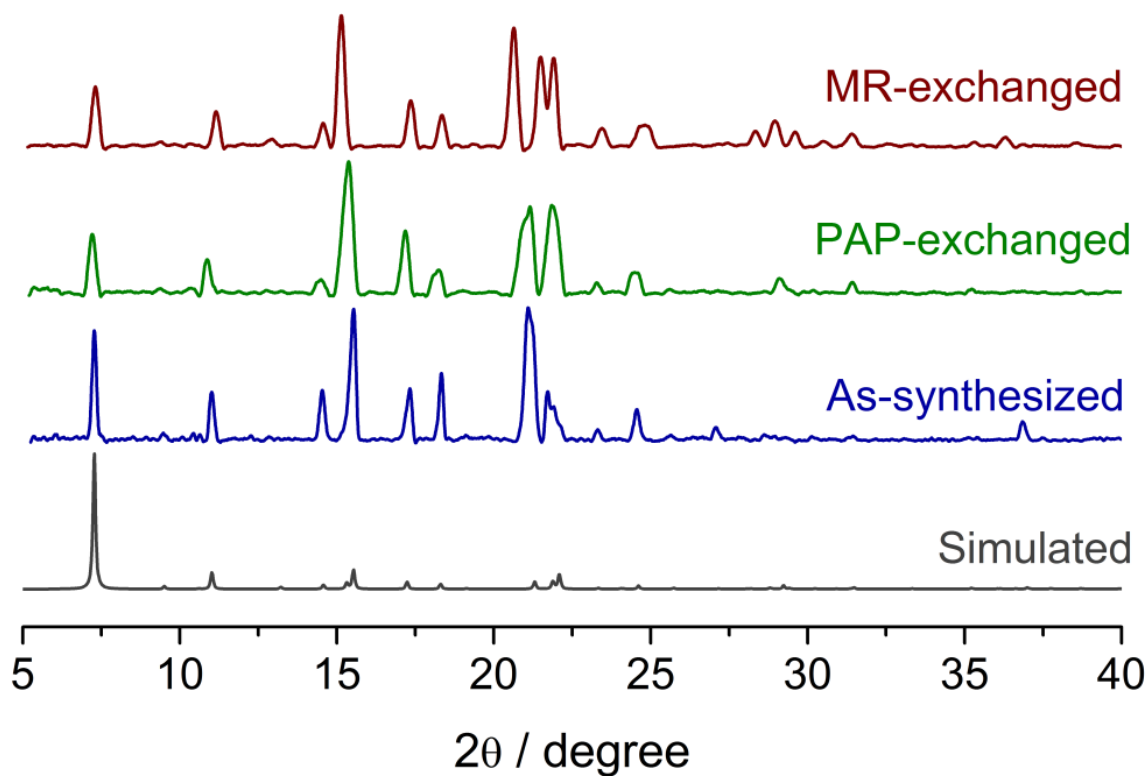
Figure S58: Dye capture studies by IPM-MOF-201, related to Figure 3.
Powder x-ray diffraction patterns of simulated (grey), as-synthesized (blue), and aqueous phase dye exchanged phases (PAP - green, MR - wine red).
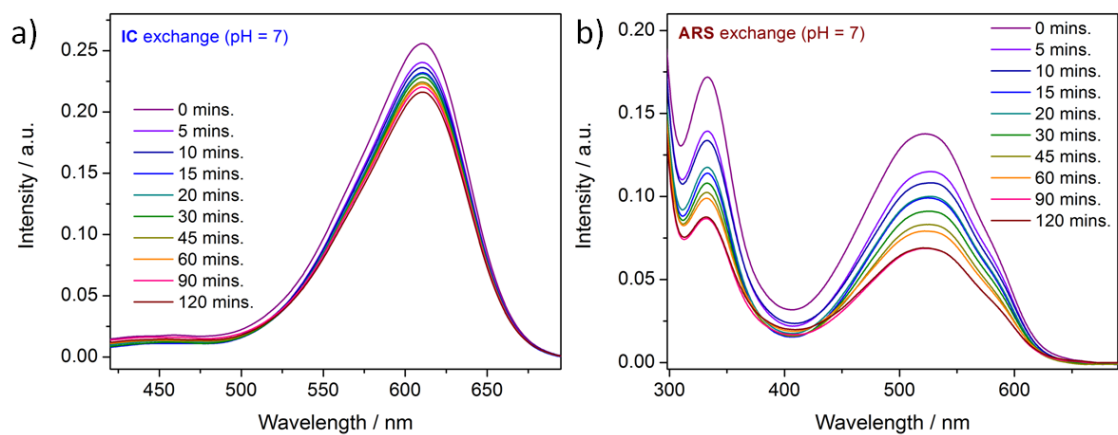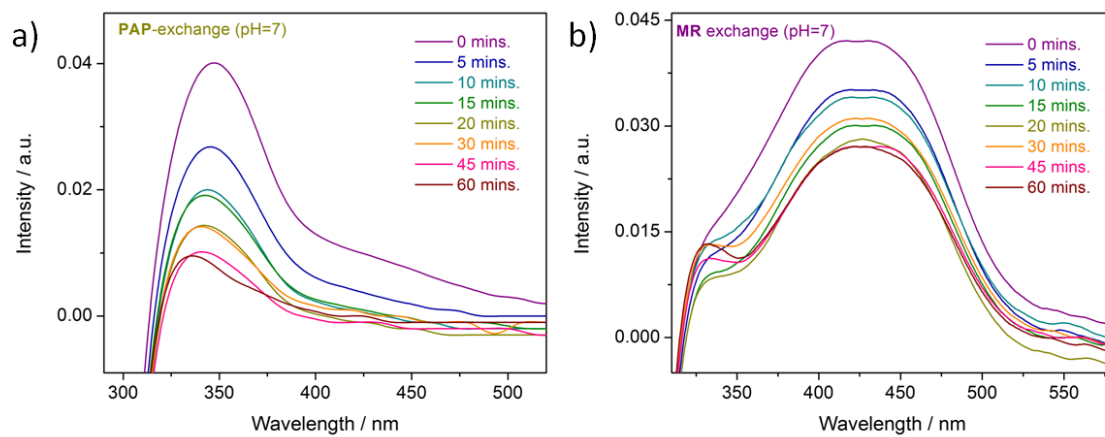
Figure S59: Dye capture studies by IPM-MOF-201, related to Figure 3.
UV-Vis spectra of the supernatant aqueous solution of a) PAP and b) MR, after addition of compound **IPM-MOF-201** at different time intervals.
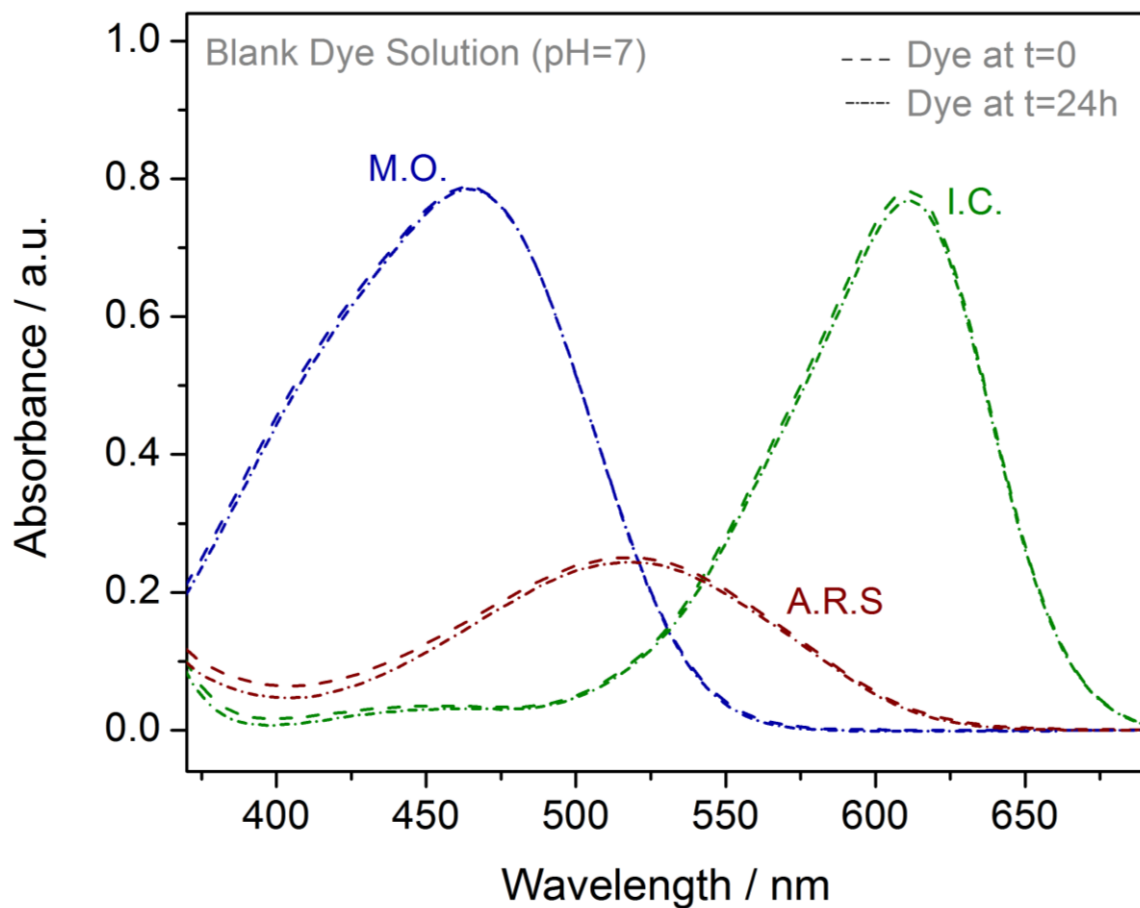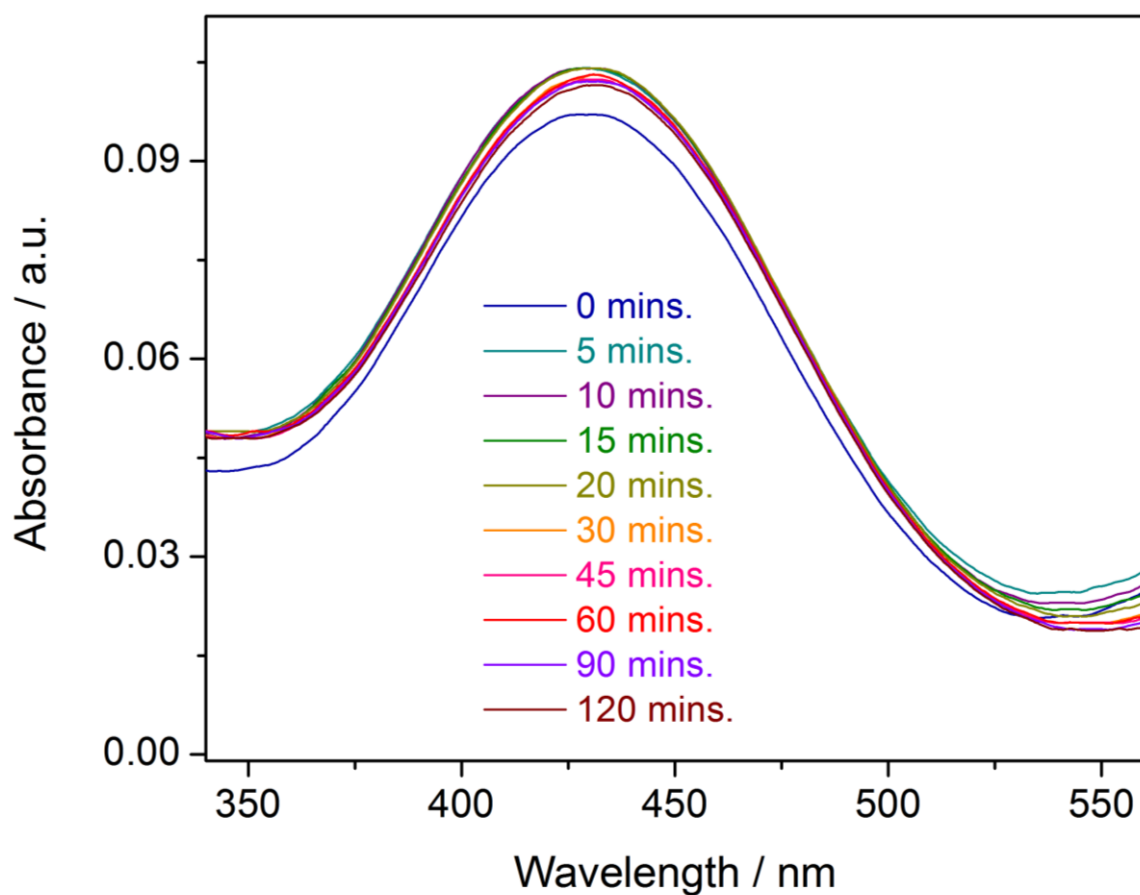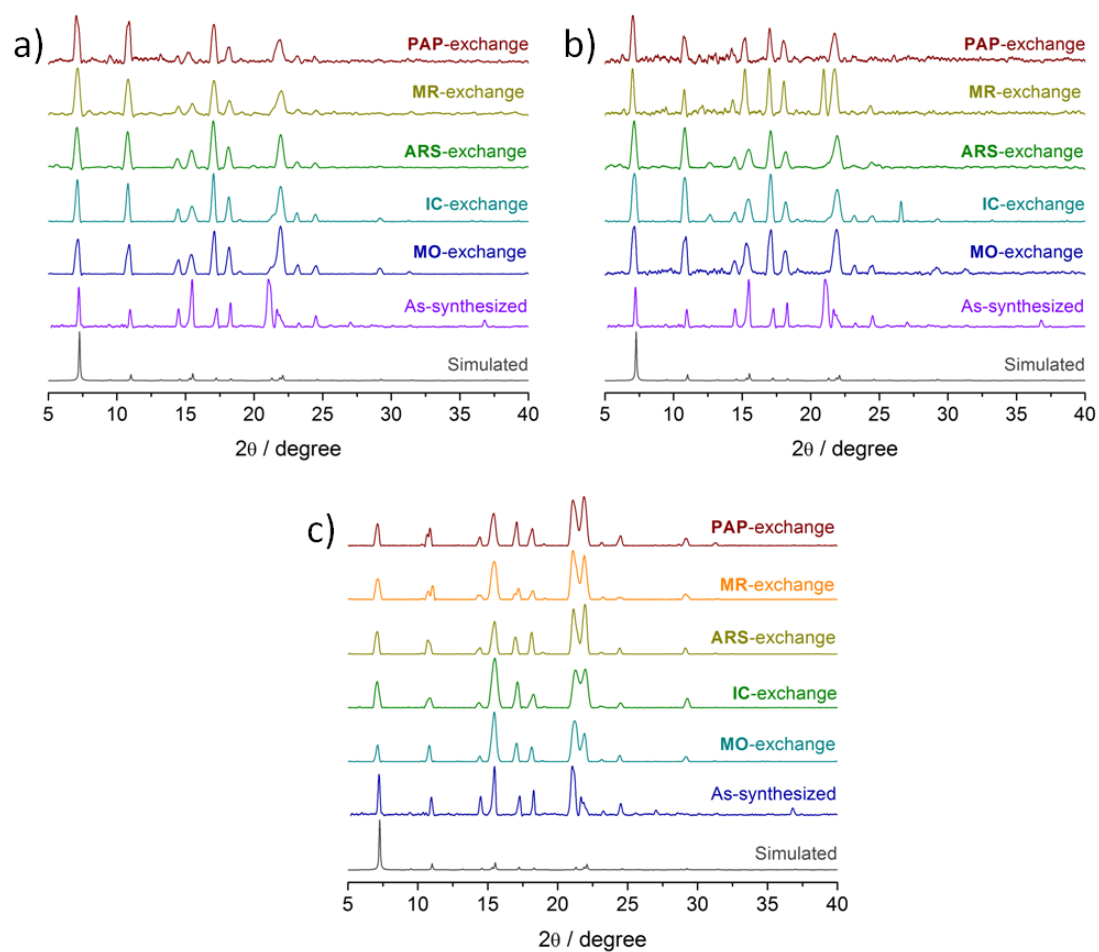
Figure S60: Dye capture studies by IPM-MOF-201, related to Figure 3.
Powder x-ray diffraction patterns of dye-exchanged phases at different pH, a) pH = 4.01, b)
pH = 10.01 and c) pH = 12.45.
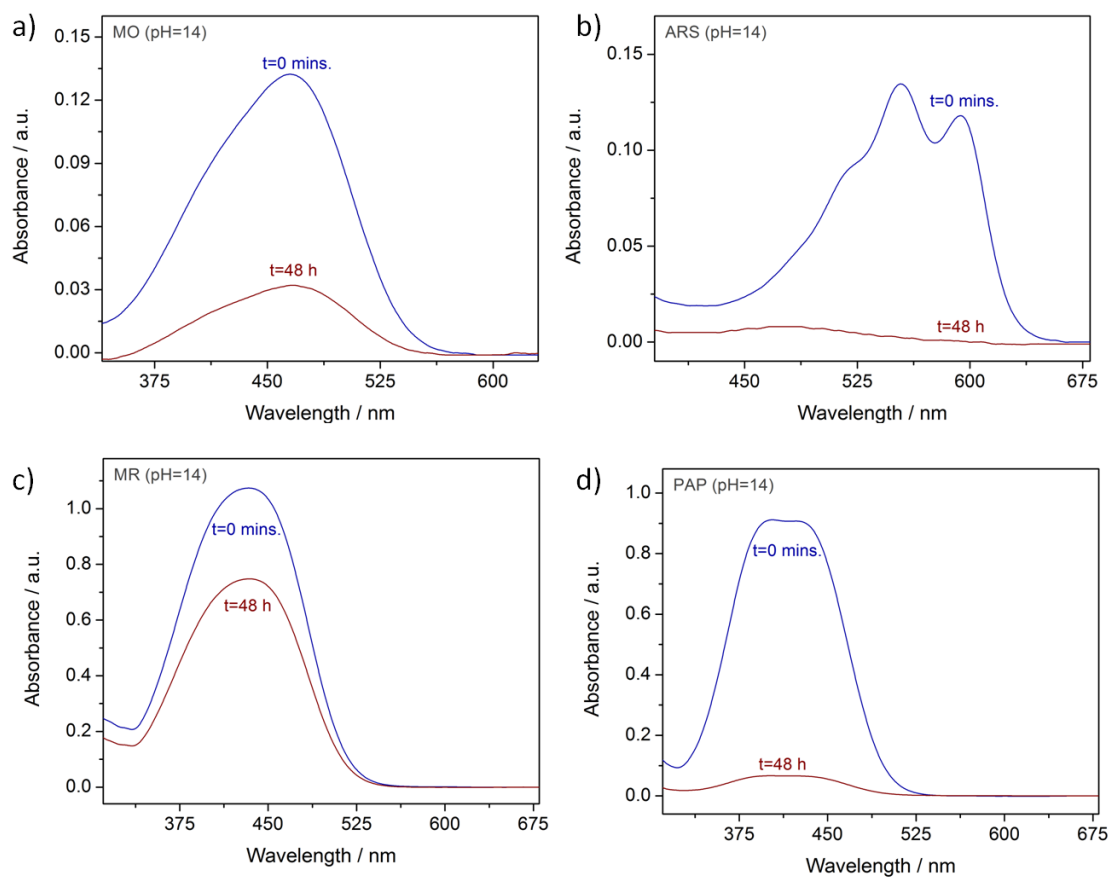
Figure S61: Dye capture studies by IPM-MOF-201, related to Figure 3.
UV-vis spectra of the supernatant at pH = 14, after addition of compound **IPM-MOF-201** at two time intervals.
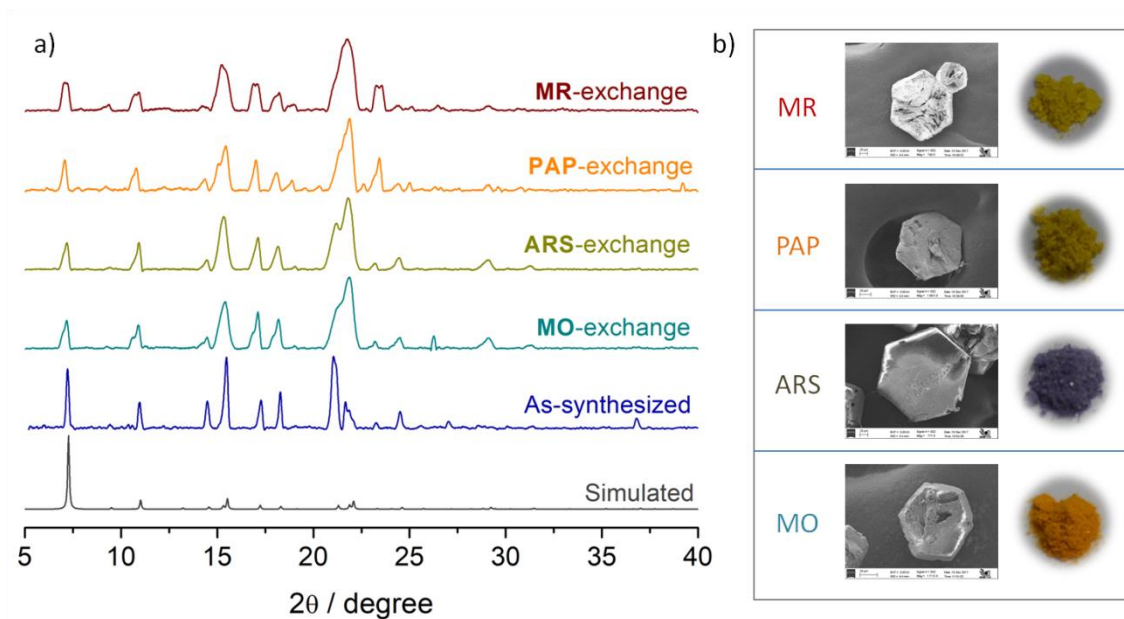
Figure S62: Dye capture studies by IPM-MOF-201, related to Figure 3.
a) Powder x-ray diffraction patterns of dye-exchanged phases at pH = 14, b) corresponding SEM images and naked-eye photographs.
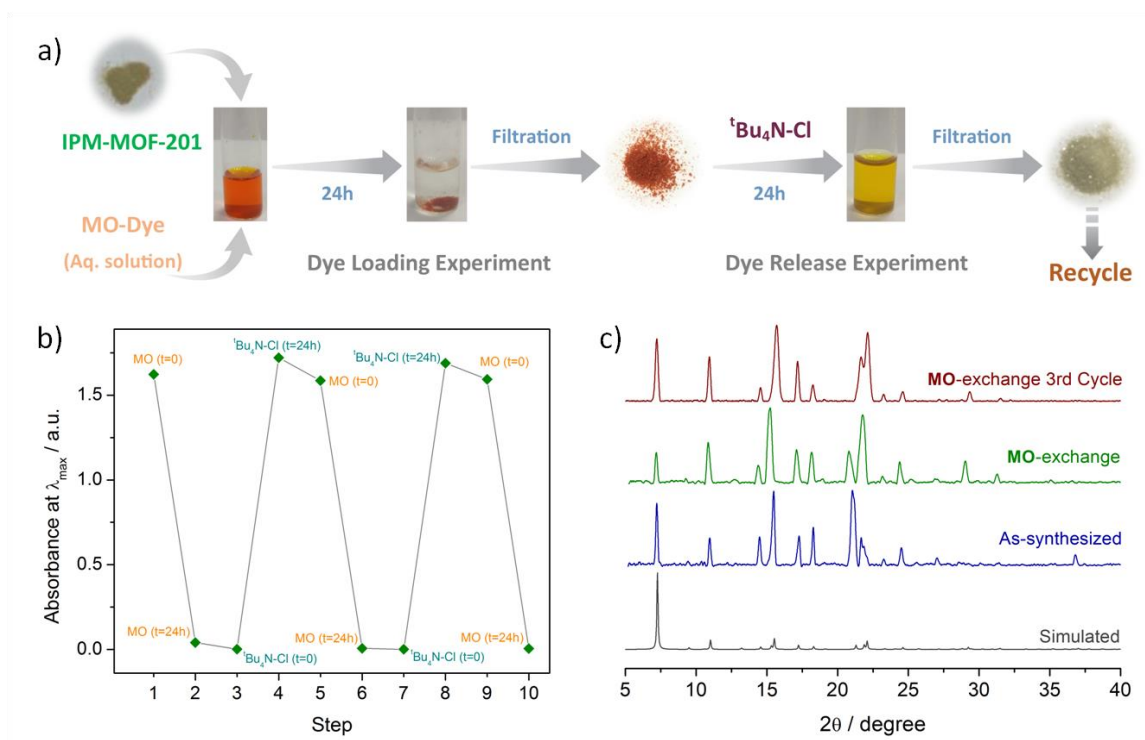
Figure S63: Dye capture studies by IPM-MOF-201, related to Figure 3.
a) Schematic depiction of the cyclic experiment for capture of MO-dye, b) absorbance of the supernatant during the adsorption-desorption cycles; c) PXRD patterns of the phase recovered after the 3rd adsorption cycle.

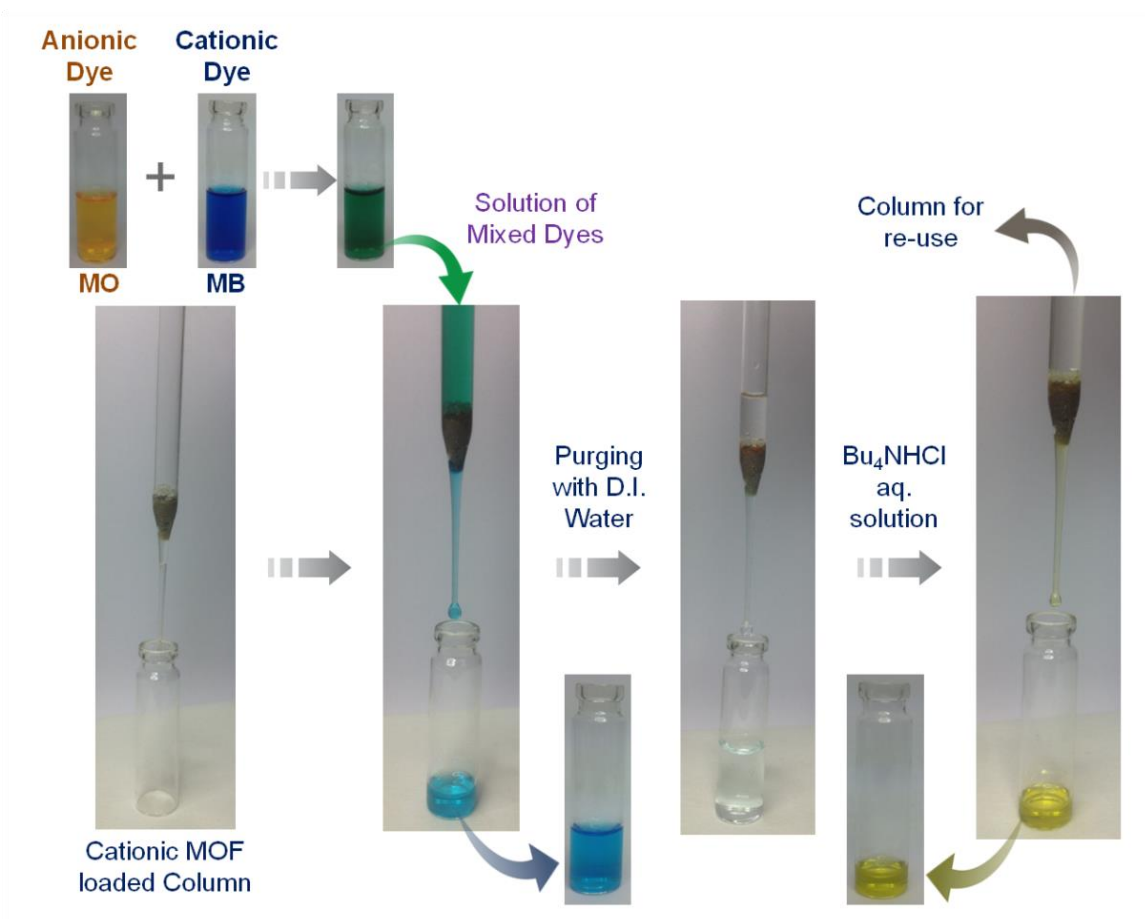
Figure S64: Dye capture studies by IPM-MOF-201, related to Figure 3.
Representation of the selective dye capture process by a MOF-loaded column.
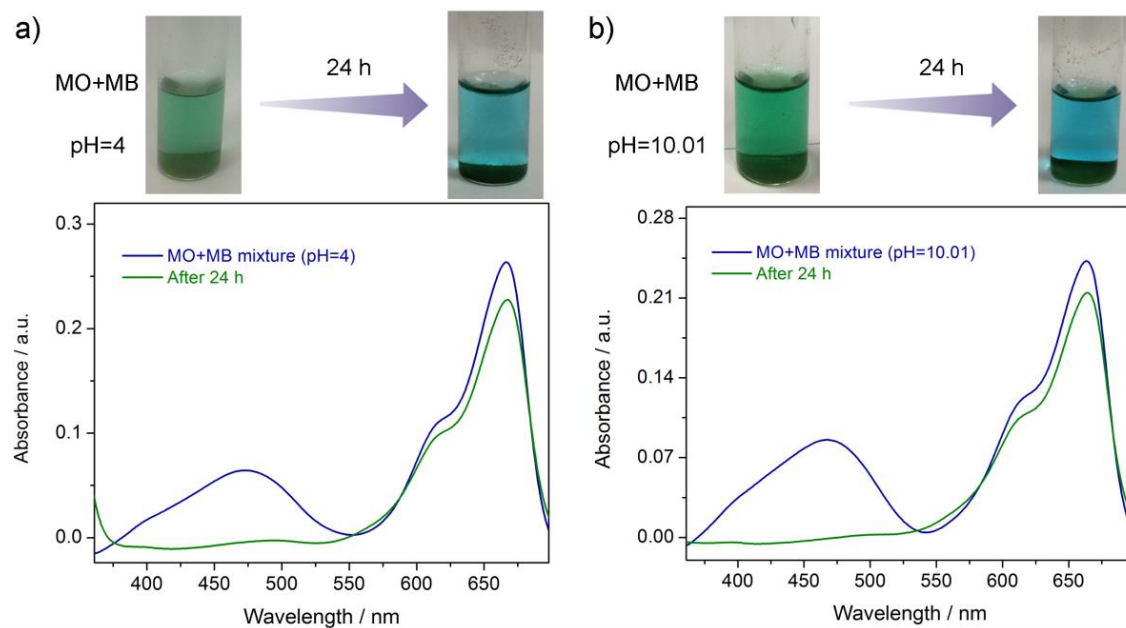
Figure S65: Dye capture studies by IPM-MOF-201, related to Figure 3.
Naked-eye changes and corresponding UV-Vis spectral profiles for mixtures of methyl orange (MO) [anionic] and methylene blue [cationic] at different time intervals for a) pH=4 and b) pH=10.01.

SCHEMES
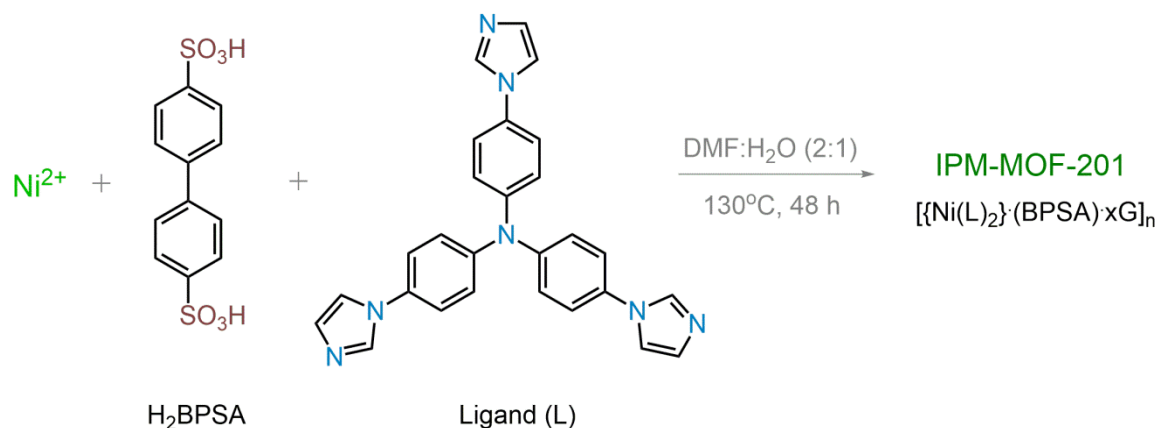
Scheme S1: Representation of the protocol employed for the synthesis of **IPM-MOF-201**, related to Figure 1.
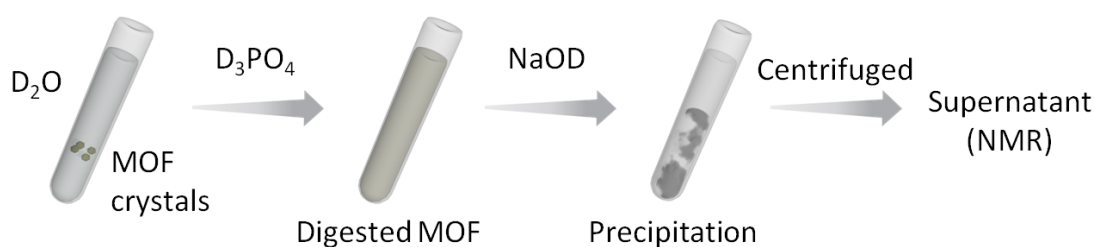
Scheme S2: Schematic illustration of the protocol employed for digesting **IPM-MOF-201**, related to Figure 1.
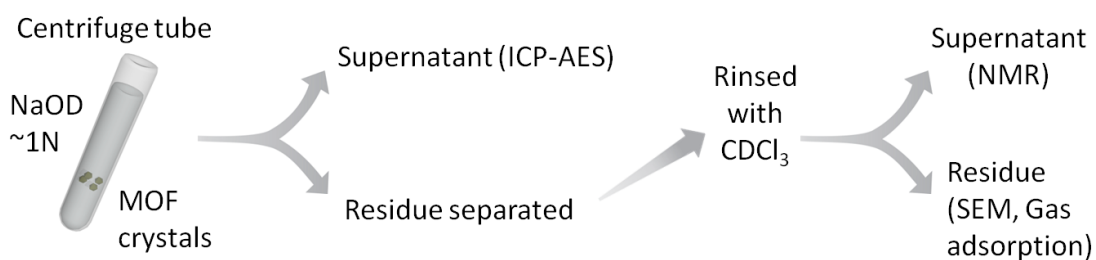
Scheme S3: Schematic illustration of the protocol employed for the ascertaining the base stability of **IPM-MOF-201**, related to Figure 2.

TABLES

Table S1: Stability studies of IPM-MOF-201, related to Figure 2.
Content of Ni (in ppm) in the supernatant solution recorded using ICP-AES.

Phase	Ni(ppm)
pH = 4 (2 days)	1.85
1N NaOH (1day)	0.485
NMR Supernatant (1 day)	0.033

Table S2. **Crystal data and structure refinement for IPM-MOF-201, related to Figure 1**.

Identification code	IPM-MOF-201
Empirical formula	C54 H42 N14 Ni
Formula weight	945.72
Temperature	100(2) K
Wavelength	0.71073 Å
Crystal system	Trigonal
Space group	R-3:H

Unit cell dimensions

$a = 16.0448\ (10)$ Å $\quad\quad \alpha = 90°$.
$b = 16.0448\ (10)$ Å $\quad\quad \beta = 90°$.
$c = 25.0057\ (18)$ Å $\quad\quad \gamma = 120°$.

Volume	5574.9 (8) Å^3
Z	3
Density (calculated)	0.845 Mg/m^3
Absorption coefficient	0.30 mm^{-1}
F(000)	1476
Crystal size	0.17 x 0.12 x 0.10 mm^3
Theta range for data collection	2.2 to 28.4°.
Index ranges	-19<=h<=21, -21<=k<=21, -33<=l<=33
Reflections collected	46123
Independent reflections	3119 [R(int) = 0.131]
Completeness to theta = 28.42°	0.999
Absorption correction	Semi-empirical from equivalents
Refinement method	Full-matrix least-squares on F^2
Data / restraints / parameters	3119 / 0 / 105
Goodness-of-fit on F^2	1.164
Final R indices [I>2sigma(I)]	R1 = 0.090, wR2 = 0.2959
R indices (all data)	R1 = 0.1542, wR2 = 0.334
Largest diff. peak and hole	0.43 and -0.37 e.Å^{-3}

Table S3: Stability studies of IPM-MOF-201, related to Figure 2.
Comparison of unit cell parameters of the compound treated under different conditions.

Cell Parameters	As-synthesized	Dipped in pH=4	Dipped in 1N NaOH
a	16.0448(10)	15.95±0.05	15.96±0.07
b	16.0448(10)	15.95±0.05	15.96±0.07
c	25.0057(18)	25.12±0.09	25.02±0.012
α=β	90	90	90
γ	120	120	120
Volume (Å^3)	5574.9(8)	5540±30	5520±50

TRANSPARENT METHODS

Materials: All solvents and reagents were commercially available and used without further purification. Standard pH buffers (pH = 4.01, 10.01, 12.45) were procured from Eutech Instruments. The other pH conditions were prepared using concentrated HCl and NaOH flakes.

Synthesis of Ligand {Tris(4-(1H-imidazol-1-yl)phenyl)amine}: The ligand was synthesized according to the reported protocol (Desai et al., 2016). The mixture of tris(4-bromophenyl)amine (500 mg, 1.04 mmol), imidazole (423 mg, 6.22 mmol), K_2CO_3 (573 mg, 4.15 mmol) and $CuSO_4$ (6.5 mg, 0.041 mmol) was kept for heating at 150^oC under inert atmosphere for 60 hours. Upon cooling to room temperature, CH_2Cl_2 (50 ml) was poured into the reaction mixture and washed several times with deionised water. The organic layer was evaporated under reduced pressure yield a pale coloured powder. The obtained ligand was recyrstallized from a mixture of $MeOH:CH_2Cl_2$ (1:1) in yield of 68%.

Synthesis of Compound IPM-MOF-201: A mixture of ligand (8.86 mg, 0.02 mmol), $NiSO_4 \cdot xH_2O$ (5.60 mg, 0.02 mmol), 4,4'-biphenyldisulfonic acid [H_2BPSA] (9.45 mg, 0.03 mmol), N,N-dimethylformamide (2 ml) and water (1 ml), was placed in a teflon capped pyrex tube, and heated at 130^oC for 48 hours followed by slow cooling to room temperature. The compound was filtered and washed with water and methanol several times. Pale green colour crystals of compound IPM-MOF-201 viz. [{Ni(L)$_2$}·(BPSA)·xG]$_n$ were isolated in ~40% yield. These crystals were dipped in MeOH solution for 2 days prior to heating it under vacuum at 75^oC to obtain the guest free phase. We were unable to locate the highly disordered guest solvent molecules and uncoordinated anion in the structure crystallographically. From the SQUEEZE function of PLATON the formula for the guest-free phase was estimated to be [{Ni(L)$_2$}·(BPSA)]$_n$. Anal. Calcd.: C/N, 4.04; N/S, 3.06; C/S, 12.35. Found: C/N, 3.98; N/S, 3.15; C/S, 12.57.

pH Stability Test: ~50 mg of the activated compound IPM-MOF-201 was dipped in 5 ml of separate pH solution (pH = 4, 10.01, 12.45, 14) and stirred at room temperature for 24 hours. The respective solutions were filtered off (the supernatant was collected and submitted for ICP-AES analyses) and the residue was washed with deionised water multiple times, followed by washing with methanol. All the phases were then degassed by heating under reduced pressure for further characterization. For gas adsorption studies, the compounds were pre-treated at 120^oC under vacuum before measurement.

To validate the base resistance of the compound, 20 mg of the activated phase of **IPM-MOF-201** was added to a solution of ~1N NaOD (0.5 ml, 40 wt%; Sigma Aldrich) in D_2O (4.5 ml; Sigma Aldrich) and kept at room temperature for 24 hours. This mixture was centrifuged and ICP-AES analysis was performed on the supernatant. The residue was then treated with $CDCl_3$ (3.0 ml; Sigma Aldrich) and the NMR spectra for this supernatant was also recorded. The residue obtained after the second step was used for further characterization (Scheme S3).

Dye Exchange Studies: ~10 mg of activated crystalline powder of IPM-MOF-201 was dipped in aqueous solution of methyl orange [MO] (1 mM, 2 ml) for 2 days at room temperature to yield the dye-encapsulated product. After anion exchange the compound was washed with deionised water and methanol several times to remove any dye adsorbed on the surface of the compound. The air-dried compounds were then used for further characterization. The same protocol was followed for other dyes viz. indigo carmine [IC], alizarin red S [ARS], methyl red [MR], 4-phenylazophenol [PAP]. Similarly, the dye exchange experiments were carried out at other pH conditions (pH = 4, 10.01, 12.45, 14). For

the UV-vis measurements, the standard deviation was calculated from five blank measurements of the dye solutions. The standard deviations for MO, IC, ARS, MR, PAP dyes were calculated to be 0.00589, 0.00728, 0.00187, 0.00083, 0.0013 respectively.

Synthesis of analogous Ni-MOFs: Metal salts of Ni^{2+} (NO_3^-, Cl^-, SiF_6^{2-}, Br^-, OTf^-; 0.02 mmol each) were added separately to the mixture of ligand (8.86 mg, 0.02 mmol), 4,4'-biphenyldisulfonic acid [BPSA] (9.45 mg, 0.03 mmol) in N,N'-dimethylformamide (DMF; 2 ml) and water (1 ml). The mixture was heated at 130°C for 48 hours in a Pyrex tube. Upon cooling the compounds were washed with water and methanol and dried in air for further characterization.

Characterization of the free anion: The presence of the free anion ($BPSA^{2-}$) was characterized by digesting the MOF. To minimize the content of the transition metal ion Ni(II) in the NMR sample, a 2-step protocol was employed for validating the presence of the free anion (Scheme S2). To 20 mg of the activated phase of **IPM-MOF-201** in 0.5 ml D_2O, 0.2 ml D_3PO_4 (85% in D_2O) was added. To this solution NaOD (40 wt%) was added dropwise till the pH became neutral. As the pH reached neutral heavy precipitation was observed. This was separated by centrifugation and the supernatant was used to record the ^{1}H-NMR spectrum.

Water Stability Test: 20 mg of activated compound **IPM-MOF-201** was dipped in 5 ml of deionised water and kept at room temperature for 7 days. Subsequently, the compound was filtered off and dried in air for further characterization. For FESEM images, the compound was kept in deionised water for 30 days.

Control Experiment: Compound **IPM-MOF-201(Co)** was synthesized following above protocol, replacing $NiSO_4 \cdot xH_2O$ with $CoSO_4 \cdot 7H_2O$ (5.62 mg, 0.02 mmol). The crystalline powder thus obtained was filtered off and washed with water and methanol. It was activated under reduced pressure at 75°C and used for further characterization. For checking the pH stability, 10 mg of the crystalline powder was dipped in pH=12.45 buffer and pH=14 solution for 24 hours at room temperature. Subsequently it was washed with deionised water and acetonitrile, and dried in air for further characterization. The Co-MOF & Cd-MOF used for comparison were synthesized according to reported protocols (Yao et al., 2011; Liu et al., 2014).

Dye Content Calculation: The dye content in the solution was calculated using a reported protocol (Song et al., 2015). Time dependent UV-vis absorbance of the supernatant were recorded. The absorbance maxima corresponding to each dye in different pH was chosen to compute the dye content using the formula:

$D = (A_t/A_o) \times 100\%$

where D is the dye content in the corresponding pH solution, A_o characteristic absorbance of the solution before addition of the MOF, A_t is the absorbance of the solution at different time intervals.

Blank Dye Solution Experiment: The UV-vis spectra of blank aqueous dye solutions [~0.05mM] (without addition of MOF) was recorded at two time intervals (t=0 and t=24h) to validate the ion-exchange experiments in the presence of MOF.

Recycling Experiment: To an aqueous solution of MO (0.09 mM) ~10 mg of the activated phase of IPM-MOF-201 was added. After keeping it for 24 hours, the supernatant was collected and its UV-vis spectrum was recorded. The filtrate was air-dried and added to an aqueous solution of tetrabutylammonium chloride (50wt%, 2 ml). The supernatant was

collected after 24 hours and its UV-vis spectrum was monitored. The filtrate was air-dried and this cycle was repeated further.

MOF-loaded Column Experiment: A glass tube with narrow opening was used for this experiment which was plugged by thick cotton at the bottom. ~20 mg of the activated phase of IPM-MOF-201 was filled followed by addition of a uniform layer of white sand. This set-up was rinsed with deionised water 2-3 times before further use. A mixture of MO and MB (0.05 mM, 5 ml each) in deionised water was added to this column. The eluted MB solution was collected and then deionised water was purged until no further dye eluted out. Following this tetrabutyl ammonium chloride aqueous solution (50wt%) was passed to elute the trapped MO dye. This was passed until no further MO dye passed out.

Physical Measurements: Powder X-ray diffraction patterns were recorded on Bruker D8 Advanced X-Ray diffractometer using Cu Kα radiation (λ= 1.5406 Å) in 5° to 40° 2θ range with a scan speed of 1.2^{o}min^{-1}. The IR Spectra were acquired by using NICOLET 6700 FT-IR spectrophotometer using KBr pellet in 400-4000 cm^{-1} range. UV spectra were recorded on Shimadzu UV 2600 Spectrophotometer having stirring attachment. The SEM images & EDX data were obtained using FEI Quanta 3D dual beam ESEM. Thermogravimetric analysis profiles were recorded on Perkin-Elmer STA6000, TGA analyser under N_2 atmosphere with heating rate of 10°C/min. Gas adsorption measurements were performed using BelSorp-Max instrument (Bel Japan). Solvent adsorption measurements were performed on Bel-Aqua instrument (Bel Japan). Prior to adsorption measurements, the activated samples were heated at 130°C under vacuum for 6 hours using BelPrepvacII. ^{1}H & ^{13}C NMR spectra were recorded on a JEOL 400 MHz or Bruker 400 MHz spectrometer.

X-ray Structural Studies: Single-crystal X-ray data of compound IPM-MOF-201 was collected at 100 K on a Bruker D8 Venture Duo X-ray diffractometer equipped with Microfocus X-ray source (operated at 50W; 50kV/1mA), graded multilayer optics for monochromatic Mo Kα radiation (λ = 0.71073Å) focused X-ray beam and Photon 100 CMOS chip based detector system. Crystal was mounted on nylon CryoLoops (Hampton Research) with Paraton-N (Hampton Research). The data integration and reduction were processed with SAINT (*SAINT Plus*, 2004) software. A multi-scan absorption correction was applied to the collected reflections (Krause et al., 2015). The structure was solved by the direct method using SHELXTL (Sheldrick, 2008) and was refined on F^2 by full-matrix least-squares technique using the SHELXL-2014/7 (Sheldrick, 2015) program package within the WINGX(Farrugia, 2009) programme. All non-hydrogen atoms were refined anisotropically. All hydrogen atoms were located in successive difference Fourier maps and they were treated as riding atoms using SHELXL default parameters. The structures were examined using the *Adsym* subroutine of PLATON to assure that no additional symmetry could be applied to the models. High disorder was observed for the guest solvent molecules and the anion (BPSA). The SQUEEZE option (Spek, 2015) was used to eliminate the contribution of disordered guest molecules and anion. The number of the anions required to maintain the electrical neutrality was estimated and the molecular formula was calculated accordingly.

SUPPLEMENTAL REFERENCES

SAINT Plus, (2004). version 7.03; Bruker AXS Inc.: Madison, WI.

Krause, L., Herbst-Irmer, R., Sheldrick, G. M., and Stalke, D. (2015). Comparison of silver and molybdenum microfocus X-ray sources for single-crystal structure determination. J. Appl. Cryst. *48*, 3-10.

Sheldrick, G. M. (2008). A short history of *SHELX*. Acta. Cryst. *A64*, 112-122.

Sheldrick, G. M. (2015). Crystal structure refinement with *SHELXL*. Acta. Cryst. *C71*, 3-8.

Farrugia, L.(2009). *WinGX*, version 1.80.05; University of Glasgow: Glasgow, Scotland.

Spek, A. L. (2015). *PLATON* SQUEEZE: a tool for the calculation of the disordered solvent contribution to the calculated structure factors. Acta. Cryst. *C71*, 9-18.